2015

Dosimetric applications of hybrid pixel detectors

Stuart George
University of Wollongong, spg085@uowmail.edu.au

University of Wollongong 

DOSIMETRIC APPLICATIONS OF HYBRID PIXEL DETECTORS

A Dissertation Submitted in Fulfilment of
the Requirements for the Award of the Degree of

Doctor of Philosophy

from

UNIVERSITY OF WOLLONGONG

by

Stuart P. George
MPhys

School of Physics
Faculty of Engineering and Information Sciences

2015

CERTIFICATION

I, Stuart P. George, declare that this thesis, submitted in fulfilment of the requirements for the award of Doctor of Philosophy, in the School of Physics, Faculty of Engineering and Information Sciences, University of Wollongong, is wholly my own work unless otherwise referenced or acknowledged. The document has not been submitted for qualifications at any other academic institution.

(Signature Required)

Stuart P. George
13 October 2015

Dedicated to

my wonderful wife Elyse.

Table of Contents

List of Tables

List of Figures

Acknowledgements

I would like to acknowledge and thank the following people.

Of course my wife Elyse comes first, for her constant support and love.

My supervisors Prof. Anatoly Rozenfeld at UoW and Dr. Marco Silari at CERN, for equal measures of guidance, wisdom and tolerance. Dr. Fabrizio Murtas and Dr. Alessandro Curioni at CERN for your help and suggestions. Everyone else in DGS-RP-SP section at CERN for your ideas, humour and sharp wit. All of the ARDENT ESR's – for the fine company, excellent science, and tasty beer. It has been a pleasure and privilege to know you all over the last 3 years.

The Medipix guru's Dr. Erik Frojdh, Dr. John Idarraga and Dr. Jerome Alozy – this thesis probably would never have been written without your help and guidance. Everyone at UoW, UH and NASA SRAG, especially Dr. Susanna Guatelli, Dr. Dean Cutajar, Prof. Larry Pinsky and Dr. Nick Stoffle.

My family and friends, who have kept me happy over these last years and writing over the last few months.

And of course all those, who reading this, feel that they should be thanked too.

S.P.G, Wollongong, 20th of September, 2015

This research project has been supported by the Marie Curie Initial Training Network Fellowship of the European Community's Seventh Framework Programme under Grant Agreement PITN-GA-4 2011-289198-ARDENT.

Radiation, unlike smoking, drinking, and overeating, gives no pleasure, so the possible victims object. - Issac Asimov

Dosimetric Applications of Hybrid Pixel Detectors

Stuart P. George

A Thesis for Doctor of Philosophy in Physics

School of Physics
University of Wollongong

ABSTRACT

This thesis discusses the application of the Timepix hybrid pixel detector to mixed field characterisation and dosimetry.

A brief history of silicon detectors and the physics of radiation detection in semiconductors is presented, and the Timepix ASIC is introduced. A guide is given to the setup, characterisation and the energy calibration of a Timepix detector (a Timepix attached to a silicon sensor).

The analysis of tracks left in the Timepix detector to produce characteristics of the impinging particle such as track polar angles and equivalent dose deposited is described. Applications of these methods are demonstrated at the CERF facility at CERN and on the International Space Station.

A novel energy independent fast neutron dosimeter based on a multilayer polyethylene converter placed on a Timepix detector is developed using Geant4 Monte Carlo simulations. A version of this converter is 3D printed and characterised using neutrons at the NTOF time of flight facility at CERN. A key capability of this detector is the potential ability to subtract gamma ray and charged particle background.

A new detector, the GEMPix is presented. This detector is based on a triple gas electron multiplier coupled to a quad Timepix ASIC for readout. The detector is operated as a highly compact ($10\,\mathrm{cm}^3$) time projection chamber. Characterisation measurements of this detector with photons, alpha particles and relativistic protons are described. The use of this detector as a microdosimeter is briefly discussed.

KEYWORDS: Pixel detectors, Timepix, mixed field characterisation, space dosimetry, neutron dosimetry, gas electron multipliers (GEM), time projection chambers (TPC), microdosimetry.

Contributions

Publications and Publications Submitted

- S. P. George, C. Severino et al, *Measurement of an accelerator based mixed field with a Timepix detector. JINST* **10** (2015), P03005, `http://dx.doi.org/10.1088/1748-0221/10/03/P03005`.

- S. P. George, F. Murtas et al, *Particle tracking with a Timepix based triple GEM detector. JINST* **10** (2015), P11003, `http://dx.doi.org/10.1088/1748-0221/10/11/P11003`

- I have two publications in preparation based on the contents of chapters 4 and 5 which will be submitted in the coming months.

Presentations and Seminars

- IEEE NSS-MIC 2015, San Diego, USA, November 2015, *"Particle Tracking with a Timepix Based Triple GEM Detector"*,

- (Poster, second author) IEEE NSS-MIC 2015, San Diego, USA, *"Patient-specific treatment plan verification in Hadrontherapy: GEANT4 simulation of a GEM detector as beam monitor"*

- Invited Seminar, University of Wollongong, Australia, June 2015, *"Particle Tracking and Neutron Dosimetry with Timepix and Gempix"*

- MPGD Industry Matching Event, CERN, March 2015, *"Neutron Beam Monitoring with Hybrid Pixel Detectors"*

- MMND 2014, Port Douglas, Australia, October 2014, *"Mapping the Asymmetry in the SAA Fluxes Using the Medipix Particle- by-Particle Directional Information"*

- NTOF Collaboration Meeting, CERN, October 2014 *"Using Timepix for Neutron Measurements at NTOF"*

- WORMISS 2014, Krakow, Poland, September 2014, *"Mapping the Asymmetry in the SAA Fluxes Using the Medipix Particle- by-Particle Directional Information"*

- Invited Seminar (Rare Event Detection group), Livermore National Lab, USA, August 2014, *"Using Timepix based gas detectors to monitor clinical hadron therapy beams at single particle, 55μm resolution."*

- IEEE NSS-MIC 2013, Seoul, Korea, October 2013, *"Mixed Field Data Analysis with Timepix at the CERF Facility"*

- Medipix Collaboration Meetings:

  - CERN March 2015 *"High Resolution Particle Tracking with Gas Based Timepix Detectors"*
  - CERN, November 2014 *"Latest Results from Timepix on the ISS"*
  - Diamond Light Source, UK, May 2014 *"Clinical Hadron Therapy Beam Monitoring with GEMPix"*
  - CERN, February 2014 *"The GEMPix, a Timepix Based Gas Detector"*
  - CERN, February 2013 *"The ARDENT Project - ESR4"*

Other Publications (unrelated to thesis)

- D. Pope, D. Cutajar, S. P. George, S. Guatelli, J. Bucci, E. Enari, S. Miller, S. Rainer, A. B. Rosenfeld, *"The Investigation of Prostatic Calcifications using μPIXE Analysis and their Dosimetric Effect in Low Dose Rate Brachytherapy Treatments using Geant4"*, Phys. Med. Biol. 60 (2015) 4335-4353.

- S. P. George, C. Bentham, X. Zeng, G. Ungar and GA Gehring, *"Monte Carlo study of the ordering in a strongly frustrated liquid crystal"*, Submitted to Phys. Rev. E.

Chapter 1

Introduction

Humans are increasingly exposed to mixed radiation fields. These fields contain a wide range of particle types and energies. The importance of these radiation fields is that they are different in character, and consequentially different in biological effect to those normally found on the surface of the earth. Clearly it is important to develop new detector technologies together with novel analytical approaches to characterise and understand these fields. This thesis seeks to explore how hybrid pixel detectors such as the Timepix detector can contribute to our knowledge of mixed radiation fields through using them in real world applications such as astronaut dosimetry on the International Space Station and assessment of mixed fields around particle accelerators. This thesis also explores how hybrid pixel detectors can be used in novel detector technologies such as an energy independent fast neutron dosimeter and a pixellated gaseous detector with applications in microdosimetry.

1.1 What is Radiation and Why Does it Matter?

Ionising radiation consists of any particle with an energy above about 10 eV. Common examples are energetic photons (gamma rays and or x-rays), electrons (beta particles), protons, helium nuclei (alpha particles), neutrons and muons [3]. Ionising radiation is toxic because of its ability to liberate electrons from their atoms (to ionise) along its path through matter. These electrons in turn can directly damage cellular structures or more often create oxygen radicals that create chains of damage around them. The most well known and well understood effects of radiation are cell death and DNA damage. Large scale cell death is a feature of high radiation doses ($\approx \mathrm{J\,kg^{-1}}$), causing

burns, tissue damage and if widespread, death. As many cancers are less effective at recovering from the damage caused by radiation than normal tissue, precisely delivered high doses of radiation form the basis for cancer radiotherapy [4]. DNA damage from low doses of radiation is more insidious, sometimes causing cellular mutations which go on to cause cancers later in life [5]. The effects from high dose damage are referred to as deterministic, as they tend to be similar in all individuals, while low dose effects are stochastic - only some people will get cancer from the same dose of radiation due to the random nature of the damage and mutation process. Less well understood are other effects from long term radiation exposure to long lived tissue such as the central nervous system [6], cardiovascular system [7] and the eye [8, 9].

1.2 Who Gets Exposed to Radiation?

Everyone is exposed to some level of ionizing radiation. The real questions are how do we measure radiation dose and how harmful is this dose?

In general everybody gets exposed to radiation at a rate of about 2 mSv/year - 10 mSv/year depending mainly on location. The natural component of this exposure is mostly radon gas, gamma rays from natural radioactive materials and cosmic ray muons [10]. The most significant man made component in the general population is medical irradiations, the dose rate from which varies widely between individuals.

The basic unit of radiation dose is the Gray (Gy). $1\,\mathrm{Gy} = 1\,\mathrm{J\,kg^{-1}}$ of energy deposited by ionising radiation. Different types of radiation are more or less biologically damaging depending on how they deposit energy on a microscopic length scale and the organs they deposit energy in. Therefore radiation dose is normally expressed as a weighted quantity, the sievert (Sv). Table 1.1 shows radiation exposures for the natural background as well as a selection of medical procedures, occupationally exposed workers and exceptional cases.

The LD50 of whole body irradiation (i.e. the point at which 50% of people will die from a single irradiation) is around 4 Sv, or around 7 Sv with medical intervention [14]. Not directly comparable, but still illustrative are the typical (tumour) treatment doses for radiotherapy, which are in the 10 - 150 Gy region depending on the cancer being treated, and the number of fractions in which the dose is delivered [4].

The main stochastic risk from radiation is cancer. The whole body cancer risk

	Source of Exposure	Dose/dose rate
Background	Cosmic Rays	0.4 mSv/year
Radiation	Terrestrial Gamma	0.5 mSv/year
	Radon	1.2 mSv/year
	Total	2.4 mSv/year
Medical	Average per person (first world)	1.2 mSv/year
Procedures	Dental x-ray	0.016 mSv
	Chest CT	10 mSv
	Mammography	0.5 mSv
Occupational	Nuclear Fuel Cycle (inc. mining)	1.8 mSv/year
Exposures	Aircrew	3 mSv/year
	Medical Workers	0.3 mSv/year
	Maximum dose CERN LS1 [11]	3.3 mSv/year
	Average dose CERN LS1 [11]	0.8 mSv/year
	Recommended occupational limit from ICRP 103 [5].	20 mSv/year
Exceptional	Max. dose for Chernobyl worker	$\approx$ 1 Sv
Exposures	Average dose for Chernobyl worker	0.1 Sv
	1 year mission on ISS [12]	0.1 Sv - 0.19 Sv
	Mars Mission [13]	0.5 Sv - 1.5 Sv

Table 1.1: Example radiation exposures, doses are average unless otherwise noted. CERN LS1 refers to the first long shutdown for the CERN LHC. Unless otherwise noted all numbers are from [10].

Exposed Population	Men	Women
Whole Life (0-85) (Sv^{-1})	15.8%	18.6%
Adult Life (18-65) (Sv^{-1})	11%	12.4%

Table 1.2: Estimated risk of developing cancer per sievert for different populations (age and sex) from a single radiation exposure. Data taken from ICRP report 103. For chronic exposures risks are halved.

Exposed Population	Cancer	Heritable	Total
Whole Life (0-85) (Sv^{-1})	5.5%	0.2%	5.7%
Adult Life (18-65) (Sv^{-1})	4.1%	0.1%	4.2%

Table 1.3: Detriment adjusted nominal risk coefficients per sievert for different populations (age and sex) from chronic radiation exposure. Data taken from ICRP report 103. These numbers try to encapsulate the detrimental effects and hence risks from both treatable and lethal cancers as well as heritable effects (mainly genetic diseases originating from radiation induced mutations in eggs and sperm stem cells).

is most commonly assumed to follow a linear model[1]. Data from the Hiroshima and Nagasaki atomic bomb survivors shows approximately a 16% risk of cancer in men and 18% in women per Sv with a (contemporary) mortality rate from these cancers of about 25%. The atomic bomb survivors were all subject to a single large irradiation, and longer chronic irradiation such as those associated with most occupational exposures is assumed to reduce these risks by around a factor of 2 [5, 16]. The uncertainties associated with these risks are large (around a factor of 2), and factors such as age of exposure, sex and individual variations in cancer susceptibility can vary them somewhat. As such they are only really suitable for application to populations, not individuals. Table 1.2 shows chronic cancer risks in men and women from the International Commission on Radiation Protection (ICRP) report 103 [5] and table 1.3 shows the detriment adjusted nominal risk coefficients from ICRP 103 - this number tries to encapsulate the risk of having a significant stochastic effect from radiation exposure and is 4.2% per Sv for adults.

Most workers who are occupationally exposed (i.e those who necessarily encounter radiation beyond natural background in their workplace) are exposed to relatively straightforward radiation fields often consisting of a single particle type. Examples

[1] Although this assumption is hotly debated below about 100 mSv [15]

might be gamma ray exposure for medical workers or radon for uranium miners [10].

Assessment of mixed fields is quite a different problem. Here we define a mixed field as one consisting of a wide range of particle types and a wide spectrum of particle energies (covering several orders of magnitude). Aviation fields for example consist of a mix of muons, photons, protons, pions and neutrons as shown in figure 1.1. Other mixed fields include cosmic rays in space (where dose rates are high $\approx 250\,\mu Sv/day$ - $1.5\,mSv/day$) and the fields around high energy particle accelerators.

Many neutron fields fall somewhere between these two extremes. Workers who are occupationally exposed to neutrons such as those in the nuclear power industry are often exposed to a relatively wide range of neutron energies mixed in with a gamma ray component.

Three different methodologies for assessing mixed fields are considered in this thesis. The first is to attempt to separate the components of the field in energy and particle type, and then calculate a response from these components. This is the approach followed in chapters 3 and 4. In chapter 5 a detector is designed in which the overall response of the detector to neutrons mimics that of the human body. Alternatively one can create a detector which measured the energy deposited by radiation on a biologically relevant length scale. These types of detectors are termed microdosimeter, and the potential application of a pixel detector with a gas sensor to this field is discussed in chapter 6.

1.3 Pixel Detectors

The detector which forms the focus of this thesis, the Timepix detector, is a hybrid pixel detector. Hybrid pixel detectors (typically) consist of a matrix of tens of thousands sensitive semiconductor diodes with a pitch typically around $30\,\mu m$ - $100\,\mu m$ and are further explored in chapter 2. The salient feature of hybrid pixel detectors for dosimetric applications is that they act like a kind of camera for the particles traversing them. Ionising radiation leaves characteristic tracks in the detector, which can be analysed to find out information about the particle. It is this ability to examine the track left by the radiation that makes a Timepix detector so useful for the analysis of mixed radiation fields. Some of these tracks gathered by a Timepix detector when exposed to cosmic rays are shown in figure 1.2.

Pixellated silicon harks back to an earlier age of particle physics where researchers

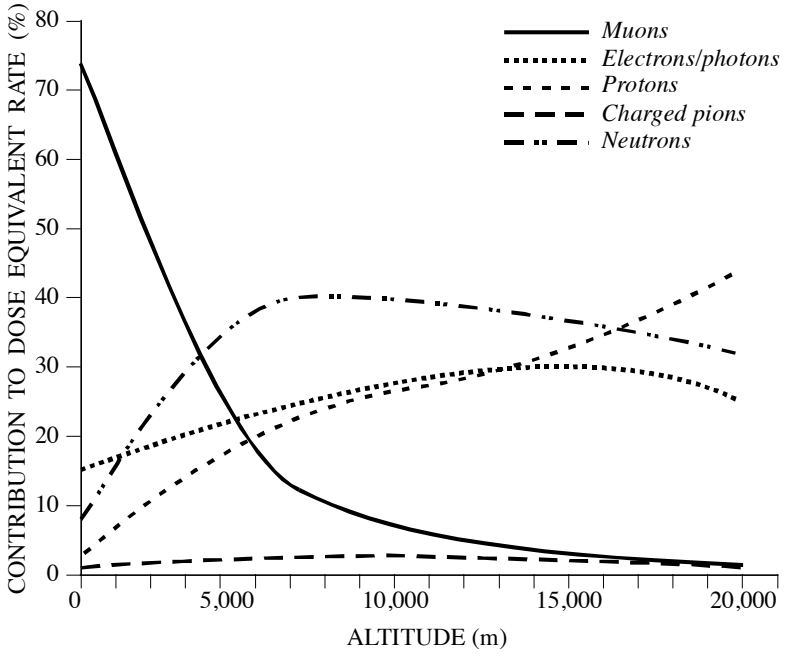

Figure 1.1: An example mixed field - contributions to the dose equivalent rate from cosmic rays as a function of flight altitude, reproduced from [10], original data from [17]. A commercial airliner flies at around 11 000 m to 12 000 m.

spent weeks pouring over nuclear emulsions searching for tracks left by ionising radiation. In an emulsion ionising radiation reduces silver halide into metallic silver along the path of its track. The emulsion is then left to develop for two to three hours and the analysis is carried out by hand, or in the modern era by computational examination of photographs. In pixellated silicon essentially the same process is carried out - ionising radiation creates electrons and holes along its track. These are then 'developed' in the silicon by transporting the electrons and holes to the pixel readout where the signal is processed by electronics and analysed by a computer. Unlike emulsion, the whole process in silicon takes a fraction of a second. Example collisions of cosmic rays with an atom measured in nuclear emulsion and a Timepix detector are shown in figure 1.3.

The unique proposition of hybrid pixel detectors is largely one of scale, economics and the onward march of semiconductor manufacturing and integrated circuit development. Modern pixel detectors take the sophistication of a last generation particle physics experiment[2], instruments that weighed tens to hundreds of kilograms and cost

[2]This is not an exaggeration, a Timepix contains approximately as many readout channels (65,536) as the vertex tracker of the ALEPH detector (73,728), a LEP era (1989-2000) experiment [19].

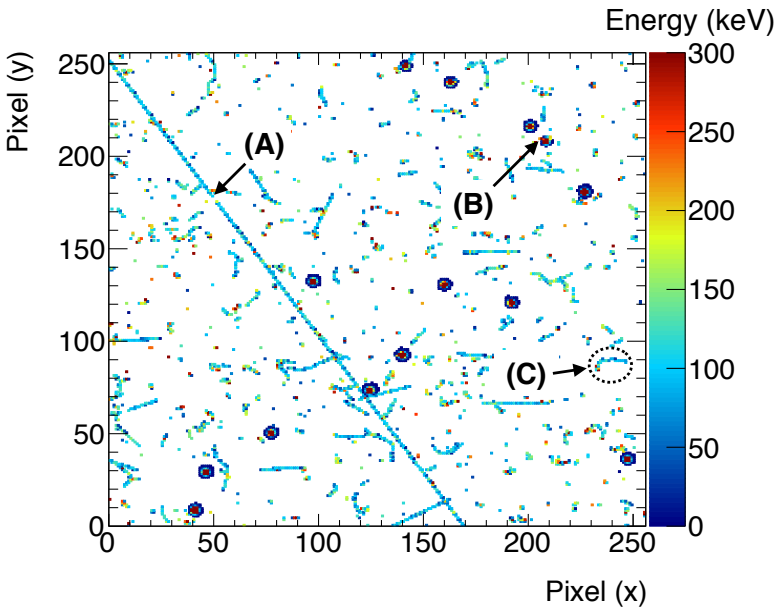

Figure 1.2: A 'snapshot' of the background radiation in Geneva, Switzerland captured over an hour in a Timepix detector. Each pixel is 55 µm long and 300 µm deep. **A** is a cosmic ray muon, the blob like objects at **B** are alpha particles from Radon. Curly tracks such as those at **C** are energetic electrons produced by the interactions of background gamma rays.

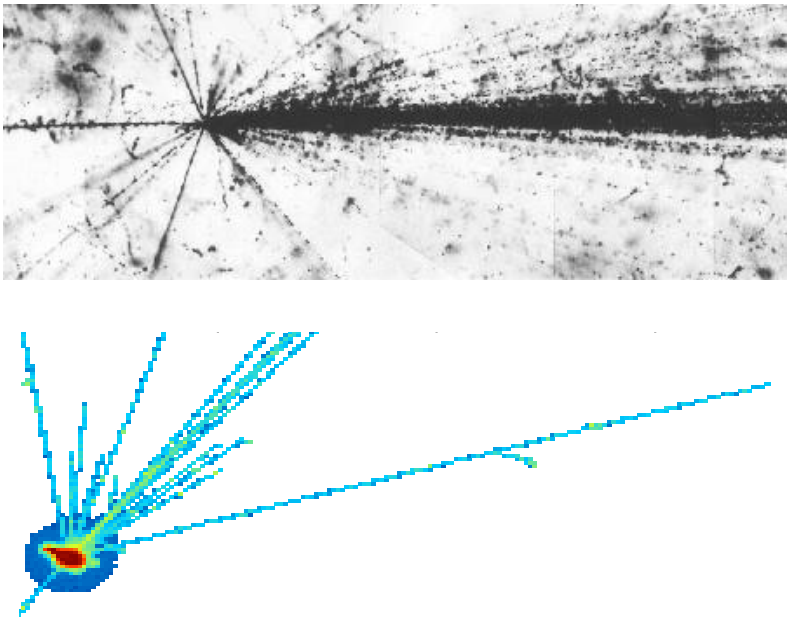

Figure 1.3: An incoming cosmic ray colliding with an atom captured in nuclear emulsion (top, reproduced from [18]) and a Timepix detector (bottom).

tens of millions of dollars and puts it into an instrument that the size of a fingernail (or finger including readout) the data from which can be readout on a home PC. Much like the development of the microprocessor which made computing generally available in the 1960's, the power of a device like the Timepix detector is not in its ability to make unique measurements in particle physics, but rather to take that sophistication to other fields such as radiation dosimetry and biology, and to environments where size and weight are key characteristics, such as space.

1.4 This Thesis - an Outline

This thesis outlines the work I have undertaken as a Marie Curie Fellow at CERN over the last 3 years.

- Chapter two discusses the physics of silicon detectors and the Timepix detector in particular. It describes how to set up and calibrate a Timepix detector.
- Chapter three discusses the basic interactions that form tracks in silicon detectors and how these tracks can be analysed to reveal physically relevant track parameters. It then provides an example of such an analysis carried out at the CERF facility at CERN. Chapter three shows how the morphological information in a track contains information separate from that measured by more traditional particle detectors (especially those used in radiation protection).
- Chapter four discusses the calculation of charged particle dose and its application to astronaut dosimetry on the International Space Station. It discusses how Galactic Cosmic Rays and the Earth's trapped charged particle belts contribute to the astronaut dose, and how the angular information gathered by tracking radiation on a per particle basis provides a unique advantage in space.
- Chapter five discusses neutron dosimetry and the development of a neutron dosimeter which provides an energy independent response for fast neutrons. Here the Timepix detector serves as a flexible testbed for the development of a device which can ultimately be used with a much simpler readout system. Its digital readout capabilities allow for the evaluation of the dosimeter response at a neutron time of flight facility.

- Chapter six discusses the initial characterisation and calibration of a Timepix which is used as the readout for a triple Gas Electron Multiplier detector, a device which offers the potential to inspect tracks at a far finer resolution than a silicon sensor. Its potential use in microdosimetry is discussed.

Chapter 2

The Timepix, Operation and Characterisation

This chapter describes relevant physics in the operation of semiconductor sensors and briefly covers the functionality of the Timepix hybrid pixel detector. It describes how to set up and calibrate a Timepix detector.

2.1 A Brief History of Position Sensitive Particle Detectors

Position sensitive silicon detectors evolved out of a need to very precisely measure interaction vertices (at resolutions of $\approx 10\,\mu m$) in fixed target particle physics experiments in the 1980's. At this time the technology of choice was crossed silicon strips. Silicon strips (as the name implies) consist of many long, thin strips of semiconductor detector arranged in a stripe pattern. The resultant detector is position sensitive along the axis perpendicular to the strip direction. By using a crossed geometry and operating the detectors in coincidence one can obtain 2D position sensitivity. By extending this to multiple planes in a telescope configuration particles can be tracked in 3D. Silicon was considered an attractive material for a detector because it has a small value for generating a single pair of charge carriers (3.6 eV) and a high density in comparison to the gas detectors prevalent at the time. This allowed measurable

signals[1] to be developed in thin sensors, and because of the relative ease and cost of manufacturing due to the extensive use of silicon in the microelectronics industry [20].

The primary problem with crossed strips is that the maximum count rate that can be obtained is insufficient for the needs of modern particle colliders. This is due to the prevalence of so called 'ghost tracks' with increasing particle fluxes. This is where more than one possible track is compatible with the readout of crossed strips. The obvious solution to this is further segmentation of the strips into pixels as shown in figure 2.1, however, the manufacturing of such devices is complicated by the need to have a readout which is sufficently compact to fit underneath the overlying semiconductor pixel[2]. In practice the development of such a readout was limited by the capabilities of the microelectronics industry to manufacture one, and the first pixel detector was built at CERN for the Omega-Ion experiment in 1992 [21, 22]. Rapid development of pixel detectors followed, and the inner trackers of all four LHC experiments (ATLAS, CMS, ALICE and LHCb) use silicon pixels.

2.2 The Physics of Semiconductor Detectors

2.2.1 The Band Theory of Solids

When atoms are brought together to form solids, the overlap of their electron orbits causes them to form 'bands' of continuous energy levels instead of the discrete orbital energy levels found in individual atoms. Typically the electrons in a material will fill the low energy bands which are called valence bands, and these bands will have no free electronic states. If an electrical field is applied across a material with a completely full valence band there is no current flow as there are no free states for electrons to move into[3].

The bands above this 'fill level' (the Fermi level) are empty and are called conduction bands. If an electron can be moved into the conduction band (typically by giving the electron extra energy, though thermal fluctuations, ionisation, absorption

[1] For the first applications of position sensitive silicon detectors which measured charm decays the high stopping power of silicon in comparison to gas detectors was also important, however in modern collider experiments the stopping power of silicon sensors is negligible.

[2] Strips can 'fan-out' their readout, the number of channels goes as $2A$ where A is the area to be covered, with pixels this goes as A^2 making a fan-out impossible for large area detectors.

[3] As per the famous Pauli exclusion principle that states that no two identical Fermions can occupy the same quantum state.

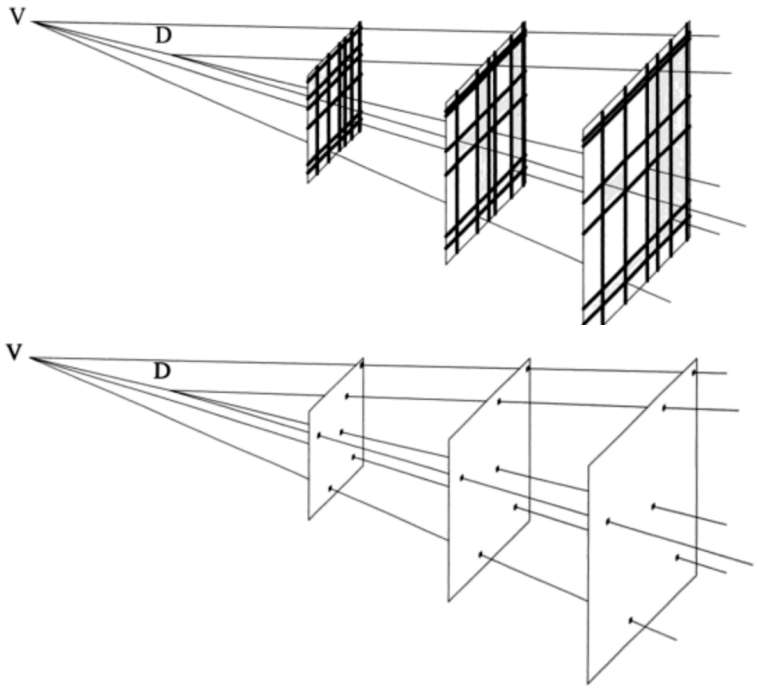

Figure 2.1: Crossed strips (top) vs pixels (bottom), from an event originating from vertex V with an interaction D, the interpretation of the data from the pixels is clearly much simpler. Figure reproduced from [20].

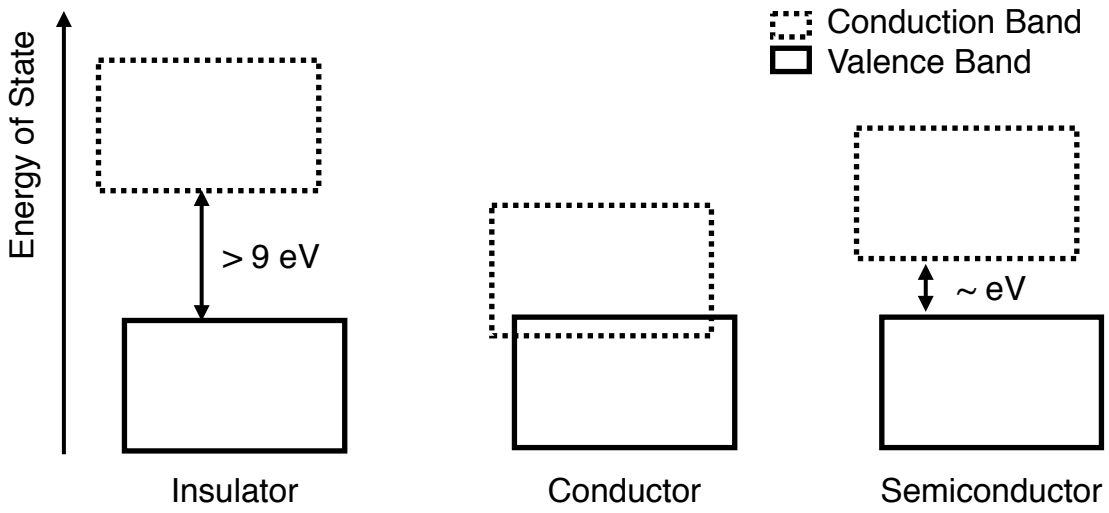

Figure 2.2: Electron band structure in solids, insulators and semiconductors.

of a photon etc) it can move freely, due to the excess of electronic states. Therefore the differences in electrical conductivity between insulators, conductors and semiconductors can be explained in terms of the accessibility of the conduction band as shown schematically in figure 2.2.

- In an insulator an electron must be given a large amount ($E \gtrsim 9\,\mathrm{eV}$) of energy to access the conduction band. This makes the conduction states completely inaccessible at room temperature where thermal fluctuations are $\approx 25\,\mathrm{meV}$.
- In a conductor the valence and conduction bands overlap. This means a substantial fraction of the electrons in the material are free to move under an applied electric field.
- In a semiconductor the separation between the valence and conduction bands (termed the band gap) is smaller than in an insulator. This typically means that it is possible to create a significant number of free charge carries through external action such as thermal action or excitation by ionising radiation.

In silicon it takes an average of 3.6 eV to promote an electron from the valence to the conduction band. Both the promoted electron and the positive vacancy it leaves behind, termed a 'hole' can carry charge. The conductivity of a pure semiconductor at a given temperature can then be calculated by working out how many electrons will be energetic enough to cross the band gap from thermal fluctuations.

Ionising radiation will also promote electrons into the conduction band, one electron per 3.6 eV of energy deposited in silicon. Because of this making a semiconductor radiation detector is easy in principle. One simply has to take a piece of semiconductor, and place an electric field across it large enough that any charge in the conduction band is transported to a readout. Each interacting particle will create a pulse of charge carriers. Unfortunately such a scheme is very difficult to make work. This is because in real semiconductor materials impurities inject electrons into the conduction band. This impurity induced conductivity dominates the signal from ionisation. It is, however, possible to create a region almost free of charge carriers with the use of doped silicon and the p-n junction structure, and this is how real semiconductor detectors work.

2.2.2 Charge Transport in Semiconductors

As a preface to discussing the p-n junction structure, the properties of charge transport in silicon are briefly discussed. Common properties are calculated for a 300 µm thick piece of silicon as this is the most common thickness found in Timepix detectors.

The drift velocity v of an electron/hole when an electric field E is applied is given by

$$v(z) = \mu E(z) \tag{2.1}$$

where μ is the electron/hole mobility. In silicon $\mu_e = 1350\,\mathrm{cm}^2/\mathrm{Vs}$ and $\mu_h = 450\,\mathrm{cm}^2/\mathrm{Vs}$. With a typical bias voltage of 100 V and 300 µm silicon sensor holes will take 20 ns and electrons 6.7 ns to drift the thickness of the sensor.

As charge moves through silicon it also diffuses into a gaussian charge cloud over time t with a width σ_y defined by the classical diffusion relation

$$\sigma_y = \sqrt{2Dt}. \tag{2.2}$$

The diffusion coefficient D is linked to charge carrier mobility by the Einstein relation

$$D = \frac{kT}{e}\mu. \tag{2.3}$$

If a voltage V_b is applied across the silicon, the average electric field is $\bar{E}(z) \approx V_b/d$ and the time t taken to traverse the sensor of thickness d is $t = d/v(z)$ then

$$\sigma_y = \sqrt{2Dt} \approx \sqrt{2\frac{kT}{e}\frac{v(z)}{E(z)}\frac{d}{v(z)}} = \sqrt{2\frac{kT}{e}\frac{d^2}{V_b}}. \tag{2.4}$$

So for a silicon sensor of thickness 300 µm with a voltage of 100 V applied at 300 K the diffusion full width half maximum $= 2.35\sigma = 19$ µm.

2.2.3 Semiconductor doping

In reality, the conductivity of all practical semiconductors is dominated by impurities which inject additional charge carriers. By artificially adding impurities the conductivity of the semiconductor can be precisely controlled. This process is called doping. Impurities can either add extra electrons (termed n type doping) or take away valence band electrons and so add extra holes (p type doping). Semiconductors with large amounts of doping have high conductivity and are hence termed low resistivity, and lightly doped semiconductors similarly have low conductivity and are so termed high resistivity. As the concentration of charge carriers introduced by doping is much larger than the intrinsic number of thermally generated carriers the conductivity σ and resistivity ρ are related to the doping concentration N by:

$$\sigma = e\mu N \qquad \rho = \sigma^{-1} = (e\mu N)^{-1}. \tag{2.5}$$

2.2.4 P-N Junctions and Radiation Detection

In a p-n junction a piece of p type and n type semiconductor are produced in the same structure by selectively doping the semiconductor. As the free holes in the p region and electrons in the n region diffuse they will occupy the donor and acceptor sites building up opposite space charges on either site of the boundary. This serves to create a region

between at the p-n boundary which is almost entirely free of charge carriers. This region is called the depletion region. A diagram of the arrangement of charge carriers in a p-n junction is shown in figure 2.3. This space charge also creates a potential across the junction and any charge carriers created in this region are immediately swept out in opposite directions, electrons towards the n doped region, and holes to the p doped region. As the number of thermally excited carriers is typically low[4] the generation of many (typically several thousand) charge carriers by the interaction of ionizing radiation causes a distinctive, distinguishable pulse.

Semiconductor detectors are usually operated in reverse bias. In this mode an external bias voltage V_b is added which is normally much larger than the natural potential of the junction. The added potential causes additional accumulation of charges in the acceptor and donor sites of the p and n regions, which in turn widens the depletion region following equation 2.7. A depletion region with the same width as the thickness of the detector is termed fully depleted and is clearly advantageous as the whole silicon volume is now sensitive to radiation. Voltages exceeding this value serve to over deplete the detector. The advantages of over depleting a p-n junction are largely that the charge collection time is faster and the diffusion smaller following equation 2.4.

The width W of the depletion region is given by

$$W = \sqrt{\frac{2\epsilon V_b}{eN}} \tag{2.6}$$

where ϵ is the material permittivity $\epsilon_r \epsilon_0$. The bias voltage at full depletion can be found by setting W to the thickness of the sensor

$$V_b = \frac{eNW^2}{2\epsilon}. \tag{2.7}$$

In silicon sensors the applied electrical field cannot go much above $10^4\,\mathrm{V\,cm^{-1}}$ - $10^5\,\mathrm{V\,cm^{-1}}$ due to avalanche multiplication (where one electron gains enough kinetic energy from the electric field to create addition electron/hole pairs creating an avalanche like effect). For a 300 µm sensor this effectively constrains the bias voltage

[4] In silicon, other detectors will smaller band gaps may need to be cooled.

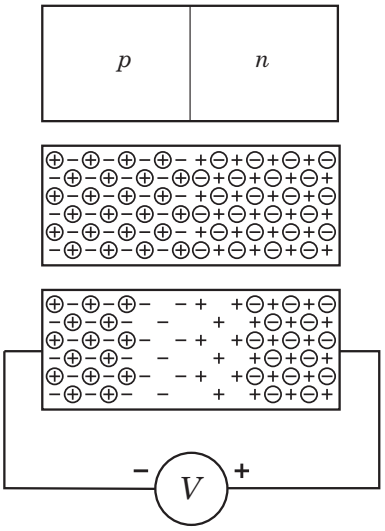

Figure 2.3: A p-n junction. When p type and n type semiconductor are brought together the mobile charge on both sides (circled) is attracted to the opposite sides of the boundary creating a region depleted of charge carriers. An external voltage can be added which serves to enhance this effect. Figure reproduced from [23].

to 200 V - 300 V. If one wishes the entire thickness to be fully depleted the resultant doping concentration must be quite low; $N \approx 10^{11}\,/\mathrm{cm}^3 - 10^{12}\,/\mathrm{cm}^3$, which is much lower than that used in commercial microelectronics [23]. The need to have the sensor and the readout electronics made from very different silicon leads to the hybrid pixel detector concept.

2.2.5 Hybrid Pixel Detectors

The essential principle of a hybrid pixel detector is that the semiconductor sensor and microelectronic readout are fabricated separately and then joined together. Typically the sensor will be made of high resistivity silicon or another semiconductor material such as CdZnTe, GaAs or Diamond. The readout is made using low resistivity silicon using normal fabrication techniques from the microelectronics industry (for example the Timepix is manufactured in a 250 nm CMOS process from IBM).

A typical sensor is usually quite asymmetric being made from a large wafer of lightly doped (n or p) silicon width individual highly doped (p+ or n+) shallow implants in the bottom few micrometers of the silicon. When operated in reverse bias the depletion region then extends up from the implants into the bulk. The electrical contacts are

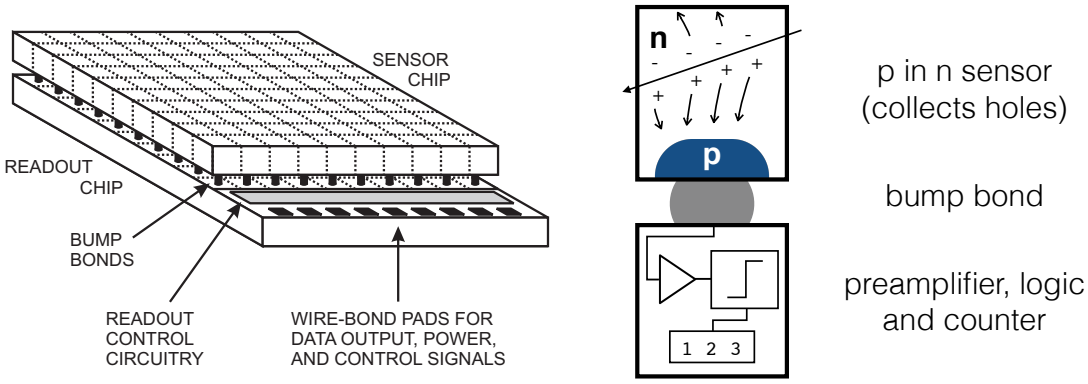

Figure 2.4: (Left) hybrid pixel detector layout, figure reproduced from [23], (right) schematic of operation of typical pixel with p in n sensor, the top is a high resistivity semiconductor sensor bump bonded to readout electronics.

typically metallised with aluminium. On the n side of the sensor the aluminium can be several microns thick which also provides light tightness. Figure 2.4 shows a diagram of the whole of a hybrid pixel detector and an example individual pixel.

2.3 The Timepix Detector

The Medipix collaboration was formed to take hybrid pixel detector technology from particle physics and apply it to single photon counting. The detectors have been very successful and are finding applications is a very wide variety of fields outside of high energy physics. These include (but are certainly not limited to...) colour x-ray imaging [24], phase contrast x-ray imaging [25], colour CT [26], charged particle tracking [27], charged particle dosimetry [28], radon dosimetry [29], brachytherapy seed imaging [30], use as an educational tool [31, 32] and mass spectrometry [33].

The Timepix ASIC is a spin off of the Medipix2 ASIC, and its applications are the main focus of this thesis. It consists of a 256×256 pixel CMOS ASIC. Each pixel measures $55 \times 55\,\mu m^2$. The term Timepix refers to the readout system which is often (but not exclusively) used with $300\,\mu m$ thick p in n silicon sensors. Typically when used with a semiconductor material the detector preamplifier pads are individually connected to the overlying semiconductor pixel through Flip Chip bump bonding [34]. The Timepix can measure both positive and negative currents (i.e. holes and electrons)

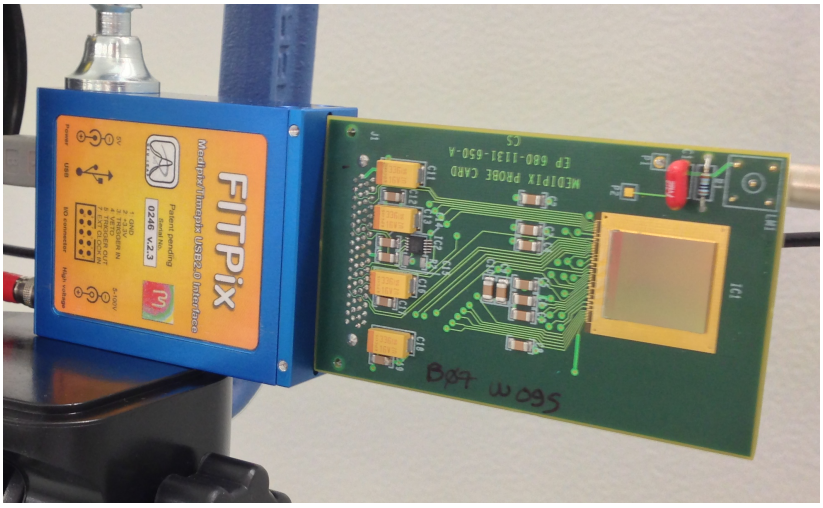

Figure 2.5: Photograph of a Timepix Detector mounted on a CERN probe board and FITPix [35] readout.

allowing for the use of a wide variety of semiconductor sensors. A photograph of a Timepix detector and readout are shown in figure 2.5.

A brief note must be made here about terminology. If the *Timepix detector* is referred to in the text, this refers to the Timepix bump bonded to (unless otherwise noted) a 300 µm thick p in n silicon sensor. The terms *Timepix ASIC* or *Timepix* refer solely to the ASIC, without reference to any attached sensor. The term *Timepix sensor* refers to the attached pixellated silicon sensor.

2.3.1 The Timepix Pixel

Each pixel in the Timepix contains a preamplifier, discriminator threshold, 14 bit counter and can operate in one of three modes:

- Medipix - photon/pulse counting.
- Time Over Threshold (TOT) - charge measurement.
- Time of Arrival - measures the arrival time of a pulse.

Figure 2.6 shows a schematic of the pulse processing in the Timepix. In Medipix mode the chip counts the number of times the signal goes higher than the threshold. In TOA mode the chip measures the particle arrival time by counting from when the preamplifier goes high on the discriminator to the end of the acquisition (which can be

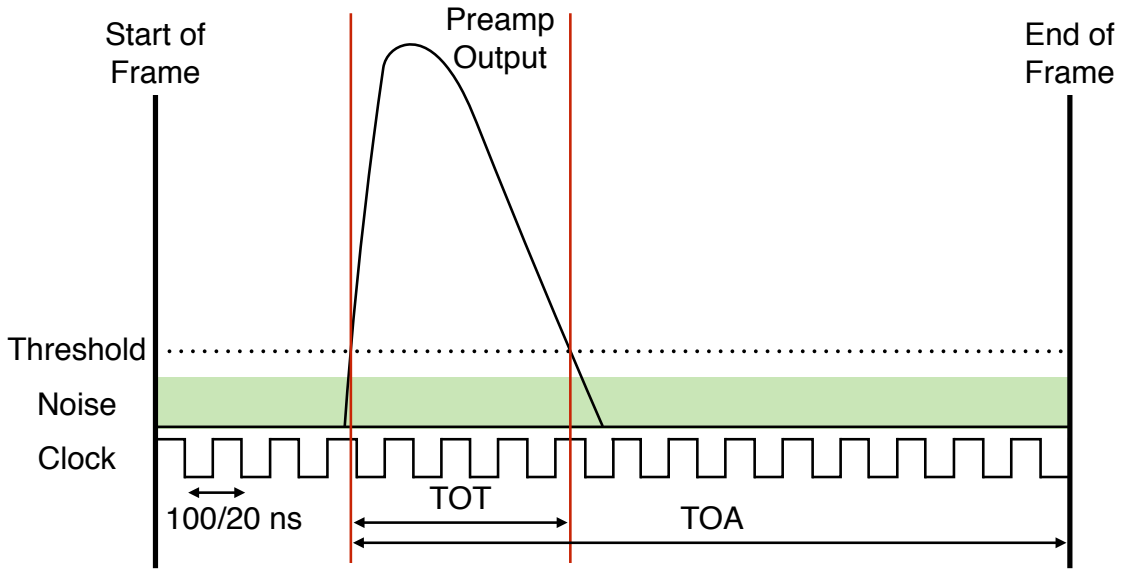

Figure 2.6: The TOT mode in the Timepix ASIC measures the time elapsed while the preamp output is high against the threshold discriminator. TOA mode measures the time from when the preamp goes high against the threshold until the end of the acquisition frame. Medipix mode counts once for each pulse.

triggered in hardware, or in software). In TOT mode whenever the pulse is high against the discriminator the pixel counts until the pulse is low again. This allows each pixel to act as a Wilkinson type ADC measuring the discharge time of the preamplifier (i.e. the time spent over the threshold). The minimum threshold is about 1000 electrons or 3.6 keV with a silicon sensor. As each pixel is individually programmable, it is possible to operate different pixels in different modes during the same acquisition. In chapter 6 we exploit this feature to operate the detector in a so called 'mixed mode' where 1 in every 16 pixels measures TOA while the rest measure TOT[5].

TOT and TOA measurement are carried out using a global clock which is synchronised across the chip. This clock can run at several different frequencies, 1.8 MHz, 9.6 MHz, 48 MHz and 96 MHz. In general the 96 MHz mode can be quite unstable. Operating at a higher frequency provides better time resolution in TOA mode at the cost of maximum frame length as explained in section 2.3.2.

An important point is that the pulse length in each pixel is relatively long, normally between a few hundred nanoseconds and several microseconds for photons depending

[5]In Pixelman, this feature can be accessed by using the 'load mode mask' option.

on the input charge and the IKrum current (see section 2.3.3).

2.3.2 Chip Operation

All of the measurements carried out in this thesis use *Pixelman* [36]. Pixelman is the software package developed for read out using the FITPix [35] by IEAP at CTU Prague. In the default configuration Pixelman provides a graphical user interface for setting up the detector and acquiring measurements. It also ships with a plugin for performing a threshold equalisation (section 2.4.1), a plugin for performing DAC scans including threshold scans (section 2.4.4) and other various plugins are available on request from IEAP for data analysis. In general the author only uses Pixelman as a tool for data acquisition and performs analysis with other tools. To get the most out of a pixel detector, experience with data analysis in a computer programming language and access to a plotting and fitting library are recommended - two common choices are C++/ROOT and Python/Matplotlib.

The Timepix operates with a frame based read out. This means that the Timepix has a digital shutter which operates in much the same way as the shutter on a camera. The shutter is opened at the start of the measurement and the digital electronics in the chip carry out pulse processing for the period that the shutter is open. When the shutter closes the values in the pixel registers are read out of the chip and once this has been performed the chip can be used again. The chip can either be read out using a built in serial or parallel bus. The FITPix read out used for these measurements utilises the serial bus and takes about 12 ms to read out the chip and hence the maximum achievable frame rate on a fast computer is about 80 frames per second. Read out interfaces using the parallel bus can achieve around a 1 ms read out but tend to be both specialised in application and expensive.

The maximum frame length depends on the mode of operation. Each pixel can count up to 11810. In Medipix mode the frame length should be sufficiently short that the counter does not saturate. In TOT mode the same requirement applies, but a user is often interested in measuring the events from single particles which may leave characteristic tracks of hit pixels. In this case the frame length should be short enough that tracks do not overlap. In TOA mode the maximum frame length is much more restricted. As the chip counts from when a pixel goes high to the end of the frame the time measurement is limited to 11810 multiplied by the period of the Timepix clock

to avoid hits from the start of the frame saturating the counter. This time is 1.23 ms at 9.6 MHz and 246 µs at 48 MHz.

The Timepix does not contain overwrite/underwrite protection logic. This means that if pixels are high at the start of a measurement they will immediately start counting, and if they are high at the end immediately stop counting. This can lead to errors, most noticeable in TOT measurements with very short (≈100 µs or less) frame lengths, especially with charged particles which may deposit a large amount of charge in a single pixel and have TOT times of 50 µs or higher.

2.3.3 Timepix DAC's and settings, a Quick Guide

Most of the Timepix settings as configured in Pixelman are optimal for the operation of the chip, this section provides a short overview of the commonly used DAC's and their effect on chip performance.

- THL - Threshold DAC, sets and controls the threshold.
- THLC - Coarse threshold DAC, sets the size of the physical voltage step per THL DAC step
- FBK - Feedback DAC. Adjusting this DAC moves the position of the threshold relative to the THL DAC. The 'real' threshold voltage of the chip is given by subtracting the THL voltage (not DAC value) from the FBK voltage.
- THS - Sets the step size for the per pixel threshold adjustment. Common values are between 60 and 85, if this value is correctly set then the distribution of pixel adjustment bits should be gaussian (see section 2.4.1)
- IKrum - Input current for Krummenacher amplifier. Higher values steepen the slope (i.e reduces the discharge time) of the preamplifier. In general higher IKrum values work well for photon counting mode, while lower values provide better resolution for TOT mode.
- Clock frequency - Frequency of the Timepix clock in MHz .

2.4 Characterising the Timepix

2.4.1 Threshold Equalisation, setting the threshold

The voltage level of the threshold in each pixel naturally varies somewhat due to the intrinsic nature of semiconductor manufacturing. To help compensate for these variations each pixel in the Timepix comes with a 4 bit (16 step) threshold adjustment setting. This changes the threshold in each pixel by a small amount. The step size of the per pixel THL adjustment is adjusted by the THS DAC.

The essential process of threshold equalisation is then to use a feature of a fixed energy to align the thresholds. The most convenient feature, that is available without external irradiation is the noise, which is used by the Pixelman threshold equalisation plugin. The results of threshold alignment using this plugin are shown in figure 2.7.

Two methods of 'finding the noise', i.e. the fixed reference point are provided in Pixelman. In both cases a DAC scan in THL is carried out on all pixels. The first is the 'noise edge' which defines the noise as a pixel (in medipix mode) counting over a certain value. The 'centroid' method attempts to find the center of the noise distribution (which is a gaussian). As the noise width in each pixel varies somewhat the centroid method should provide a uniform absolute threshold response across the whole chip and is generally recommended. The edge method provides a narrower transition in and out of the noise, and is useful for operating the chips at low thresholds.

Following equalisation the threshold (THL DAC) is set some number of DAC counts away (in hole counting mode the threshold is lowered as the positive holes produce a 'negative' current). Typically this is about 30, but in general it will be until the majority/all pixels are noise free. Often one or two pixels will be persistently noisy and should be masked.

2.4.2 Measuring the Sensor Depletion Voltage

The classical way to determine the full depletion voltage of a silicon p-n junction is to perform a capacitance/current scan. However due to the compact and generally preassembled nature of hybrid pixel detectors this is not always possible. Instead one solution is to measure the number of medipix counts (i.e. the number of detected photons) from an external photon source as a function of applied voltage. The depletion region extends out from the p wells at the bottom of the sensor, so as the bias voltage

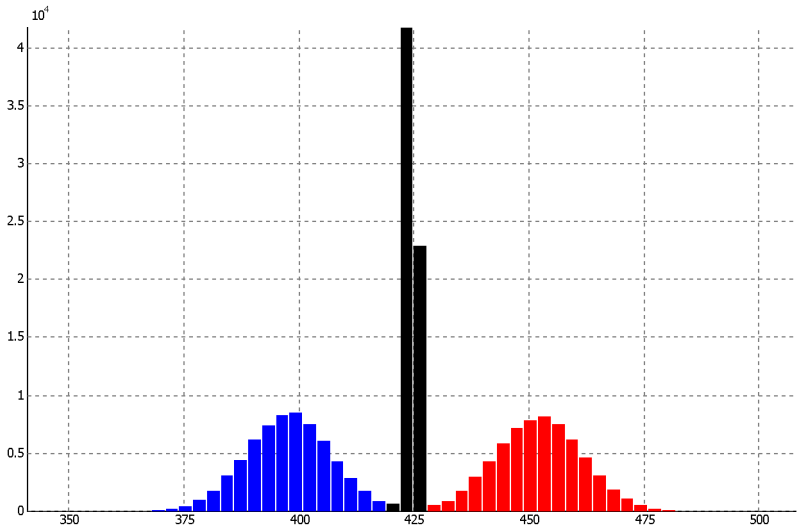

Figure 2.7: Screenshot of a threshold equalisation from Pixelman. The histogram shows the THL value of pixel noise centroids for trim = 0 (blue), trim = 15 (red) and trim equalised (black).

is increased the sensitive region of the sensor will extend upwards. As the depletion region extends more photons will be counted up to some plateau value when the entire sensor is sensitive. The results of such a scan are shown in figure 2.8, in this case a 500 µm sensor is full depleted at $\approx 100\,\mathrm{V}$. If the depletion voltage is known then the sensor doping concentration N and hence the resistivity ρ can be estimated from equations 2.7 and 2.5:

$$N = \frac{2\epsilon V_d}{eT^2} \qquad \rho = (e\mu N)^{-1}. \tag{2.8}$$

Given a depletion voltage of $\approx 100\,\mathrm{V}$ and sensor thickness $T = 500\,\mu\mathrm{m}$:

$$N \approx 5.1 \times 10^{11}\,/\mathrm{cm}^3 \qquad \rho \approx 27\,\mathrm{k}\Omega\,\mathrm{cm}^{-1}. \tag{2.9}$$

2.4.3 Photon Hits and Charge Sharing

Further characterisation of the Timepix detector uses x-ray photons (5.9 keV - 60 keV). The physics of photon interactions with silicon are covered in section 3.2.3, but in this energy range it is safe to assume that for a majority of photons the energy of the

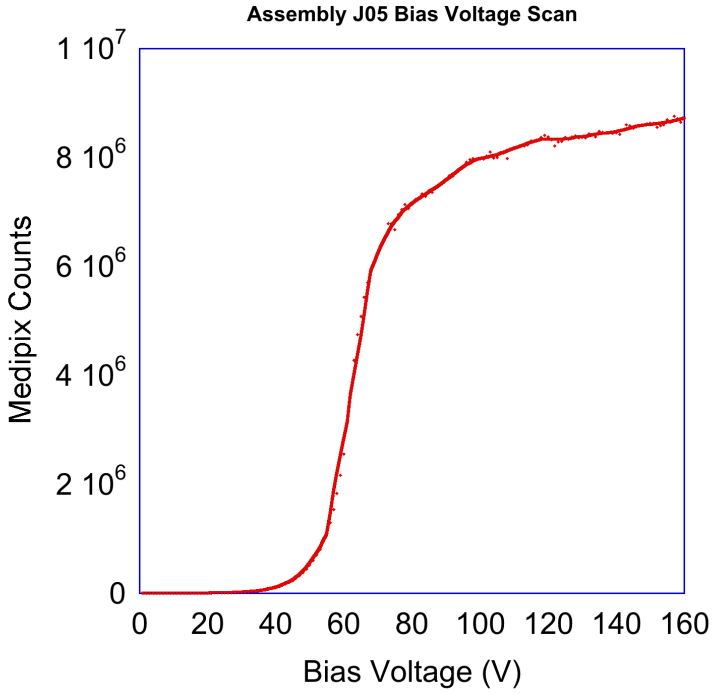

Figure 2.8: Number of Medipix counts as a function of applied sensor bias voltage for a 500 µm thick Timepix detector with an external ^{55}Fe source. In this case the sensor is fully depleted at ≈ 100 V.

photon is entirely transferred into a photoelectron[6], which then stops in a negligible distance in the silicon pixel.

The electrons created by photon interactions can however spread their charge over multiple pixels thanks to the charge sharing effect. When charge is transported through the sensor it can diffuse, and if the interaction of an electron occurs near a pixel boundary then the charge can be spread between two pixels. More unusually, the electron can interact on the boundary of three pixels, or even four [27] as shown in figure 2.9.

If the charge shared into a pixel is less than the pixel threshold then that charge is 'lost' to the measurement. As the relationship between TOT and input photon energy/charge is not linear (see section 2.4.5) the summed TOT counts from clusters with different numbers of hit pixels will not be the same for the same charge deposition

[6] Actually a photoelectron *and* a 2 keV Auger electron.

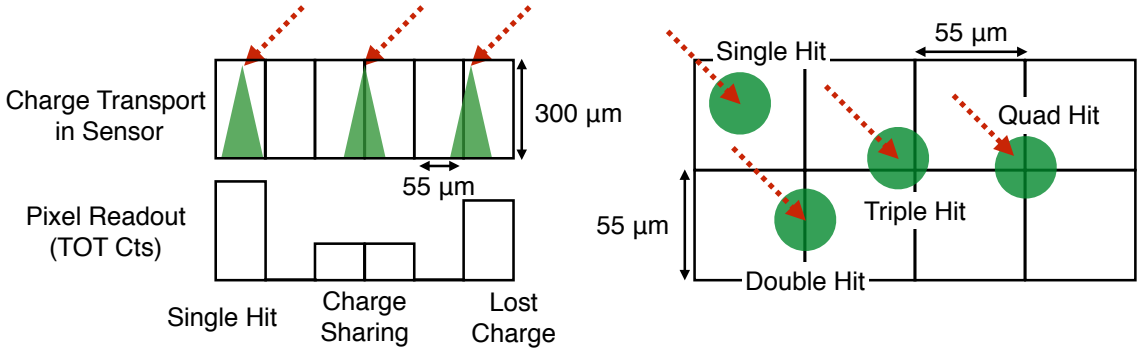

Figure 2.9: Effects of charge sharing in a Timepix detector. Shown side on (left) with a single photon hit, a double hit resulting in less total TOT counts due to the nonlinearity in the low energy TOT response and lost charge. Right shows a top down view of the sensor and the origin of single, double, triple and quad hits.

(i.e. a 2 pixel hit from a 15 keV photon will have more TOT counts than a 1 pixel hit). Figure 2.10 shows this effect in a TOT spectrum for a ^{241}Am source.

2.4.4 Threshold Energy Calibration

It is quite useful to calibrate the set threshold DAC value to the physical threshold in keV. The essential principle behind a threshold scan is that as the threshold voltage is raised at some point the signal that this threshold corresponds to will pass beyond the signal induced by a photon of given energy and the photon will no longer be detectable. For a normal gamma ray line a plot of the number of detected photons against threshold the result would in principle be a step function, with the step located at the threshold corresponding to the emission energy of the photon. In reality the step is broadened into a sigmoidal shape by the intrinsic energy resolution of the detector.

This line can then be differentiated. This produces a Gaussian peak, which can be fit to find the threshold DAC value corresponding to the emission energy of the line. To avoid excessively long measurements it helps to first smooth the data (a simple moving average works well) and then differentiate it using a simple algorithm such as a five point stencil.

By plotting several threshold values against the photon energy one can obtain a calibration curve of threshold against energy. An example of the whole proceedure, including a differentiated threshold scan for an Iodine 125 Brachytherapy seed is shown in figure 2.11. Once this curve is obtained the threshold energy can easily be read out.

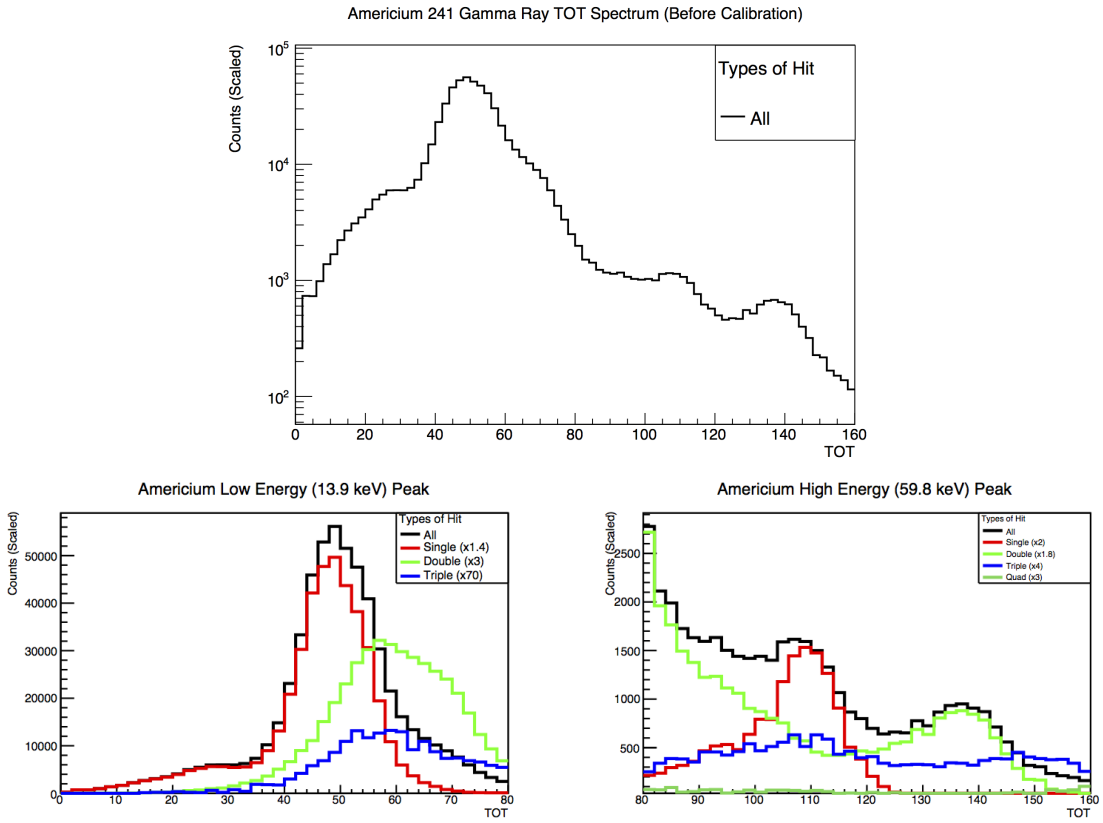

Figure 2.10: TOT Spectrum of ^{241}Am source measured by a Timepix detector, the spectrum exhibits extra peaks beyond the two expected. The figures at the bottom show the spectrum split into single, double, triple and quad hits. The extra peaks are clearly due to non-linearities in the TOT response where the charge from a single photon is spread over multiple pixels. Figure 2.13 shows the corrected version of this spectrum after per pixel energy calibration.

As well as being generally useful to know for detector operation, this threshold value is helpful when performing an absolute energy calibration of the detector as described in the next section.

A subtle distinction should be made between the number of counts, and the number of detected photons. As the threshold is lowered, the number of pixel counts per photon increases because more hits from charge sharing become detectable, yielding a broader gaussian. The solution to this problem is to separate the data into individual groups of hit pixels, each one of which should correspond to the interaction of one particle. This procedure is called clustering and is explored in more detail in chapter 3. The use of such a procedure excludes the use of high count rate sources as the occupancy of each frame should be low enough so that particle hits do not overlap, and hence dramatically increases the time required to carry out this measurement.

2.4.5 TOT Energy Calibration

The TOT response of the Timepix detector to energy is non-linear for low input charges and linear for charges above about 5000e- (20 keV). The calibrated response of a single pixel is shown in figure 2.12. In general the response of TOT to input energy E has been shown to follow the general shape of a 4 parameter surrogate function shown in equation 2.10 with a non-linear parameters c and t and linear parameters a and b [37]

$$\mathrm{TOT} = a + bE + \frac{c}{t - E}. \tag{2.10}$$

The simplest way to calibrate a Timepix detector is to perform a calibration treating all of the pixels as if they have a uniform response. In carrying out such a procedure one measures the TOT value of single pixel hits and then fits the most probable value of the resultant spectrum to the pixel energy. Typically this procedure is carried out with at least 4 spectral lines, normally ^{55}Fe (5.9 keV), the ^{241}Am peak at 59.5 keV and at least 2 x-ray fluorescence lines between these two values, preferably in the non-linear part of the curve. Photon based calibration after this limit becomes difficult as the electron range starts to commonly exceed 1 pixel and the Compton effect (section 3.2.3) becomes important. Extrapolation of the linear part of the curve is perfectly acceptable, until ≈ 1 MeV per pixel at which point other effects (section 2.4.6)

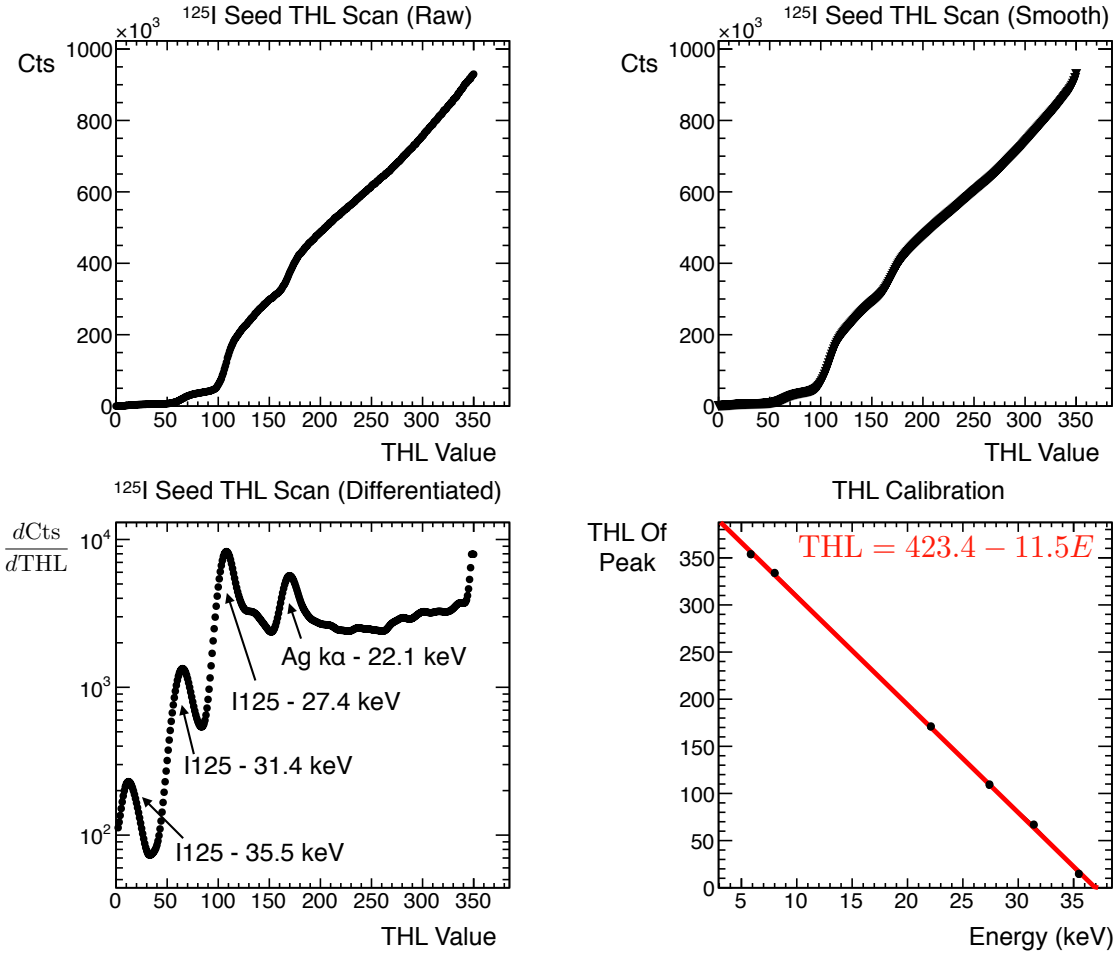

Figure 2.11: Threshold energy calibration for a Timepix detector with ^{125}I, (top left) number of Medipix counts as a function of THL DAC value, each 'kink' is the threshold passing below the energy of a new gamma ray line, (top right) number of medipix counts, smoothed, (bottom left) differentiated, smoothed spectrum with 4 clearly distinguishable peaks (the silver peak is from the source packaging), (bottom right) resultant THL calibration. The points at 5.9 keV and 8.0 keV are from ^{55}Fe line and Cu fluorescence respectively (THL scans not shown).

start to become important.

One issue with fitting 4 points with a 4 parameter function is that there is a fairly large number of convergent fits, most of which do not reflect the reality of the calibration curve. There are several ways to ameliorate this situation. One procedure that can help with this is to fix the linear part of the curve by using two sufficiently high energy photon lines ($> 25\,\mathrm{keV}$) and then to only vary the non-linear parameters c and t in a variation of the procedure described by Jakubek [38]. Alternatively one can use the procedure outlined in [38] where the a and b parameters are determined by the linear part of the curve and then used in a fit to the lineshape of the ^{55}Fe TOT spectrum from which the c and t parameters can be determined. The author uses a fairly conventional method, identifying all four peak values from the most probable values in the spectra and then using an additional fifth point, where the energy threshold (section 2.4.4) is matched with a TOT value of 0.

Per-pixel energy calibration is essentially an extension of the procedure outlined in the previous section, the principle difference being that a surrogate function is fit for all 65,536 pixels instead of treating the matrix monolithically. This approach is obviously advantageous as it compensates pixel to pixel variations, which are an inherent feature of semiconductor manufacturing. The principle differences between the full matrix and per pixel approach largely involve measurement and computation time. In general 1000 single photon hits are needed to construct a reasonable response to a single spectral line. This means that 65 million single photon hits are required for a source with low charge sharing to many more hits for a source with a wide spectrum and a large amount of charge sharing such as ^{241}Am. Given a high activity (such that a measurement at a the maximum frame rate of ≈ 80 fps has frames with ≈ 4000 hits, typically such a source is $> 10\,\mathrm{MBq}$) source or x-ray tube and a fast computer the measurement of a single spectral line in all pixels can be carried out in approximately two hours. With more typical lab sources, measurements of an individual line typically have to be run at least overnight. Running the calibration procedure then takes approximately two additional hours on a relatively fast computer.

A key advantage of performing such a non-linear calibration is the removal of extra peaks in the cluster TOT spectrum. These originate when, for example the energy of one photon is fully absorbed in a single pixel, while a different photon can split its energy between two pixels. The resulting summed non-linear response of multiple pixel clusters results in characteristic shifted peaks in TOT, which are aligned when

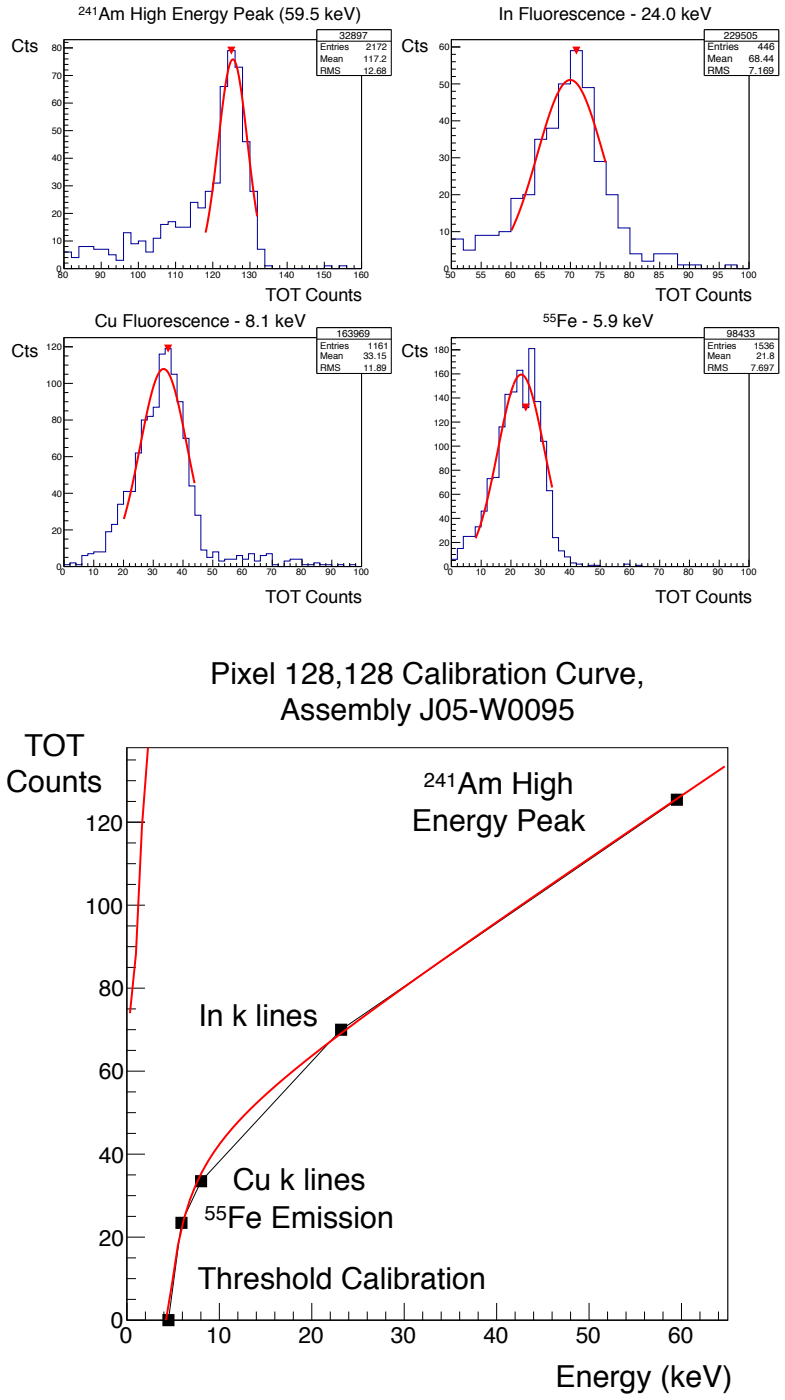

Figure 2.12: Peak fit for one pixel. The top panels show the distribution of TOT counts from 4 different sources, the bottom panel the resultant calibration fit.

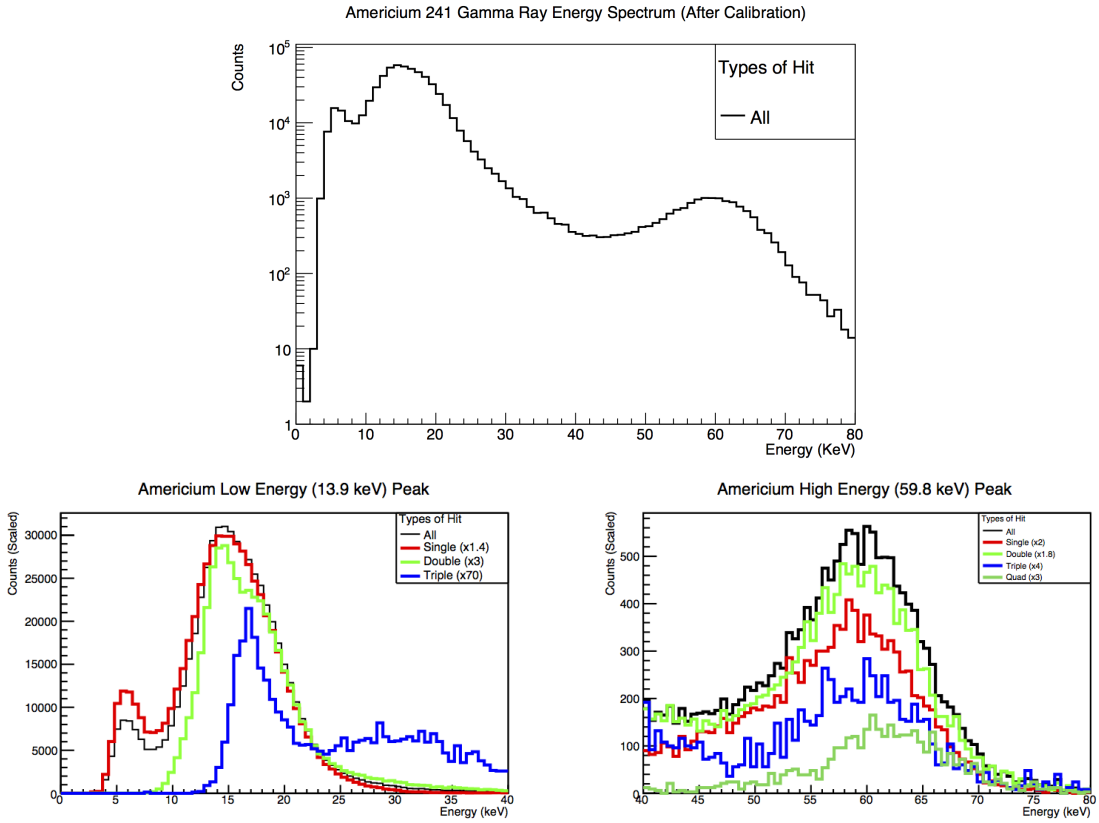

Figure 2.13: Energy spectrum of ^{241}Am photons after per pixel energy calibration. In contrast with figure 2.10 there are two spectral peaks instead of four, and the peaks from different numbers of cluster hits are aligned.

the energy calibration is applied. The result of such a per pixel calibration is shown in figure 2.13.

2.4.6 High Energy Calibration

Above approximately 800 keV - 1.2 MeV per pixel the energy response of the Timepix detector becomes nonlinear. This is due to a bug in the Timepix preamplifier that causes preamplifier output to oscillate above a certain input charge [39]. The effect of this is that the gain of the pixel changes above a certain threshold input charge, this can be corrected with a recalculation of the a and b parameters. An example recalculated calibration curve is shown in figure 2.14.

I will briefly describe one method for obtaining such a curve. Such a method is approximate, and negatively effects the energy resolution above the threshold value. This method uses monoenergetic charged particles, these can be obtained using alpha

particles from ^{241}Am in vacuum for example, but in this method we use monoenergetic 7 MeV protons incident at 40° produced at the Van de Graaff Tandem linac at INFN Legnaro. Such particles create an extended cluster of pixel hits formed by a combination of the physical track of the particle and charge sharing, this is further discussed in section 3.1. As the protons are relatively slow they stop in the silicon, depositing all their energy. The key point for this method is to select clusters where only a single pixel is responding non-linearly[7]. From this the 'real' energy in the pixel can then be constructed as the 'good' energy measured by the other pixels subtracted from the incident particle energy. Then a calibration curve can be constructed.

First one has to select clusters where only one pixel counts above some threshold value, for example 800 keV. A spectrum of detected events that fit this criteria is shown in the top right panel of figure 2.14. Clearly visible are two peaks, one where all the pixels respond normally and another with non-linearly responding pixels. The normally responding peak can then be fit to determine the energy E of the incoming radiation making this method relatively insensitive to machine energy variations. If the measured energy in the normally responding pixels is E_g then the 'real' energy in the hottest pixel is $E - E_g$. A plot of this value against the measured energy E_m can then be used to calculate a relationship between the measured and real energy as shown in the middle panels of figure 2.14.

Finally, the recalculated calibration parameters a_n and b_n can be worked out with some simple algebra as described below.

$$\mathrm{TOT} = a + bE - \frac{c}{t - E} \tag{2.11}$$

$$\mathrm{TOT} = a + bE_m \tag{2.12}$$

$$\mathrm{TOT} = a + b\frac{E - p}{m} \tag{2.13}$$

$$E = mE_m + p \tag{2.14}$$

$$\mathrm{TOT} = a_n + b_n E \qquad a_n = a - \frac{p}{m} \quad b_n = \frac{b}{m}. \tag{2.15}$$

When the recalculated curve is applied to the data it restores the expect line shape,

[7] If a source is used in which there are not many clusters with a single non-linear pixel, the bias voltage can be varied which will change the amount of charge sharing. In this way the bias can be used to tune the amount of charge in the central pixel of a cluster.

with some impact on the energy resolution (bottom panels of figure 2.14).

The volcano effect causes some pixels with a very high amount of charge (i.e. several MeV or above a million holes) to not count in some situations [40]. It is further discussed in section 3.2.7.

2.4.7 Test Pulses

Test pulses provide a way to inject a set amount of charge into a pixel using circuitry built into the Timepix ASIC. In theory this input charge can be used for calibration avoiding the need to use photon sources, although such a method of calibration only compensates for intrapixel variations in the ASIC, not in the silicon sensor. Unfortunately the Timepix test pulse functionality does not accurately reproduce the c and t parameters of calibration curves produced using the photon method, an issue that is explored in detail in [39]. Test pulses can be used to measure the a and b parameters reasonably successfully.

2.5 Other ASIC's in the Medipix Family

- Medipix 2 [41] - The Medipix 2 is essentially identical in functionality to the Timepix with the significant difference that only the Medipix mode is available. The Medipix also offers two (instead of one) discriminator threshold,s allowing the chip to operate in an energy window mode where it only counts pulses between the low and high thresholds.

- Medipix 3 RX [42] - Medipix3 is the latest version of the Medipix chip designed for photon counting. It contains a charge summing mode, that adds charge from neighbouring pixels to compensate charge sharing

- Timepix 3 [43] - The Timepix 3 is the latest version of the Timepix chip. At the time of writing chips are widely available, but read out systems [44] are not. The Timepix 3 uses a data driven output which pushes the data from pixels out when the preamplifier goes low. The maximum data rate is 85 MHits/sec. Timepix 3 offers 1.5 ns time resolution, 24 bit counters and the option of simultaneous TOT and TOA. The test pulse functionality in Timepix 3 can be used to calibrate the chip.

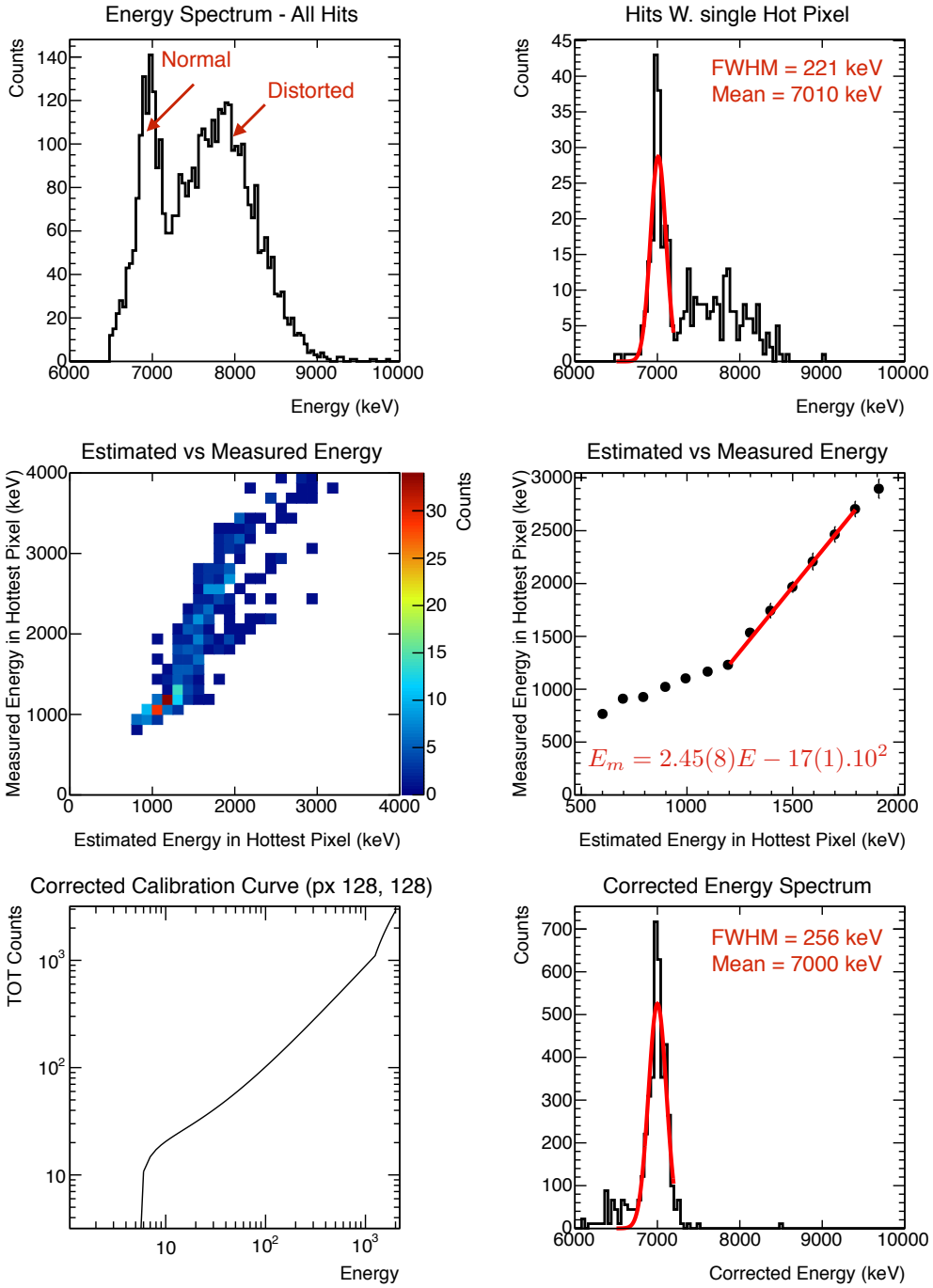

Figure 2.14: High charge correction/calibration of a Timepix detector with monoenergetic protons. (Top left) - whole energy spectrum, many events are clearly distorted, (top right) - spectrum of events with only one pixel with E >800 keV, (middle left) - heat map of approximate value in hot pixel against measured value, (middle right), derived energy correction curve (bottom left) new calibration curve and (bottom right) corrected spectrum.

- Dosepix [45] - Dosepix consists of 256 pixels which measure and bin TOT pulses using 16 discrete thresholds per pixel. It is designed to perform photon dose measurements in high flux environments.

- Timepix 2 - The Timepix 2 is a planned evolution of the Timepix. It retains the frame based read out of the Timepix 1, but acquires the simultaneous TOA/TOT modes, wider counters of the Timepix 3 and fixed test pulse functionality of the Timepix 3.

Chapter 3

Mixed Field Measurements and Cluster Formation with Timepix

Most of the material in the second half of this chapter was published as S.P.George, C.Severino et al, *Measurement of an accelerator based mixed field with a Timepix detector*. *JINST* **10** (2015), P03005, http://dx.doi.org/10.1088/1748-0221/10/03/P03005.

This chapter describes how the energy deposition by ionising radiation and the subsequent processes charge transport in the silicon sensor and signal shaping in the Timepix ASIC forms measurable signals in the Timepix detector. It then explains how to analyse these signals to get useful information about the traversing particle such as the polar angle and the Linear Energy Transfer (LET). An example of such an analysis and the useful information that can be gained is presented based on data taken at the CERF mixed field facility at CERN. Chapter 4 explains how this information can be processed to calculate quantities relevant to radiation dosimetry.

3.1 Clusters in the Timepix Detector

A single, interacting particle impinging on a pixelated sensor will deposit charge along the track of its interaction in the sensor, allowing the Timepix detector to act as a kind of digital nuclear emulsion [31]. The resultant signal is formed by the electronic transport of charge through the sensor to the pixel preamplifier pads.

We define a cluster as a group of contiguous reading pixels. Providing care is taken

to limit the acquisition time of the Timepix in order to avoid overlapping tracks, a cluster represents the track left by a single particle. The clusters left by several different impinging particles in a 300 µm thick silicon sensor in TOT mode are shown in figure 3.1.

The process of cluster formation can broadly be split into two processes that take place over very different timescales. The process of track formation (i.e. the traversal of the particle across the silicon sensor, and the creation of ionisation along its path) takes place over timescales that range from femto to pico seconds and the subsequent silicon diffusion and transport takes place over a (comparatively) much longer time, normally some tens of nanoseconds. As such these processes can be considered largely separate of each other and so we consider them separately. Firstly we discuss the processes that lead to the formation of signal from photons, electrons and charged particles in a Timepix detector, and then how charge transport modifies these signals into measured clusters.

3.2 Track Formation

3.2.1 Charged Particles

Charged particles deposit energy mostly by interactions with the electrons of the media they are slowing down in. These interactions create secondary or δ electrons, most of which are very short ranged and deposit their energy within one or two pixels of the track.

For charged particles in the range $\beta\gamma \approx 0.1$ to $\beta\gamma \approx 1000$ (5 MeV - 4 TeV for protons and 20 MeV - 15 TeV for alpha particles) the energy deposition in matter follows the Bethe formula.

$$\left\langle -\frac{dE}{dx} \right\rangle = Kz^2 \frac{Z}{A} \frac{1}{\beta^2} \left[\frac{1}{2} \ln \frac{2m_e c^2 \beta^2 \gamma^2 W_{\max}}{I^2} - \beta^2 - \frac{\delta(\beta\gamma)}{2} \right] \tag{3.1}$$

$$K = 4\pi N_a r_e^2 m_e c^2 \tag{3.2}$$

$$W_{\max} = \frac{2m_e c^2 \beta^2 \gamma^2}{1 + 2\gamma m_e/M + (m_e/M)^2} \tag{3.3}$$

where z and M are the charge and mass of the incoming particle, β and γ the

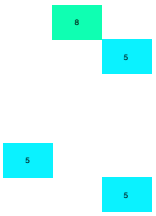

(a) Photoelectron hits from ^{55}Fe photons.

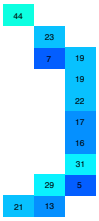

(b) Compton electron from ^{60}Co photon.

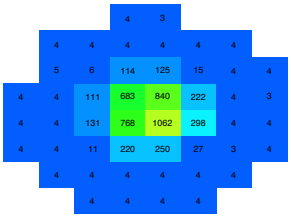

(c) Alpha particle from ^{241}Am decay (Bias at 30 V).

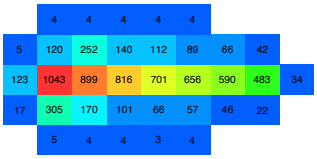

(d) 7 MeV proton incident at 75 degrees.

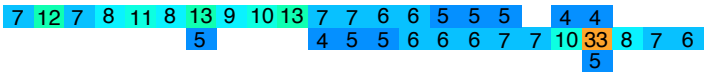

(e) High energy (≈ 200 MeV) proton produced by a therapeutic proton therapy beam.

Figure 3.1: Example Tracks Detected in a Timepix detector with a 300 µm thick sensor. Numbers show the calibrated energy in each pixel. Clusters (a), (c) and (d) stop in the sensor. Except where noted the sensor bias was set to 100 V (333 V cm^{-1}).

relativistic velocity and Lorentz factor of the particle, Z and A the atomic and mass number for the absorber, m_e the electron mass, r_e the electron radius, I the mean excitation energy (typically an experimental value) and $\delta(\beta\gamma)$ the density effect correction. $W_{\max}$ is the maximum energy produced in a single collision [46].

Integration of the Bethe formula yields the particle range (the so called Continuous Slowing Down Approximation range). Plots of the CDSA range for protons and alpha particles in silicon are shown in figure 3.2.

When charged particles stop in matter they deposit a large amount of energy in the last few millimetres of their track. This effect is called the 'Bragg Peak'. For charged particles of appropriate range (5 - 50 MeV for protons) incident at high angles relative to the sensor plane Bragg Peaks are clearly distinguishable in the Timepix detector. An example of the track left by such a particle (a 7 MeV proton incident at 75°) is shown in figure 3.1d).

High z particles also produce distinguishable δ electrons in a Timepix detector. In principle almost all of the slowing down of heavy charged particles is through the production of these delta rays, but in practice they are only energetic enough to be distinguished for particles with $z > 2$ (not alpha particles or protons). The energy spectrum of delta electrons with energies $T >> I$ is given by:

$$\frac{d^2N}{dTdx} = \frac{1}{2}Kz^2\frac{Z}{A}\frac{1}{\beta^2}\frac{(1-\beta^2T/W_{\max})}{T^2} \tag{3.4}$$

3.2.2 Electrons

Electrons behave like charged particles in so far as they slow down by interacting with the electrons of the media. As the particles have the same mass the momentum transfers involved in collisions can be large creating a distinctive tortuous paths in silicon. An example electron track is shown in figure 3.1b. Most energetic photon interactions produce electrons and there is no a priori way to distinguish an individual electron produced by a photon from one produced by a β decay[1].

The range of electrons in silicon is shown in figure 3.2. Slow electrons stop in 1 pixel, most energetic electrons produced by photon interactions (see the next section)

[1]However one can distinguish the nature of the field by covering a section of the sensor with a piece of material that will attenuate β rays.

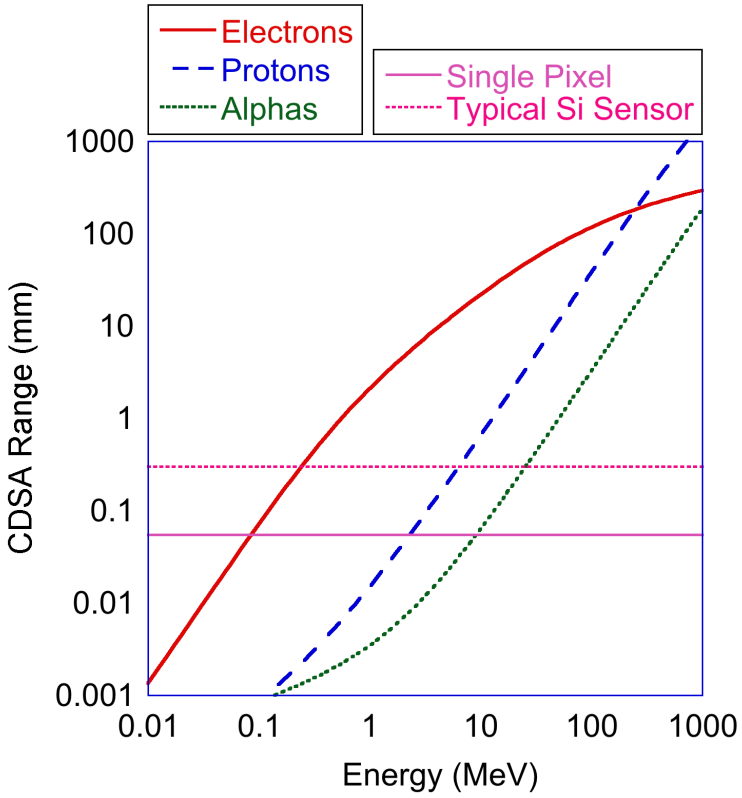

Figure 3.2: Ranges of electrons protons, alpha particles in silicon computed with the CDSA approximation [47]. For comparison the pitch of a single pixel and thickness of a typical silicon sensor attached to a Timepix are shown.

have similar stopping powers and ranges larger than the sensor thickness.

Fast electrons ($E >$10 MeV) lose their energy primarily by Bremsstrahlung, which produces a wide continuum of gamma rays [3]. These gamma rays will not form a connected track if indeed they do interact in the sensor (see the discussion in section 3.2.4 on fluorescence x-rays).

Positrons behave in a very similar way to electrons with the exception that they annihilate when they stop. This releases two 511 keV photons (which in a Timepix sensor will normally exit without interacting).

3.2.3 Photons

Photons are neutral particles, that is they are not directly detectable by their energy deposition. Instead photons are detected by the energy deposition of the secondary particles produced by the interactions of photons with matter. These secondary particles are normally electrons, although for sufficiently high energy photons they can be positrons ($E \gtrsim$1 MeV) or neutrons ($E \gtrsim$10 MeV). For typical applications of the Timepix detector, photoelectric and Compton interactions, both of which produce a secondary electron, are the most important.

The probability of a photon interaction occurring is defined through the attenuation coefficient μ.

$$\frac{I}{I_0} = e^{-\mu x} \tag{3.5}$$

where $\frac{I}{I_0}$ is the fraction of photons remaining after attenuation through an absorber of thickness x. Hence $1 - e^{-\mu x}$ is the interaction probability in a thickness x.

The absolute attenuation coefficients in silicon and absolute interaction probabilities in 300 µm of silicon for these interactions are shown in figure 3.3 as a function of incident photon energy. In general the interaction probability p is unity for photons less than 10 keV and is then a sharply decreasing function of energy until $\approx$ 1 MeV when it flattens out at approximately $p = 10^{-3}$.

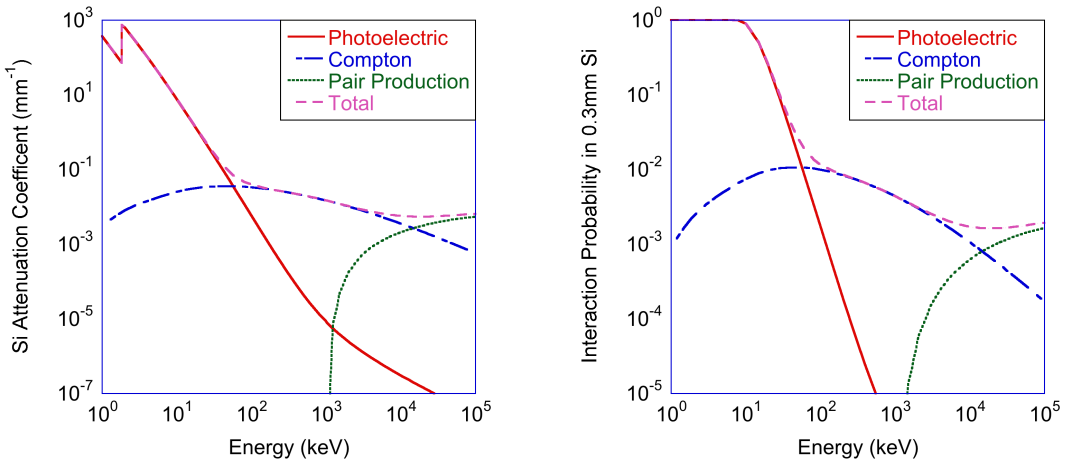

Figure 3.3: Photoelectric, Compton and Pair Production attenuation coefficients in silicon and absolute interaction probabilities in a typical (300 µm) Timepix detector silicon sensor as a function of photon energy. The interaction probability becomes a sharply decreasing function of energy above 10 keV and the Compton interaction becomes dominant above 100 keV.

3.2.4 Photons - The Photoelectric Interaction

The photoelectric interaction dominates the interactions of photons in silicon below 100 keV. During a photoelectric absorption a photon of energy $h\nu$ completely transfers its energy to an electron. For gamma rays this electron is normally in the most tightly bound (or K) electronic shell. The electron is then emitted from the atom with an energy E_e equal to the gamma ray minus the binding energy E_b of the electron, i.e:

$$E_e = h\nu - E_b \tag{3.6}$$

In silicon the K shell binding energy is 1.839 keV. The resulting vacancy in silicon can then filled either through Auger electron emission or by a less tightly bound electron transitioning into the K shell resulting in the fluorescence emission of a second x ray with a maximum energy of 1.839 keV (if capturing a free electron). In silicon Auger emission is the dominant process normally resulting in the capture of the electron in the same pixel as the photoelectron. As the energy of produced photo and Auger electrons is typically very small these electrons stop within a single pixel.

In other materials such as Cadmium Telluride the emission of a fluorescence photon is the dominant process resulting in distinctive fluorescence peaks. This effect is different to that encountered in monolithic detectors where instead one encounters an *escape peak* at $h\nu - E_b$ when the fluorescence photon exits the detector without interacting. In a monolithic detector the fluorescence and photoelectric events are essentially coincident in time with each other, and so cannot be distinguished, while in a pixellated detector, both particles are distinguishable as separated clusters.

3.2.5 Photons - The Compton Interaction

Between energies of approximately 100 keV and 10 MeV Compton scattering becomes the dominant energy deposition process for photons in silicon. Compton scattering is an inelastic process where a photon transfers some fraction of its energy to an electron and scatters through some angle κ.

$$h\nu' = \frac{h\nu}{1 + \frac{h\nu}{m_e c^2}(1 - \cos\kappa)} \tag{3.7}$$

Where $m_e c^2$ is the rest mass of the electron. The spectrum of electrons produced by Compton interactions is broad with a maximum energy at $\kappa = 180°$, a feature called the Compton Edge[2].

Electrons produced by Compton scattering tend to have a range of at least several pixels in a typical (300 µm) silicon sensor used with a Timeix and in most cases will end up exiting through the top or bottom of the sensor before depositing their full energy. In addition the absolute cross section in 300 µm of silicon for photons in the energy range where Compton scattering is dominant is quite low. For these reasons the spectroscopic performance of a Timepix detector for photons much above 100 keV is very poor and normal spectral features such as a Compton Edge are absent[3].

[2]The full double differential cross section for Compton scattering is described by the Klein-Nishina formula [48].

[3]One can find thicker sensors made of higher Z semiconductors such as CdTe, CdZnTe and GaAs which should work much better for high energy gamma rays than Si, but these tend to be of somewhat variable quality - this field is rapidly evolving, and it is not unreasonably to expect high quality pixel sensors for spectroscopic gamma ray measurements to be on the market in the next few years.

3.2.6 Photons - Pair Production

Pair production involves the creation of an electron and a positron, a process that requires at a minimum 1.022 MeV of energy. Pair production typically becomes the dominant process in silicon above about 10 MeV. Any excess energy is transferred into the electron and positron.

3.2.7 Charge Transport and ASIC Effects on Cluster Formation

A more detailed discussion of carrier transport in semiconductors is carried out in section 2.2.2, the key result with relevance to this section is that created charge diffuses as a gaussian with a width of

$$\sigma = \sqrt{2\frac{kT}{e}\frac{d^2}{V_b}} \tag{3.8}$$

where d is the sensor thickness and V_b the bias voltage. For a 300 µm thick silicon sensor at 100 V the diffusion full width half maximum is 19 µm.

For photons and light particles such as electrons this can result in the sharing of charge between adjacent pixels. In this case the spectral response can be non-linear and an energy calibration (section 2.4.5) is needed to correct it.

In addition to conventional diffusion there are several additional effects specific to charged particles with high stopping power in silicon ($\gtrsim 10\,\mathrm{keV\,\mu m^{-1}}$). They are the following:

- The Timepix detector pixel exhibits over response above about 850 keV per pixel. This is caused by a defect in the pixel front end and be corrected with a compensated calibration curve (see section 2.4.5).

- Heavy charged particles also induce a signal proportional to their total charge in neighbouring pixels. This is caused by induction from drifting charge. The drifting charge induces equal and opposite mirror charges in the preamplifier, but the shaper circuitry only operates on the positive part of pulse (or negative part if the ASIC is run in electron collection mode) giving a net output. The result of

this process is formation of a halo or 'skirt' around the cluster with a fairly low energy deposition which is nevertheless proportional to the total cluster charge.

- Heavy charged particles (including alpha particles) exhibit substantially wider tracks than can be explained by simple diffusion alone, it is assumed that there is an additional process, most likely some kind of plasma effect whereby the locally deposited charge shields the bias electric field allowing the additional lateral spread [49, 50].

- The volcano effect is seen with particles that deposit a lot of charge over short lengths (for example lead ions), often, but not always at low angles of incidence and causes a characteristic 'crater' void or nearly void of collected charge in the center of a cluster such that the whole cluster structure resembles a volcano. It can be corrected using the energy deposition in the skirt [40] . It is currently (July 2015) unknown if the volcano effect is caused by some effect in the sensor, the readout or a combination of the two.

3.3 Data Analysis and Tools

The Timepix detector is relatively data intensive. The binary x, y, c file format in Pixelman is generally the most data efficient for clusterable data. In this format the x and y pixel positions are stored as a 16 bit short and the counts as a 32 bit int for a total of 8 bytes per pixel hit. If a sample frame contains 2000 hit pixels (which is very approximately the maximum occupancy beyond which tracks begin to overlap) then the data output at 80 Frames per Second (the maximum rate of a FITPix) is approximately $10\,\mathrm{Mbit\,s^{-1}}$ or $\approx 4.6\,\mathrm{GB\,h^{-1}}$. While small in comparison to the data sets gathered by particle physics experiments it is clear that some form of preprocessing is needed if one wishes to explore the data and generate plots in an interactive way[4]. The task is to then take the individual particle tracks left in the Timepix detector, reduce them to some set of relevant (ideally physically relevant) parameters such as track length and deposited energy and then analyse these parameters.

All of the analysis discussed in this thesis is carried out using ROOT and MAFalda.

[4]In the future the analysis problem will only get worse. The Timepix3 which is not the subject of this thesis, but is now available for use, outputs data at a rate of approximately 85 million hits per second, or $2.5\,\mathrm{Gbit/cm^2 s}$, a 500 fold improvement over its predecessor. In the corresponding time period desktop computing performance has improved at most 5 fold.

3.3.1 ROOT

ROOT [51] is a powerful data analysis toolkit developed at CERN which is ubiquitously used for analysis in current high energy physics experiments. ROOT provides a file format that allows the serialisation (i.e. the reading and writing) of arbitrary C++ objects which typically represent a complicated measured physics event, a plotting and drawing package; a large toolkit including fitting and minimisation packages and a C++ command line interpreter which allows the interactive use of ROOT classes at some (roughly 10 fold) cost to performance. Interpreted ROOT C++ code can be compiled to run in batch mode at native C++ performance levels and compiled and interpreted code can be mixed together.

3.3.2 MAFalda

MAFalda [52] (Medipix Analysis Framework) is a C++/ROOT based framework for the analysis of the data gathered by the Timepix and other hybrid pixel detectors. MAFalda essentially consists of three components:

- A convenient ROOT based file format for storing and accessing the data gathered by the Timepix, and a program for conversion of the Pixelman output files.
- A toolset for common operations carried out on clusters.
- An analysis chain based on the ATLAS Athena framework [53].

The analysis chain loads a series of user implemented algorithms which operate once per frame. These are implemented as a C++ class which inherits from a superclass which provides a common interface to the Medipix data. For example one algorithm may perform a clustering operation, the second perform morphological analysis on these clusters and the third perform a more computationally intensive analysis on an 'interesting' set of clusters. A transient data store called the *storegate* is provided as a mechanism for cross-algorithm communication and a special viewer algorithm is provided in order to display the frame data. Each algorithm can output its own n-Tuple for further analysis and interactively communicate with the viewer in order to display markers, arrows etc if desired. The analysis chain can be built very easily in an interactive top level ROOT macro while all of the data analysis code is compiled, providing the user with the speed inherent to C++ but with the flexibility to

change simple analysis options without recompilation. An example top level MAFalda algorithm and the viewer interface is shown in figure 3.4.

Once the initial analysis has been run (which may take some time depending on the dataset size) the resulting n-Tuples produced by the algorithms can be analysed. As these are typically orders of magnitude smaller than the raw output data of the Timepix this allows for the real time plotting and interactive exploration of the data.

3.4 Calculation of Track Parameters

This section describes the process of analysing the tracks left in a Timepix detector to produce useful data.

3.4.1 Basic Parameters - length, density, deposited energy

If the radiation field incident on a Timepix detector is roughly spatially homogenous the data can be searched for noisy pixels. This is done by searching through single pixel hits for pixels with more than $10\sigma + 1$ total hits from the mean number of single pixel hits. In a Poissonian process such as photon counting $\sigma = \sqrt{\lambda}$ where λ is the average number of hits per pixel and the factor $+1$ is included to account for average pixel occupancies substantially less than 1.

The data is then sorted into clusters of hits. This is done with a simple 8-fold search algorithm. The algorithm starts by looking for cells that have received hits. When it finds one it creates a new cluster. It then recursively[5] searches the 8 cells surrounding that cluster and if they have received hits they are added to the cluster. After clustering several basic properties of the cluster are calculated. These are the X and Y dimensions of the cluster, the length and the width of the cluster, the centroid and the centre of mass centroid (weighted by TOT/energy), the energy deposition in the cluster, the density of the cluster and the number of inner pixels (pixels with more than 4 neighbours).

The length and width of the cluster are found using the rotating callipers algorithm [54] and define a minimum bounding box for the cluster. We define the length as the longer of the two axes of the bounding box. The X and Y dimensions on the other

[5]Using simple recursion for this procedure is not recommended as the recursion level can be very deep for large clusters leading to very poor performance.

```
void doProtonClustering()
{
    // Load the MediPix analysis lib
    gSystem->Load("libMediPixAnalysisCore.so");

    // Get an instance of the analysis manager and load data
    AnalysisManager mpxAnalysis("/Users/stuart/Documents/Software/mafalda/mpxdataconverter/MPXNtuple_Biotite_Test.root");

    // Blobs Finder.  This is a Clustering Algorithm
    BlobsFinder * bf = new BlobsFinder;
    mpxAnalysis.ConnectAlgo("BlobsFinder", bf);
    bf->changeOutputLevel(MSG::INFO);
    bf->SetBorderExclusion(1);
    bf->SetDiscontinuityTolerance(0);

    // Your algorithm --> ProtonClustering
    ProtonClustering * ac = new ProtonClustering(10, 0, 10 );
    mpxAnalysis.ConnectAlgo("ProtonClustering", ac);

    // Setting up the calibration from this algorithm by loading
    //  the 4 calibration files and the clock used for calibration.
    //  If you fail loading any of the 5 following pieces then the
    //  calibration won't be available but you can still run the job.
    ac->SetCalibrationConfigFile_a("/Users/stuart/Dropbox/Medipix Configs/B05-W0257/_Calib_a.txt");
    ac->SetCalibrationConfigFile_b("/Users/stuart/Dropbox/Medipix Configs/B05-W0257/_Calib_b.txt");
    ac->SetCalibrationConfigFile_c("/Users/stuart/Dropbox/Medipix Configs/B05-W0257/_Calib_c.txt");
    ac->SetCalibrationConfigFile_t("/Users/stuart/Dropbox/Medipix Configs/B05-W0257/_Calib_t.txt");
    ac->SetCalibClk(9.6); // MHz
    ac->ReadConfiguration();
    //ac->OutputLevel(MSG::DEBUG);

    // This is an special algorithm that works as a frames viewer
    MPXViewer * v1 = new MPXViewer;
    v1->changeOutputLevel(MSG::DEBUG);
    mpxAnalysis.ConnectAlgo("MPXViewer", v1);
    v1->SetFrameTitle("Offline Analysis");
    // Run !
    mpxAnalysis.Run();         // all frames
}
```

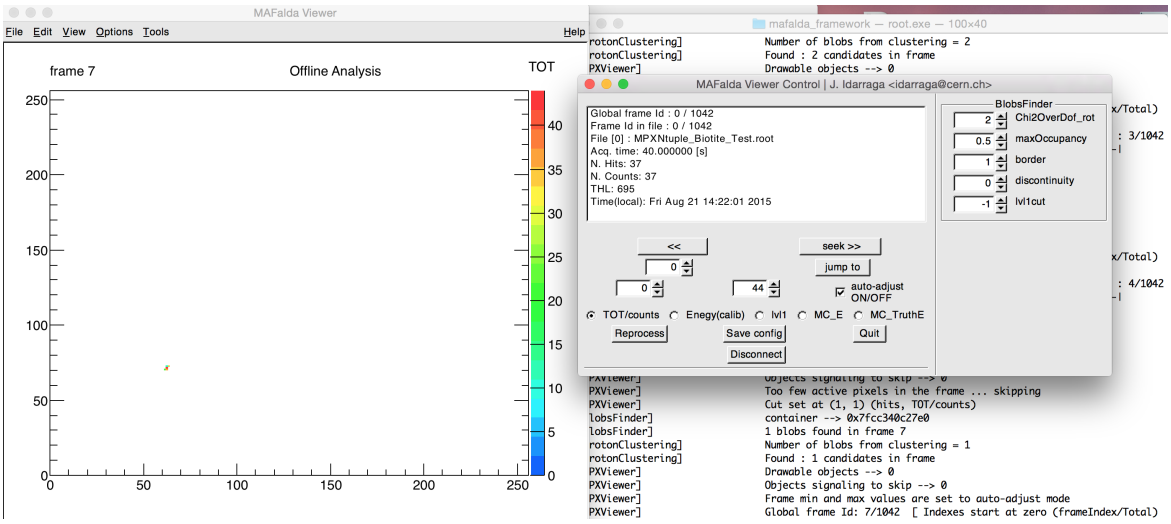

Figure 3.4: Example MAFalda top level macro for steering an analysis job (top) and MAFalda viewer and console (bottom).

hand refer to the size in pixels along the X and Y axes on the chip. A diagram showing both quantities is shown in figure 3.5. The centroid and centre of mass weighted (with TOT or energy if calibrated) centroids are defined for a cluster with n members and weighting factor w_i as follows:

$$X_C = \sum_{i=0}^{i=n} = \frac{x_i}{n} \qquad Y_C = \sum_{i=0}^{i=n} = \frac{y_i}{n} \tag{3.9}$$

$$X_{WC} = \sum_{i=0}^{i=n} = w_i \frac{x_i}{n} \qquad Y_{WC} = \sum_{i=0}^{i=n} = w_i \frac{y_i}{n}. \tag{3.10}$$

The cluster density is defined as the number of occupied pixels divided by the cluster bounding box size, i.e.

$$\rho = \frac{n}{\text{Length} \times \text{Width}}. \tag{3.11}$$

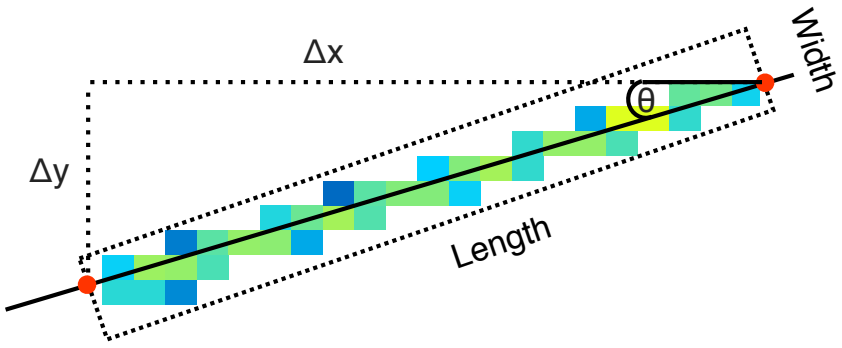

Figure 3.5: Minimum bounding box surrounding an example cluster with least squares fit. By finding the intersection points of the fit with the box, the projected track length L_p and angle can be determined (equations 3.12 and 3.13).

3.4.2 Basic Cluster Types

The clusters can then be sorted into basic geometric types based on the quantities calculated in the previous sections for further analysis. This analysis follows the methods outlined by the Institute for Advanced Experimental Physics at the Czech Technical

Type	Inner Pixels	Length/ Width Ratio	Other Criteria	Example Tracks
Small Blob	0	-	1 or 2 Pixels, 3 if L shape, 4 is square	
Heavy Track	> 4	> 1.25	Not S.Blob Density > 0.3	
Heavy Blob	> 4	< 1.25	Not H.Track Density > 0.5	
Medium Blob	> 1	< 1.25	Not H.Blob Density > 0.5	
Straight Track	0	> 8	Not M.Blob Minor axis < 3 pixels	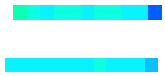
Light Track	-	-	Not S.Track	

Table 3.1: Clustering algorithm developed for use at CERF, read down using an if, else if format.

Institute in Prague [55]. The principle is that morphology of the cluster is representative of the physics of the particle that created it and from this some information about the particle can be elucidated. This procedure is very successful for simple fields such as alpha/x-ray [56]. The applicability to this procedure to mixed radiation fields is discussed in section 3.5.2. The cluster sorting algorithm used is shown in table 3.1. Common origins of these cluster types, based on the physics described earlier are listed in table 3.2.

3.4.3 Real parameters - Absorbed Dose, Track Length and Polar Angles, LET

The absorbed dose from a cluster is defined as the deposited energy E divided by the mass of the active area of the sensor assuming that the radiation in question is not significantly attenuated or stops in the sensor [58]. In general this is true for most gamma ray and energetic charged particle fields, but notably is not true in a 300 µm silicon sensor for most alpha sources (which stop in the first few micrometers of the

Cluster Type	Possible Origin
Small Blob	Low energy short range particle/interaction, i.e. x-ray photoelectron or neutron elastic scattering [57]. Number of pixel hits determined by position of interaction in pixel (see section 2.4.3).
Heavy Track	High energy ($\gtrsim 20\,\mathrm{MeV}$), heavy ($Z \geqslant 1$) charged particle e.g, proton $> 20\,\mathrm{MeV}$ or alpha $> 100\,\mathrm{MeV}$.
Heavy Blob	High energy ($\gtrsim 2\,\mathrm{MeV}$), short range (few µm in Si) particle.
Medium Blob	Fast charged particle at high angle of incidence, very slow charged particle ($\lesssim 2\,\mathrm{MeV}$) or fast neutron interaction (see section 3.5.3 or [57]).
Straight Track	Light minimum ionizing particle (muon, fast proton, pion etc).
Light Track	Multiple scatterer (electron, positron $\gtrsim 100\,\mathrm{keV}$).

Table 3.2: Description of common origins of different cluster types

sensor) and protons below about 10 MeV. For the rest of this chapter it is assumed (unless otherwise noted) that tracks penetrate the sensor. In that case we can define the following quantities.

The projected track length L_p is the measured length of the track. For tracks with minimal charge sharing we compute this by fitting the track with linear least squares (normally weighted by energy deposition per pixel) and then finding the intersection points of the least squares fit with the bounding box, an example of the bounding box with a least squares fit is shown in figure 3.5. For tracks with large amounts of charge sharing we use the procedure defined by Hoang which is described below. From the least squares fit the polar angle in the plane of the pixel matrix (the Azimuth) can be defined through simple geometry,

$$\theta = \arctan\left(\frac{\Delta Y}{\Delta X}\right) \tag{3.12}$$

$$L_p = \sqrt{\Delta X^2 + \Delta Y^2}. \tag{3.13}$$

From the projected track length the altitude polar angle θ and real track length L can be determined for a sensor of thickness T as shown in figure 3.6,

$$\phi = \arctan\left(\frac{T}{L_p}\right) \tag{3.14}$$

$$L = \sqrt{L_p^2 + T^2}. \tag{3.15}$$

The Linear Energy Transfer or LET is an important quantity for dosimetry and is used to calculate dose rates in the next chapter. Formally, the LET is defined as the energy deposition per unit length over some site size [59], which is normally selected to match a biologically important volume such as a cell, or cell nucleus. This formalism is used in order that energetic delta electrons which may transport a substantial quantity of energy away from a localised site are not included in the 'local' energy deposition.

It follows that the LET in a Timepix silicon sensor is something of a nebulous concept, as the pixels themselves are asymmetric, being substantially taller (300 µm or 500 µm) than they are wide (55 µm) and the signal spread by charge sharing obscures short range delta electrons. In addition, in the analysis procedure one has the choice of removing or retaining visible delta electrons as part of the energy deposition. Because the sensor is still 'thin' in comparison to the range of particularly energetic delta electrons (350 keV for a 300 µm thick sensor and 500 keV for a 500 µm) it is clear that the LET measured is not simply the stopping power dE/dX either, but instead some quantity between the two depending on the inherent track structure of the primary particle. For simplicity of discussion we refer to the measured quantity as the $\mathrm{LET_{Si}}$ following [60], however understanding the size of the errors introduced by this technique for different particle fields is an open question that should be studied in the future. We define the $\mathrm{LET_{Si}}$ as,

$$\mathrm{LET_{Si}} = \frac{E}{L}. \tag{3.16}$$

3.4.4 Heavy Ion Tracks

For tracks with significant charge sharing a modification to the above method of determining track length is used following the method of Hoang [61]. In this case the track displays a large skirt due to the induction effect discussed in section 3.2.7 as

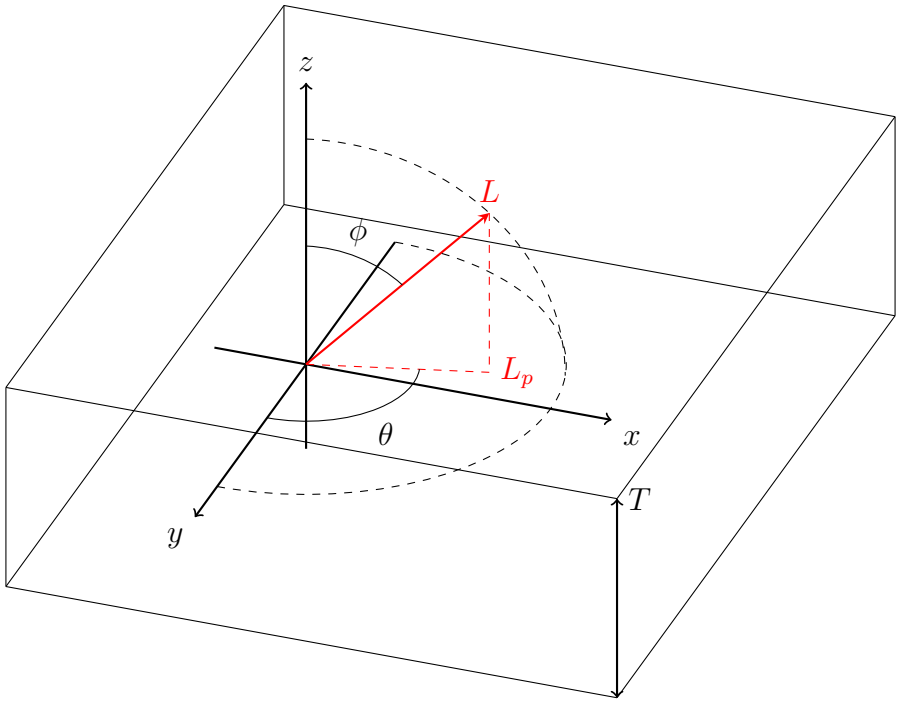

Figure 3.6: Measurement of the azimuth angle θ and altitude ϕ relative to the sensor axes from a penetrating track of length L over a sensor of thickness T.

well as pronounced charge sharing. The track can also contain distinguishable delta electrons which may extend far beyond the primary track. All of these effects need to be corrected in calculating the real length.

The skirt region is isolated and removed by setting a minimum threshold (normally 1% of the charge of the hottest pixel in the cluster) and counting any pixels below that threshold as part of the skirt. Delta electrons are removed iteratively by removing pixels with 1 or 2 neighbours until none remain. The bounding box of the remaining core region is then calculated and an empirical formula (equation 3.17 and 3.18 below) using the major (M) and minor (m) axes of the box used to calculate the ϕ angle of the track. The θ angle is calculated using a least squares fit to the core. The major components of a heavy ion cluster are shown in figure 3.7.

$$\phi = \arctan\left[\frac{55}{T}\left(M - \frac{m - 1.5}{M + 1}.m\right)\right] \tag{3.17}$$

$$L = T\cos(\phi) \tag{3.18}$$

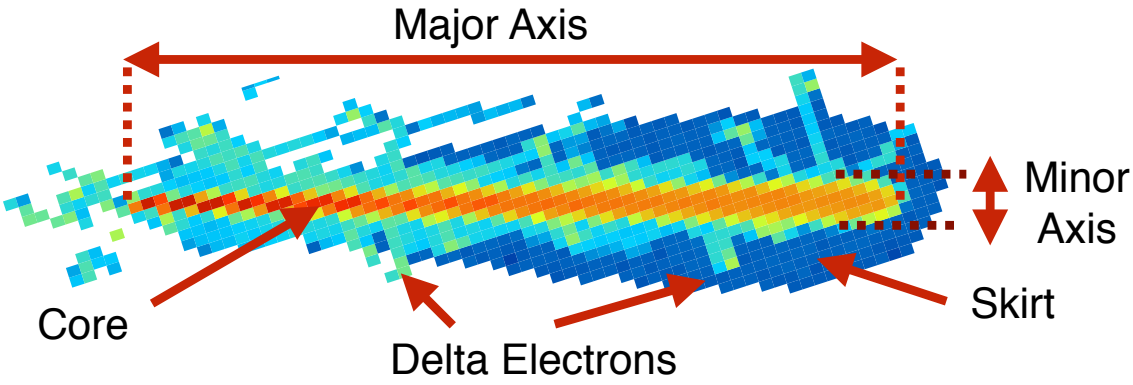

Figure 3.7: Major components of a heavy ion cluster showing the skirt, delta electrons, core and major/minor axes. The color scale is logarithmic, dark blue ≈ 10 keV/pixel, green ≈ 100 keV, orange ≈ 1 MeV (color scale the same as figure 3.8). The length of this cluster can be computed using equation 3.18.

Four example tracks (from the ISS Timepix detector deployment, see chaper 4) with their calculated LET, altitude and azumith angles are shown in figure 3.8.

3.5 Data taken in a mixed field at CERF

This section describes the analysis of the data taken with Timepix detector in a mixed field at the CERF facility at CERN.

3.5.1 The CERF Facility

CERF [62] is a reference radiation facility installed in one of the secondary beam lines from the Super Proton Synchrotron (SPS), in the North Experimental Area of the Prevessin (French) site at CERN. CERF produces a field similar to that produced by the interactions of cosmic rays with the atmosphere at commercial flight altitudes. The stray radiation field is created by colliding a beam of $\frac{1}{3}$ protons and $\frac{2}{3}$ positive pions at 120 GeV/c with a 50 cm long copper target, which is equivalent to three interaction lengths for the impinging beam. The intensity of the beam is measured with an Ionization Chamber (IC) [63]. CERF produces a field consisting mostly of protons, electrons, photons, neutrons and muons (plus some pions and kaons) with a wide range of energies, which makes it interesting for the evaluation of detector performance in mixed fields.

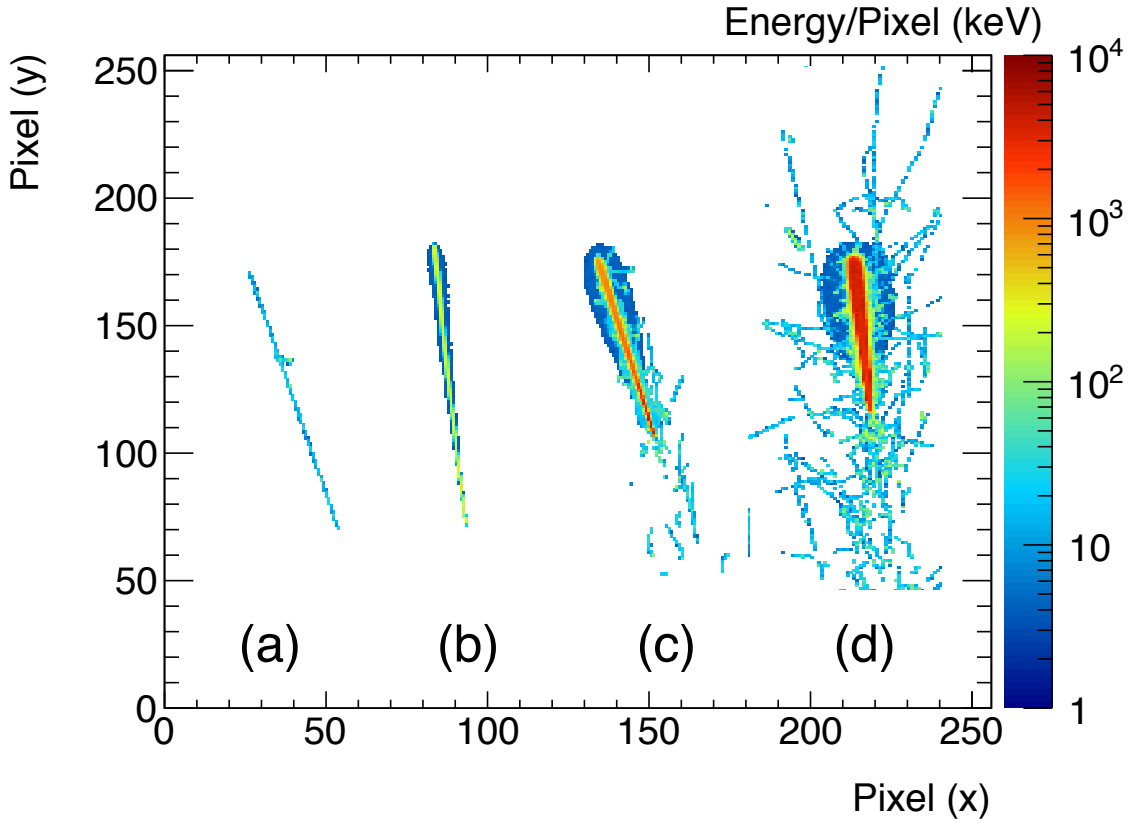

Figure 3.8: Four tracks of increasing $\mathrm{LET_{Si}}$:

(a)	$\mathrm{LET_{Si}} = 0.52\,\mathrm{keV\,\mu m^{-1}}$	$\theta = 71.0°$	$\phi = 84.6°$
(b)	$\mathrm{LET_{Si}} = 5.45\,\mathrm{keV\,\mu m^{-1}}$	$\theta = 82.0°$	$\phi = 84.0°$
(c)	$\mathrm{LET_{Si}} = 54.8\,\mathrm{keV\,\mu m^{-1}}$	$\theta = 66.7°$	$\phi = 81.4°$
(d)	$\mathrm{LET_{Si}} = 233\,\mathrm{keV\,\mu m^{-1}}$	$\theta = 84.2°$	$\phi = 81.1°$

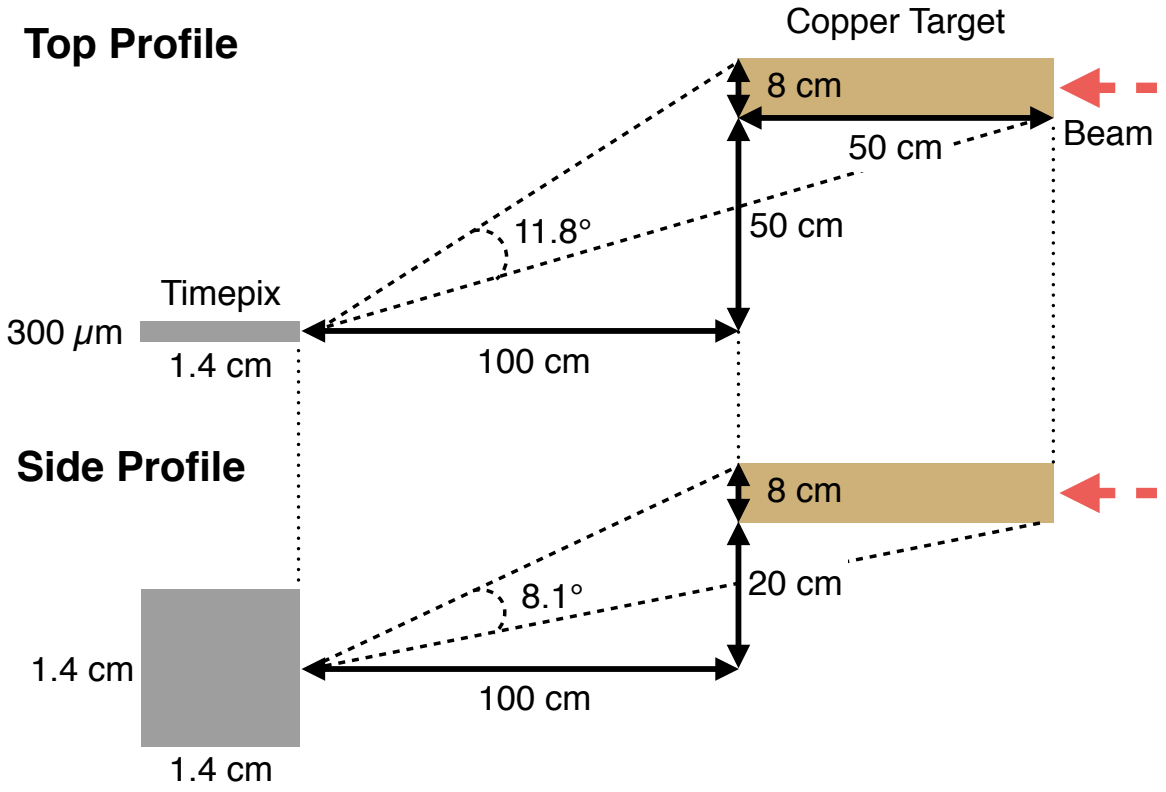

Figure 3.9: Top down and side views of the setup geometry, including opening angular widths onto the Timepix detector from top and side of the copper target.

The Timepix detector was placed in a reference irradiation position 100 cm downstream of the copper target, shifted 50 cm horizontally and 20 cm vertically. The Timepix detector was placed at a 90° angle of incidence (i.e. side on) with respect to the target, a diagram of the experimental setup is shown in figure 3.9. This is important because it allows a first broad separation of particle types based on track angle, particles coming from the target should leave tracks at an approximate angle of $\phi = 70°$ and $\theta = 15°$ (see fig 3.6 for an explanation of angles). Figure 3.9 also show the expected angular widths of these distributions from geometrical considerations, they are $\Delta\theta = 8.1°$ and $\Delta\phi = 11.8°$.

The measured clusters are then sorted into the basic geometric types using the algorithm described in section 3.4.2. In section 3.5.2 we analyse how it compares against the LET based measurements that are necessary for mixed field dosimetry and used to compute dose rates in the next chapter.

Particles not coming from the target leave tracks going in other directions. Our

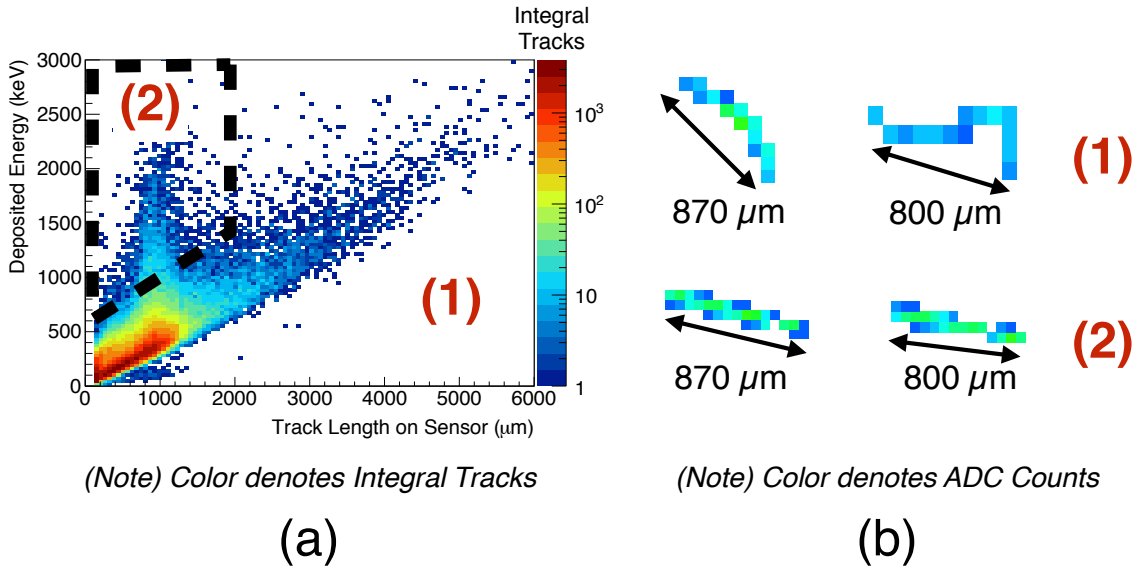

Figure 3.10: Measured light track properties, (a) Track length distribution on sensor versus the deposited energy. Two different energy deposition branches are visible, likely due to electrons (1) and energetic protons (2). Sample tracks from (1) and (2) are shown in (b).

clustering algorithm discriminates medium and heavy 'Blobs' as clusters which are highly circular. These clusters are produced by particles moving at a near vertical ϕ angle through the chip or by slow particles moving at other angles which stop in the first few microns of silicon. From the geometry of our setup, we expect anything emitted from the target to project a track in silicon several pixels long. To first order blobs are therefore restricted to slow particles.

3.5.2 Tracking measurements and LET distributions

For radiation protection purposes an important quantity to calculate is the LET, we calculate this following the method outlined in section 3.4.3.

Figure 3.10 shows a heat map of cluster length and deposited energy for light track clusters. Within the light track cluster category there appear to be two distinct branches of clusters with different $\mathrm{LET_{Si}}$ values. The tracks in groups (1) have a range of several pixels and follow curved paths with many changes of direction in the sensor. The tracks in group (2) are straighter and more ionizing than those in group (1) as illustrated by the sample clusters shown in figure 3.10(b).

We computed $\mathrm{LET_{Si}}$ distributions for light (high and low energy deposition branches),

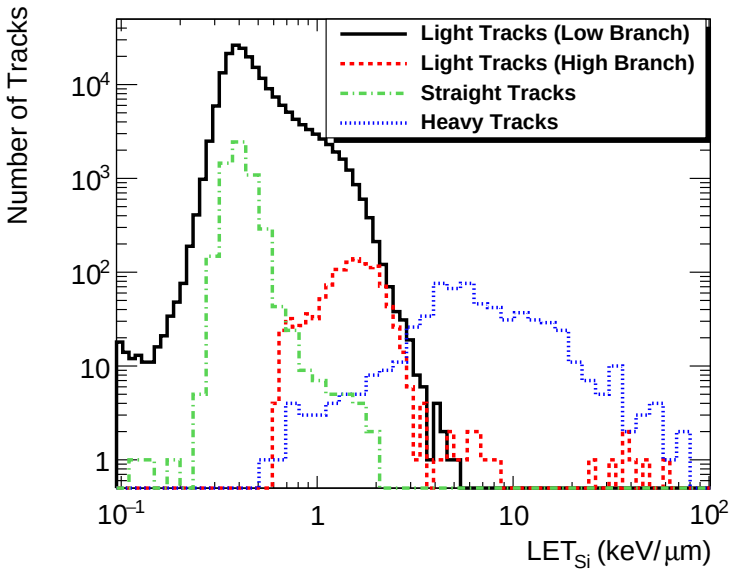

Figure 3.11: LET_{Si} distributions for light (high and low energy deposition branches, regions (1) and (2) from Figure 3.10), heavy and straight tracks (as defined in Table 3.1).

heavy and straight tracks (the different morphological categories defined in table 3.1). These LET_{Si} distributions are shown in Figure 3.11. The LET_{Si} distributions overlap, showing how broadly our morphological clustering algorithm separates clusters by LET_{Si}. Interestingly the LET_{Si} distribution of the straight track category fits entirely within the LET_{Si} of the light track category. This implies that these track categories would not be separable on the basis of LET_{Si} characterisation alone.

We also computed the ϕ and θ angles for track like particles. Heat maps of these distributions are shown in Figure 3.12. Both branches of the light tracks and heavy tracks have an extended distribution centred around $\phi = 75°$ and $\theta = -10°$. The absolute limits of this bounding box from the geometrical constraints shown in Figure 3.9 are also shown in the top left of Figure 3.12 overlaid on the light track distribution, which fits inside this box. Straight tracks are offset from this distribution by approximately 5 degrees in theta and phi, which lies outside the bounded region from the target geometry. The distribution of straight tracks is also much more point like than for other tracks. This suggests a single separate source for these tracks, one explanation for which is energetic muons. These are produced by pion decay and primary beam interactions with the collimators in the beam line (which is several hundred metres long) upstream of the CERF copper target.

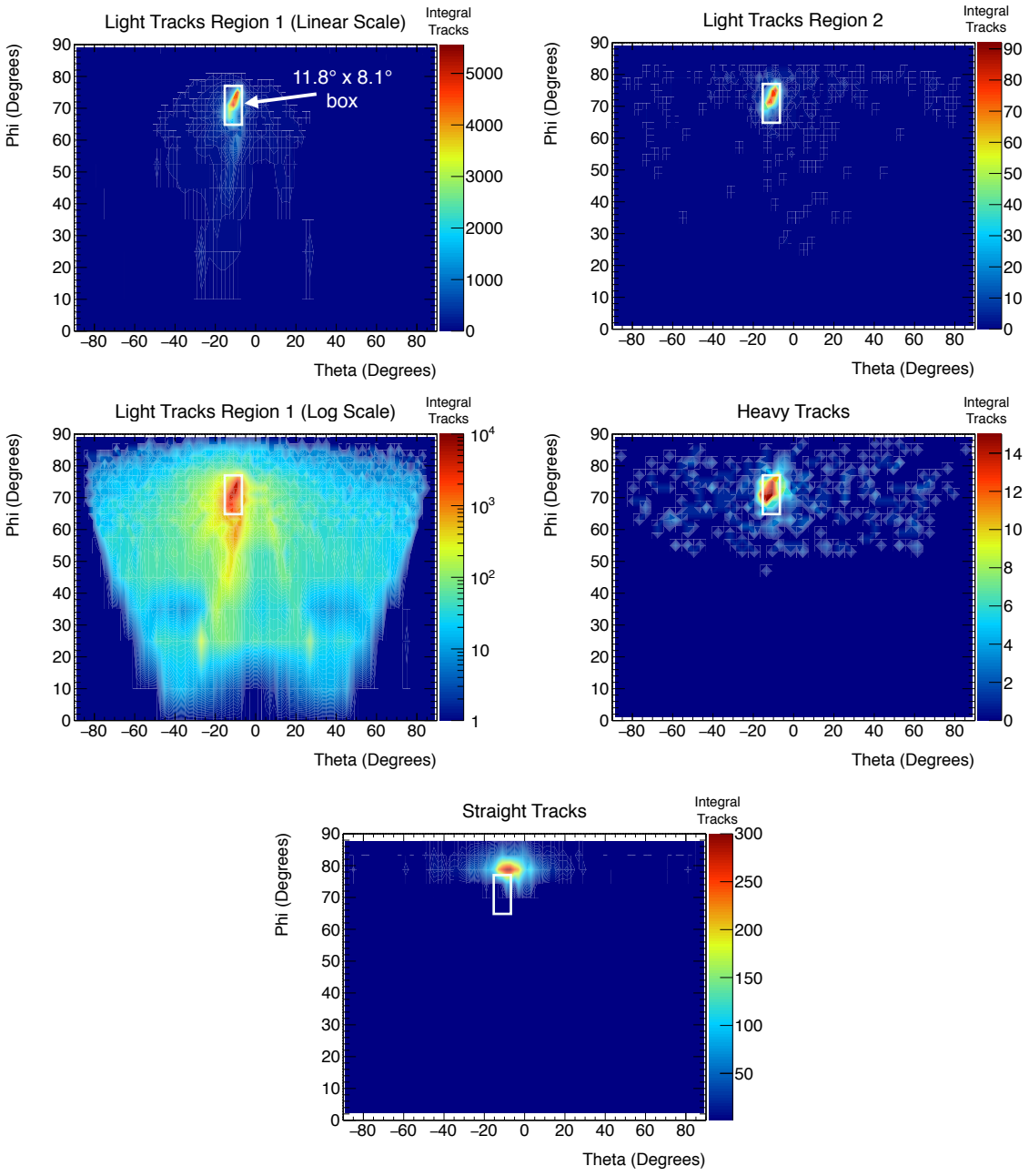

Figure 3.12: Heat maps of altitude and azimuthal angles of tracks. Both light tracks and heavy tracks have an extended distribution centred around $\phi = 70°$ and $\theta = -10°$, with a width corresponding to the geometrical width of the target (Figure 3.9). Straight tracks originate outside of this distribution and probably are muons from primary beam pion decay and interactions with collimators upstream of the target.

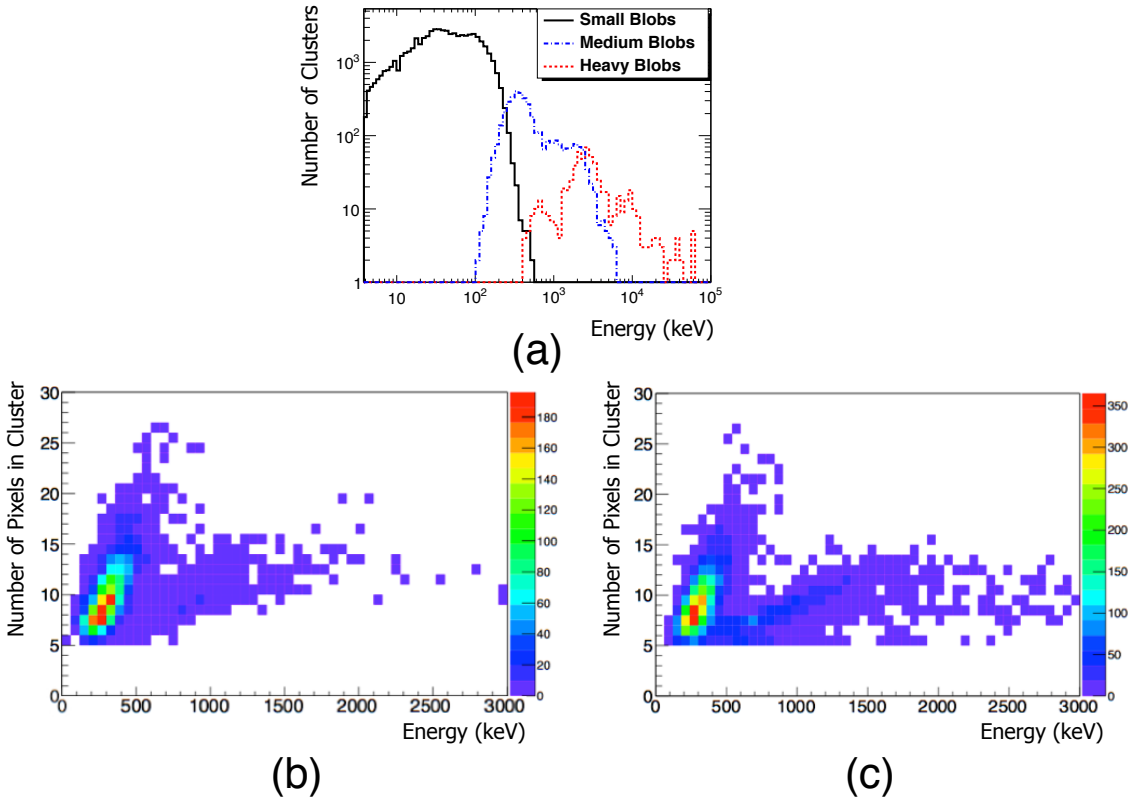

Figure 3.13: Blob energy spectrum at CERF (a), medium blob energy/pixel distribution at CERF (b) and for comparison at the CERN calibration laboratory (c). These blobs are interesting because they deposit a large amount of energy ($\approx 1.5\,\mathrm{MeV}$) in a comparatively small number of pixels (5-10).

3.5.3 Blobs

As discussed in section 3.5.1, due to the geometric constraints of our setup, blob-like clusters could only correspond to either slow particles coming from the target, or fast particles coming from somewhere else, at a high angle of incidence. As we have excluded to first order fast incident particles from this category we can compute the spectrum of deposited energy, but not the $\mathrm{LET_{Si}}$. This is shown for small, medium and heavy blobs in Figure 3.13. As with the $\mathrm{LET_{Si}}$ distributions for tracks these spectra for blobs are broad and overlap.

We also note that there is a qualitative similarity between the so called medium blob population, shown in Figure 3.13(b), and the spectrum of (n,Si) background events measured with an AmBe source in the Calibration Laboratory at CERN shown in Figure 3.13(c). These medium blobs are interesting because they contain some

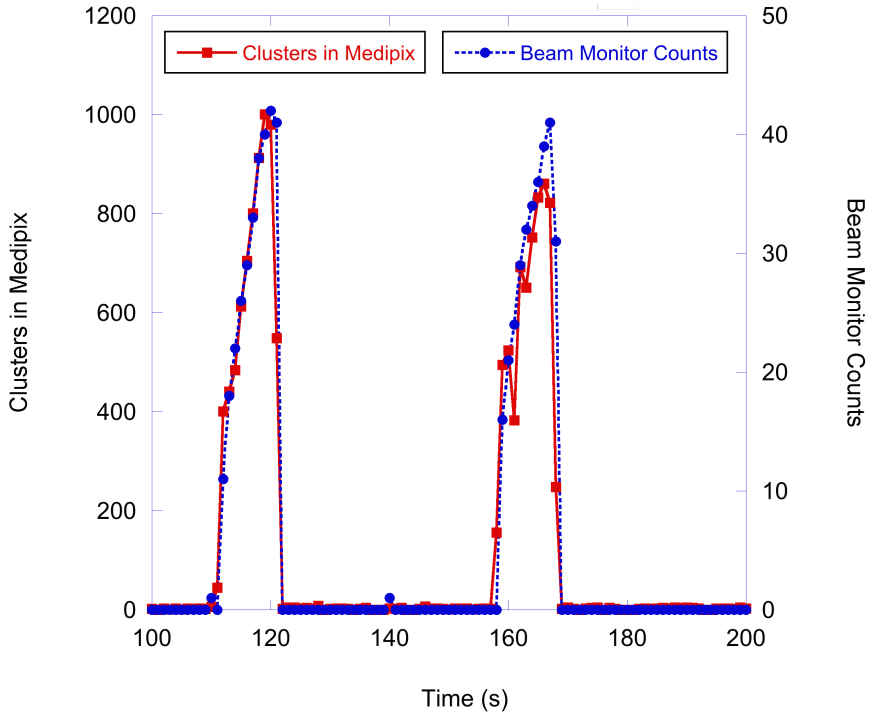

Figure 3.14: Number of measured clusters and beam monitor (IC) counts as a function of time.

events which deposit a relatively large amount of energy in only a few pixels, which one would expect to be spread over more pixels if the charge was deposited in the top of the sensor. (n,Si) interactions deep in the sensor provide a possible explanation for this distribution.

3.5.4 Time Distribution of Clusters

Figure 3.14 shows the number of measured clusters as a function of time with the Timepix detector placed outside of the beam in the reference position. It also shows the beam intensity measured with the reference IC. There is a good correlation between the two data sets, which raises the possibility of using a hybrid pixel detector as an indirect monitor of beam intensity at CERF and other energetic mixed fields.

3.5.5 Discussion

This chapter has discussed how tracks form in a Timepix detector and how this information can be analysed to obtain useful dosimetric outputs. The physics of energy

deposition in silicon by photons, electrons and charged particles was discussed, and how charge transport in silicon forms the measured signal. Common data analysis problems and some tools were discussed. The calculation of basic track parameters and how these can be used to sort clusters into different morphological categories was explained, as well as the calculation of more useful cluster properties such as $\mathrm{LET_{Si}}$ or polar angles. In the next chapter(4), the interpretation of these values into dosimetric quantities is explored.

The properties of different morphological cluster categories in the Timepix detector have been investigated. Clusters in the CERF mixed field sorted by morphology have widely overlapping $\mathrm{LET_{Si}}$ distributions. However, this does not mean that this information is not useful. One category of clusters identified at CERF ("Straight Light" tracks which probably correspond to muons) originates from a different point in space to the others, but would not be identifiable on the basis of $\mathrm{LET_{Si}}$ alone. Angular information provides an additional degree of freedom for mixed field disentanglement, especially if one expects the field to be highly anisotropic. This is the case for many accelerator based measurements.

The information in 'blob' like clusters is hard to extract useful quantities from, because the range of the particles is unknown. Like track $\mathrm{LET_{Si}}$ distributions blob energy distributions produced by our clustering algorithm also overlap considerably. Separation of (n,Si) interactions from charged particle interactions remains an open question in fields with a substantial neutron component.

Finally, it was demonstrated that the number of detected secondary particles produced by collision of energetic protons and pions with the copper target is proportional to the beam intensity.

On a first inspection it appears that the additional information gathered by the Timepix detector is quite complex for the assessment of many mixed radiation fields. Most fields encountered in a radiation protection environment are not particularly directional. Setting up and calibrating a Timepix detector is a time consuming procedure which requires a reasonable amount of relevant technical experience, and the subsequent data analysis is relatively complicated and computationally intensive compared to other dosimetry systems. Finally work needs to be done to relate the $\mathrm{LET_{Si}}$ with the true LET over a relevant site size of the track. In chapter 6 we discuss a novel detector, the GEMPix which consists of a gas detector with a Timepix ASIC for readout where biological site sizes are extended over many pixels.

The Timepix detector does have several advantages though. In some situations the angular information is useful, and track by track dosimetric information is clearly useful in varying radiation fields. The Timepix is also compact, light weight and solid state. The lack of a case/detector wall makes it sensitive to low energy γ and β rays and the morphological information in clusters allows for the separation of tracks where a solely LET based formalism would be impossible. In the next chapter the application of the Timepix detector to dosimetry in space radiation fields is discussed. Here hybrid pixel detectors present unique advantages over existing systems.

Chapter 4

Charged Particle Dosimetry and Space Radiation Measurements with Timepix Detectors

This chapter discusses the analysis of measurements taken with 5 Timepix detectors on the International Space Station (ISS), undertaken during a period spent at the University of Houston and NASA Johnson Space Centre. The use of the Timepix to calculate relevant dosimetric quantities from the mixed ion fields in space is discussed (following the procedure devised by the University of Houston) and a study of the angular isotropies in the radiation fields on the ISS in carried out.

4.1 Introduction - The Space Radiation Problem

Astronauts are probably the most occupationally exposed radiation workers in the world [64]. Astronauts are exposed to radiation fields primarily composed of charged particles in comparison to terrestrial fields which are normally gamma rays or neutrons. Both integral and instantaneous doses are quite large in comparison to most terrestrial radiation sources. Daily absorbed doses on the ISS are on the order of 200 µGy/day, instantaneous doses can exceed 20 µGy min^{-1} and much of the radiation has high LET for which long term biological effects are less well understood than gamma rays and neutrons (the long term effects of which are mostly well understood based on the Hiroshima and Nagasaki survivors dataset [65]). These long term effects not only

include cancer risk [66, 67], but also potentially cardiovascular [68, 69], central nervous system [70, 6] and ocular degradation [71]. Integral doses for long term space missions are high, for a potential two year Mars mission dose estimates vary between 0.25 Sv to 1 Sv (0.5 mSv/day - 1.5 mSv/day [72, 13]. An additional hazard for missions outside of the terrestrial magnetosphere are solar particle events which produce intense fluxes of protons in the 10 MeV to 100 MeV energy range [73, 74]. The Timepix detector offers several advantages as a radiation monitor in a space environment over other systems. These are the compact low weight/power nature of the Timepix detector, the ability to distinguish the angular information of the incoming radiation and the potential ability to target dosimetric end points other than LET.

4.2 The ISS Timepix Deployment

This chapter concentrates on work carried out during a secondment with the University of Houston and NASA Johnson Space Centre on measuring the differences between the South Atlantic Anomaly and the Galactic Cosmic Ray Field on the International Space Station (ISS) with Timepix detectors.

Six Timepix detectors are currently deployed on the ISS as a NASA technology demonstration [75]. Each Timepix detector is mounted on a compact USB readout designed by IEAP at CTU Prague which is approximately the size of a thumb drive and is attached to a crew laptop. The whole unit including readout is referred to as a REM (Radiation Enviroment Monitor) by NASA. The laptop runs a software package which performs an online analysis of the data calculating the instantaneous and integral dose rates. The laptops buffer the saved frame data and transfer the full data to a linux server at the University of Houston for further analysis. Figure 4.1 shows a REM in the ISS Cupola module.

4.2.1 The Radiation Field on the ISS

In low earth orbit the typical radiation field consists of Galactic Cosmic Rays (GCR), made up mostly from high energy protons but also other nuclei with high energy and charge. GCR are hypothesised to be produced by cosmic accelerators (normally supernovae) with elemental abundances following the elemental abundance at source and energy spectra which fall off as a power law. The observed field in low earth orbit

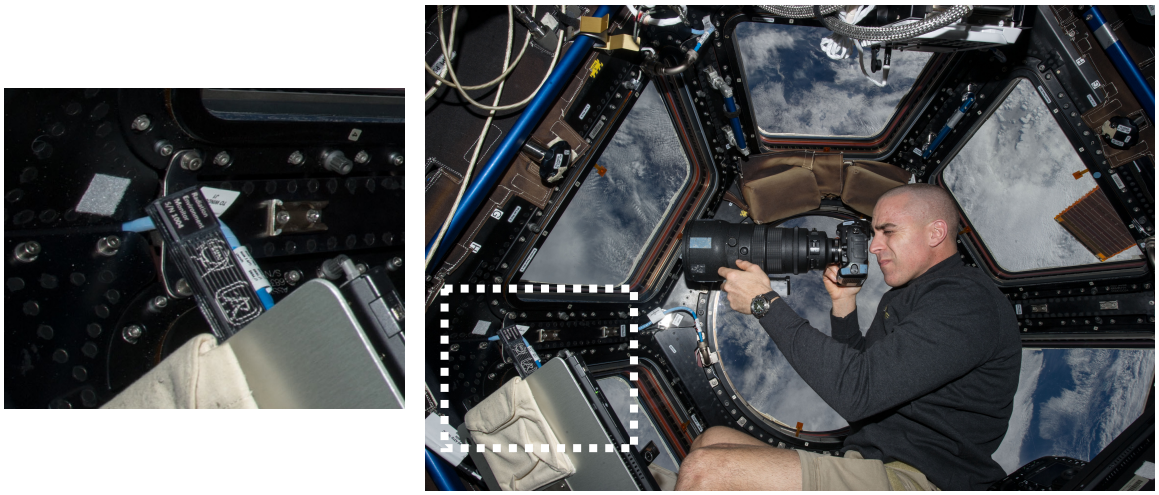

Figure 4.1: REM in the ISS Cupola module (courtesy, NASA).

is somewhat modified from the source, particles with energy below about 1 GeV being attenuated by interactions with the interstellar medium. Dominant isotopes in GCR are Hydrogen, Helium, Carbon, Oxygen, Silicon and Iron, all of which have roughly similar energy spectra falling off as $\frac{dE}{dN} \approx E^{-2.65}$. Example energy spectra and isotopic abundances for GCR are shown in figure 4.2 [76, 46].

For approximately 15 minutes each day the ISS passes through the South Atlantic Anomaly (SAA), a region over the coast of Brazil where the Earth's trapped charged particle belts[1] dip into the upper atmosphere due to the offset in the earths geomagnetic and rotational axes [77]. The SAA field is quite different from the GCR field, and contains considerably higher fluxes of particles. It is mostly composed of protons with energies between 1 MeV and 500 MeV peaking at $\approx$ 100 MeV [78].

4.3 From LET to Dose Equivalent

4.3.1 The Quality of Radiation

It has long been known that the dose deposited by radiation is not the only factor that contributes to a biological response in a person, and that some radiations like high z charged particles or fast neutrons are much more damaging per unit absorbed dose

[1] Trapped charged particles follow spiralling paths in Earth's magnetic field, bouncing back and forth between so called mirror points.

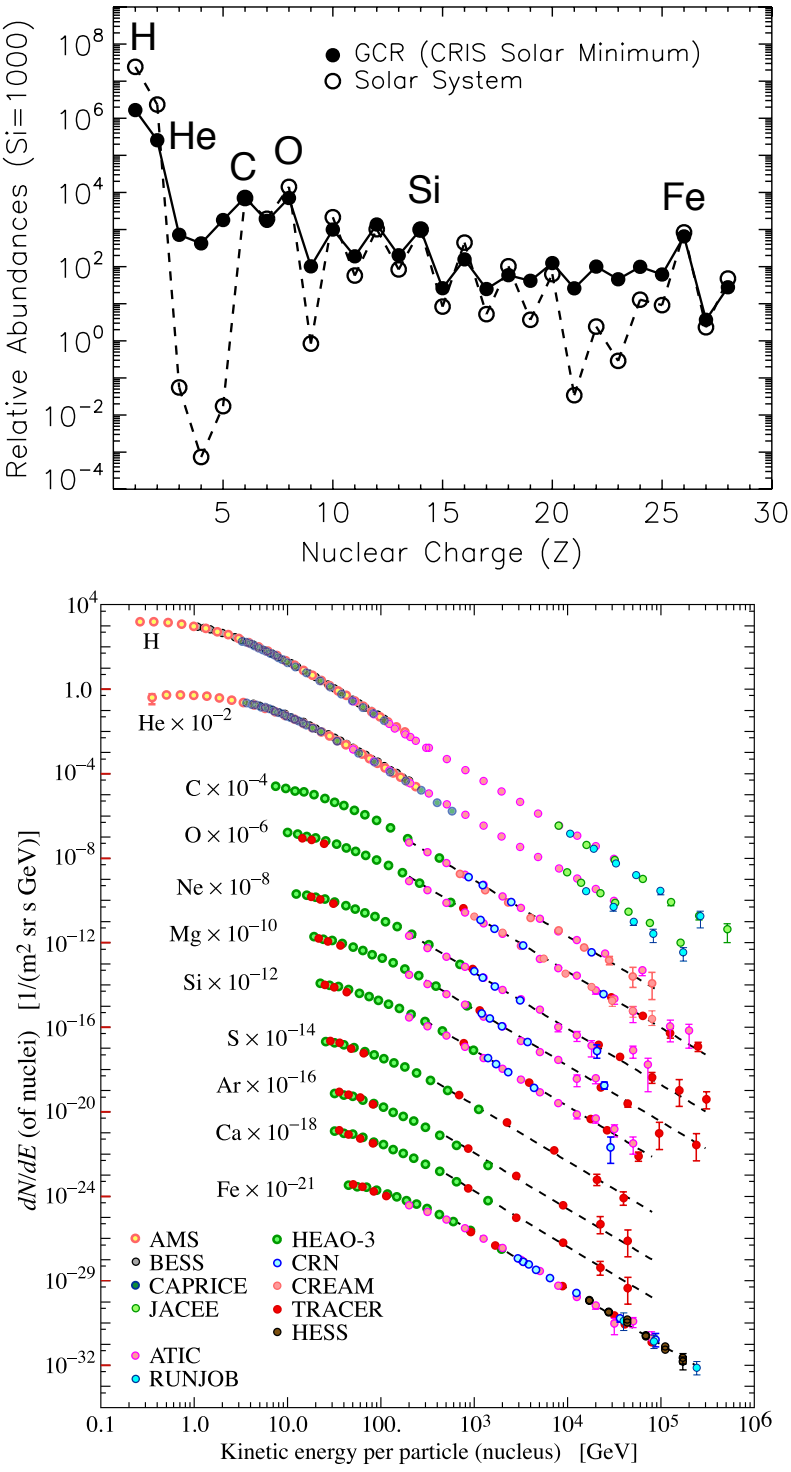

Figure 4.2: Top - Elemental abundances in the GCR at Solar Minimum compared with Solar System elemental abundances (figure reproduced from [76]. Bottom - sample energy spectra of the GCR (figure reproduced from [46]).

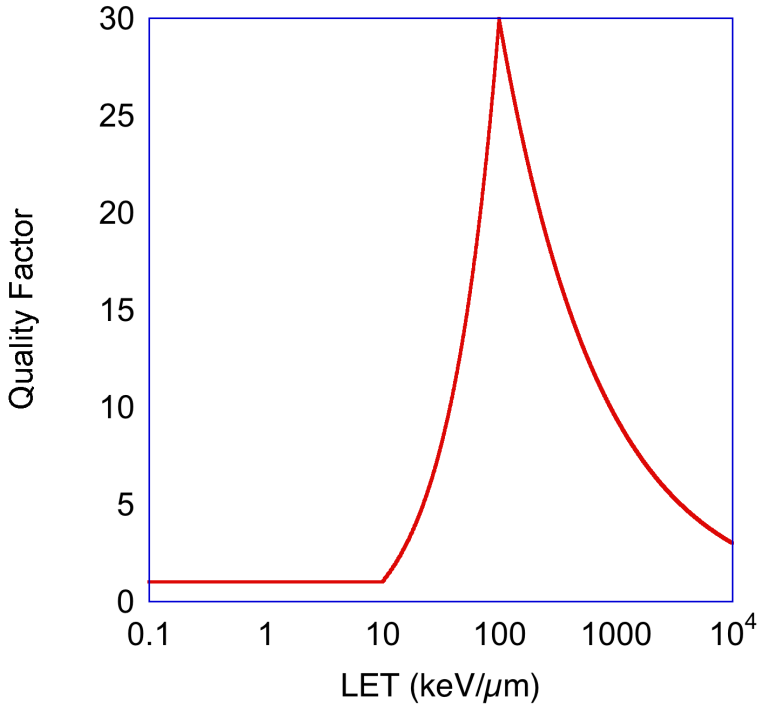

Figure 4.3: ICRP 60 Quality Factor as a Function of LET in Tissue

(D) than photons or electrons. For radiation protection purposes this is quantified in terms of the Quality Factor Q. The dose equivalent H in sieverts is defined as

$$H = QD. \tag{4.1}$$

Various formalisms for determining the Quality Factor of incident radiation exist, including that of ICRP 103 [5] which defines the quality factor in terms of incident particle type and ICRP 60 [79] which defines the Quality Factor as a function of the particle LET (in tissue). As LET is a directly measurable quantity in the Timepix detector we proceed to calculate the dose using this definition (also following the recommendations from ICRP 123 [64]). The quality factor from ICRP report 60 as a function of LET is shown in figure 4.3, and is based largely on experimental data with cell cultures targeting carcinogenic endpoints.

The shape of the quality factor curve can be explained as follows. With increasing LET the measured biological effectiveness of the radiation changes out of proportion to the simple increased dose deposition. This is thought to be because the ionisation density over biologically relevant length scales (such as cells, cell organelles or DNA strands) becomes much more concentrated with high LET radiation. Because the ionisation is more likely to be concentrated over small volumes, this allows much larger amounts of damage to be done to individual cell structures and DNA, as opposed to the low LET case where the damage is more distributed. Typically extended damage to cellular structures will be detected by the cell and trigger apoptosis (the normal, regulated procedure for cellular suicide, which occurs in approximately 0.1% of a typical adults cells daily [48]).

Specific to DNA is the hypothesised double strand break mechanism. Each strand in the double helix structure of DNA is essentially a copy of the other, providing a template for DNA repair in the event of a lesion in one of the strands. Single strand breaks are very common, and the repair mechanisms are generally very reliable, it is estimated that an average cell will undergo some 10,000 - 1,000,000 repair events per day [48]. Double strand DNA breaks on the other hand are much harder to repair as there is no template from which to regenerate the opposing strand. Cells repair DNA damage via two processes. The first is called homologous recombination and essentially involves borrowing DNA from a similar nearby DNA strand to facilitate the repair, the second is non-homologous end joining which involves removal of several nucleotides to 'patch over' a double strand break [48]. The genome of the cell can be changed by such events, and as there is no way for the body to detect such changes apoptosis is usually not triggered. Many cells with a damaged genome will die during mitosis (division), or rarely sucessfully mutate, or more rarely still mutate into a dangerous cancer. This increasing probability of double strand breaks with higher LET explains the sharp ramp up of the Q curve above $10\,\mathrm{keV\,\mu m^{-1}}$.

Above $100\,\mathrm{keV\,\mu m^{-1}}$ the the Q factor curve tends downwards. If the ionising power of radiation is high enough there is a significant probability of there being multiple traumatic events in every cell traversed by the radiation. At this point the probability begins to lie overwhelmingly in favour of damaging the cells so much that the cell is killed in all cases.

4.3.2 Silicon to Tissue Conversion Factors

Armed with the deposited dose from a track and the $\mathrm{LET}_{\mathrm{Si}}$ (defined in section 3.4.3) one can compute the dose equivalent contribution on a track by track basis if the dose deposited in silicon can be converted to the dose deposited (and hence LET) in muscle by use of an appropriate conversion factor $C_{\mathrm{Si}\to\mathrm{m}}$. The conversion factor is defined as the ratio of deposited dose in silicon to deposited dose in muscle,

$$C_{\mathrm{Si}\to\mathrm{m}} = \frac{D_{\mathrm{m}}}{D_{\mathrm{Si}}} \therefore \tag{4.2}$$

$$C_{\mathrm{Si}\to\mathrm{m}} \approx \frac{\mathrm{LET}_{\mathrm{m}}}{\mathrm{LET}_{\mathrm{Si}}}. \tag{4.3}$$

Hence the dose equivalent in muscle can be restated in terms of the dose delivered to silicon and the $\mathrm{LET}_{\mathrm{Si}}$

$$H_{\mathrm{m}} = D_{\mathrm{m}}.Q(\mathrm{LET}_{\mathrm{m}}) \tag{4.4}$$

$$H_{\mathrm{m}} = D_{\mathrm{Si}}.C_{\mathrm{Si}\to\mathrm{m}}.Q(\mathrm{LET}_{\mathrm{Si}}.C_{\mathrm{Si}\to\mathrm{m}}). \tag{4.5}$$

where H_{m} is the dose equivalent in muscle, D_{Si} the absorbed dose in silicon, $C_{\mathrm{Si}\to\mathrm{m}}$ the silicon to muscle conversion factor and $Q(\mathrm{LET}_m)$ the ICRP 60 Quality factor which is a function of the LET in muscle LET_m.

In the literature the most common approach to converting the dose in silicon to the dose in tissue in a mixed field is to use a constant conversion factor, normally estimated using Monte Carlo [80]. However the morphological nature of the data gathered by the Timepix detector and a knowledge of the normal incident radiation field in space allows for a separate approach based on an estimation of particle conversion factor on a track by track basis.

Figure 4.4 shows the ratio of stopping powers between muscle and silicon as a function of charged particle energy. Above about 200 MeV the stopping power ratio is flat ($C_{\mathrm{Si}\to\mathrm{m}} = 1.23$) however below roughly 1 GeV the stopping power is a function of particle energy as shown in figure 4.4.

In order to estimate the conversion factor it is first necessary to estimate the particle energy. It is clear from figure 4.2 that the dominant isotopes in the GCR

below $Z = 12$ are Hydrogen, Helium and Carbon. $\frac{dE}{dx}$ curves for these three ions as a function of particle energy are shown in figure 4.5. Carbon ions can be discriminated from helium and protons as they emit distinguishable delta electrons at all energies, while protons and helium nuclei do not. The particle energy can then be estimated using the following procedure.

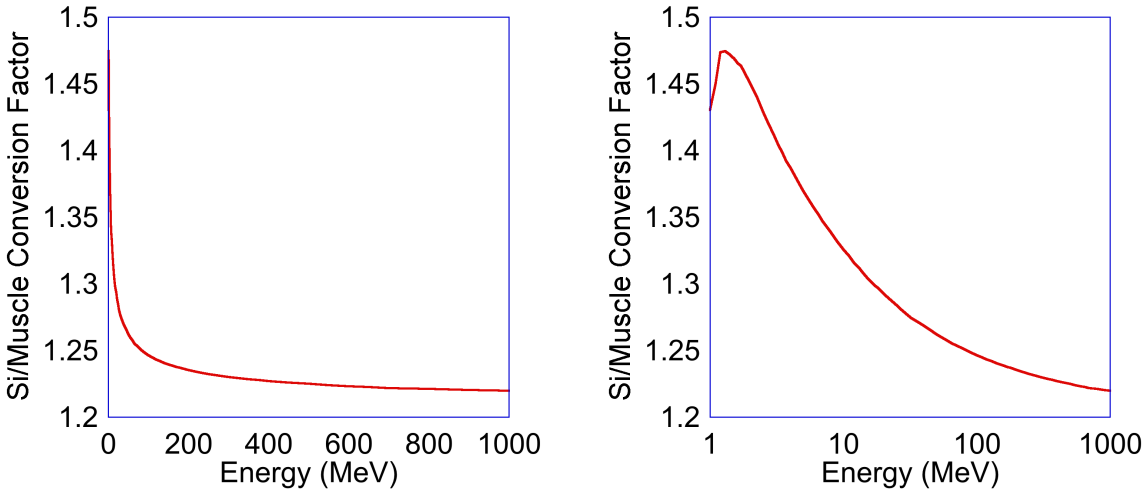

Figure 4.4: Silicon to muscle conversion factors for heavy charged particles as a function of particle energy (left - energy scale linear, right - logarithmic).

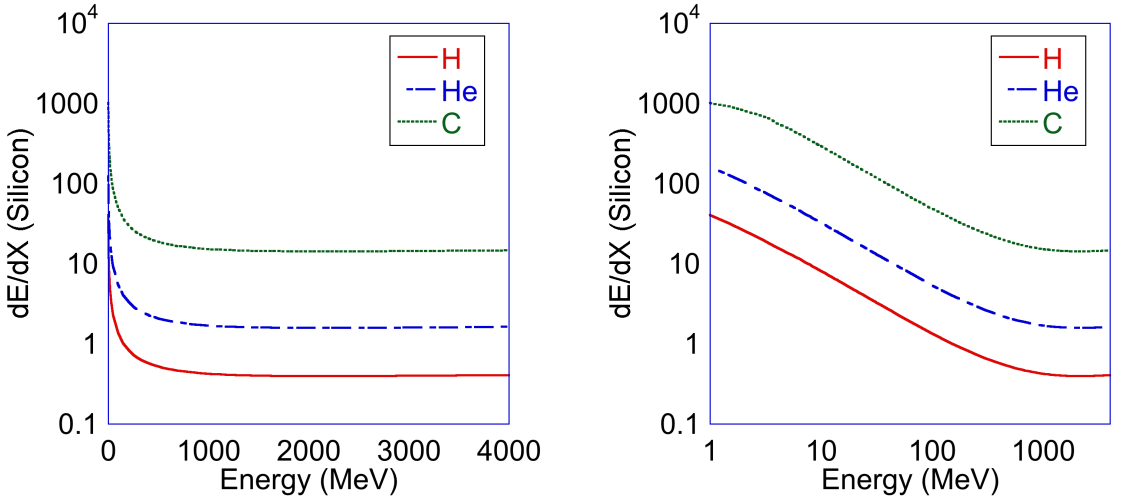

Figure 4.5: $\frac{dE}{dx}$ as a function of particle energy for H, He and C (left - energy scale linear, right - logarithmic).

- If there are visible delta electrons assume the ion is carbon and read the energy off from figure 4.5

- Otherwise pick the lowest compatible energy with the measured $\frac{dE}{dx}$ from the curves for protons and helium nuclei in figure 4.5.

Clearly such an algorithm is not perfect, and one place it fails is in discriminating fast alpha particles from slow protons, but by consistently picking the lowest energy option compatible with the cluster morphology one always picks the highest possible conversion factor, and so such an error leads only to an overestimate of the absorbed dose and LET in tissue. Ions with $Z > 6$ are significantly attenuated by the interstellar medium below $E \approx 1\,\mathrm{GeV}$ and because of this the error introduced by slow heavy ions should be small.

Dose equivalent rates measured on the ISS with 2 Timepix detectors compared to a Tissue Equivalent Proportional Counter (which does not need a silicon → tissue conversion as it measures energy deposition in a 'tissue equivalent' gas mixture) are shown in figure 4.6.

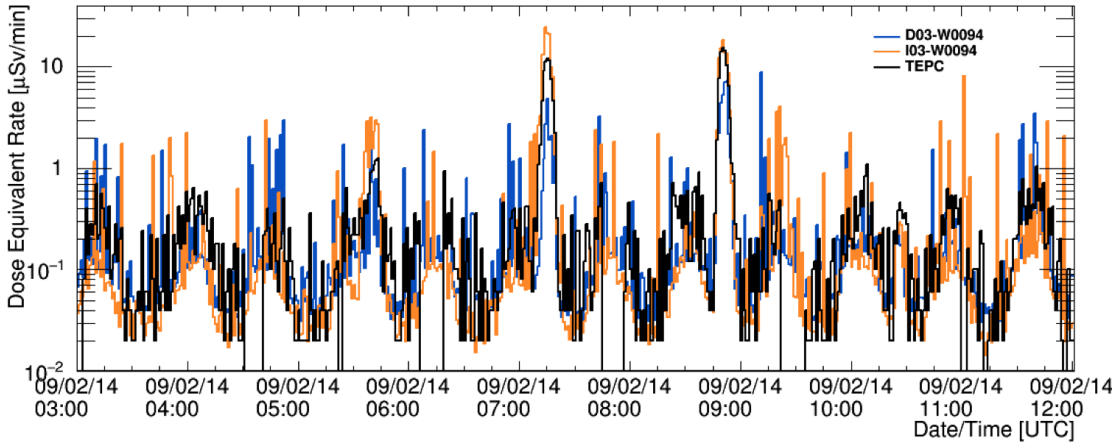

Figure 4.6: Comparison of dose equivalent rates measured with a Tissue Equivalent Proportional Counter (The IVTEPC instrument [81]) and two Timepix detectors on the ISS. The Timepix detector data is more noisy than the TEPC as the active volume of the detectors is substantially smaller. Each spike typically represents the detection of a single high z cosmic ray. SAA passes are visible as the two regions with a sustained dose rate over $10\,\mu\mathrm{Sv\,min^{-1}}$. Plot courtesy [82].

4.4 Absorbed Doses in the GCR and SAA

Figure 4.7 shows the absorbed dose rate as a function of ISS position for the first six months of 2014, the SAA is clearly visible as the region of high dose rate over Brazil.

The SAA contributes around 30% - 50% of the total absorbed dose taken by astronauts on the ISS[83]. Figure 4.8 shows daily absorbed dose rates for the month of April 2014 measured by a single Timepix detector in the ISS Columbia module split into SAA and GCR components. In general the GCR dose is flat at around 100 µGy/day while the SAA dose varies between 75 µGy/day and 125 µGy/day. This is probably due to the fact that the station can pass through the SAA a variable number of times in a 1 day period. Figure 4.9 shows example data taken over 20 s in the GCR and 0.7 s in the SAA measured with a Timepix detector. The tracks in the SAA frame show a clear angular dependence and have a higher LET (more energy in each pixel) than the tracks in the GCR frame.

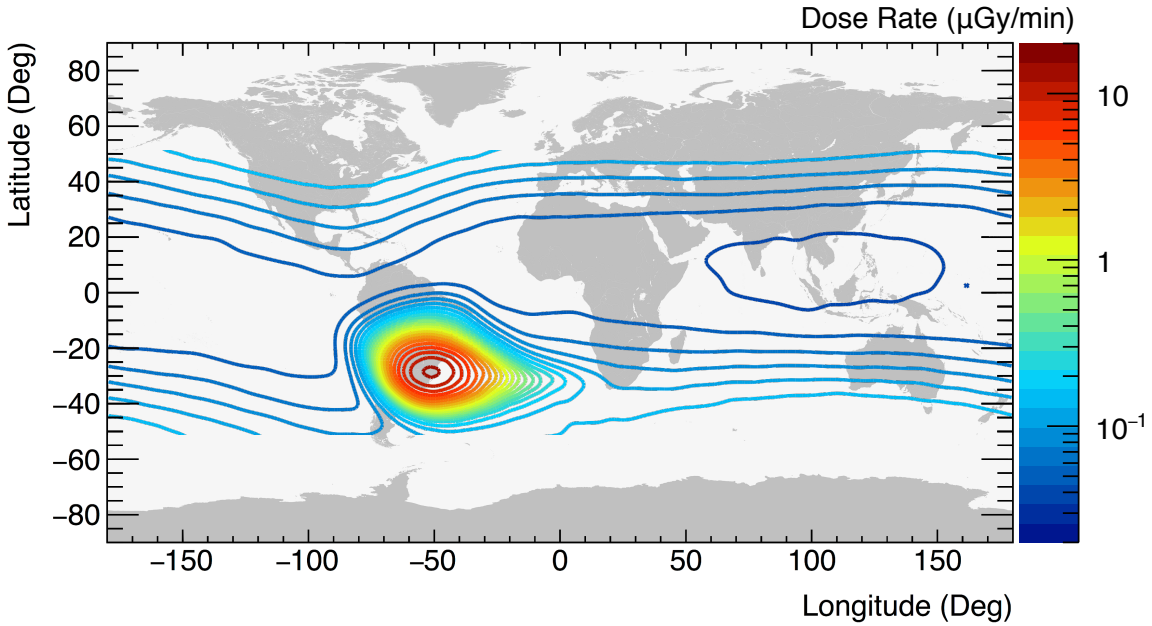

Figure 4.7: Extracted absorbed ISS dose rate contours for the first six months of 2014, averaged over all (5) deployed detectors.

Figure 4.10 shows the instantaneous variation of the dose rate with altitude on the ISS over 5 hours and 1 year. In general the trend in the instantaneous dose rate matches the orbital altitude. Over 1 year the dose rate from the SAA appears to fall as the station ascends (the ISS orbit slowly decays due to atmospheric drag and requires periodic boosting) while the GCR dose rate remains constant.

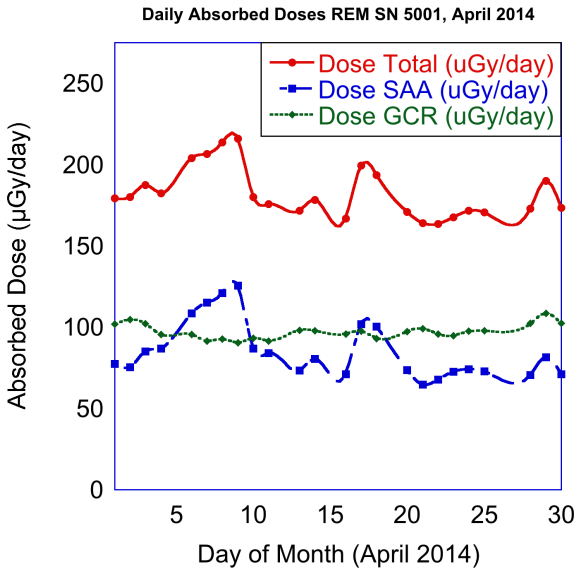

Figure 4.8: Daily dose rates measured with a single Timepix detector split into GCR and SAA components, April 2014.

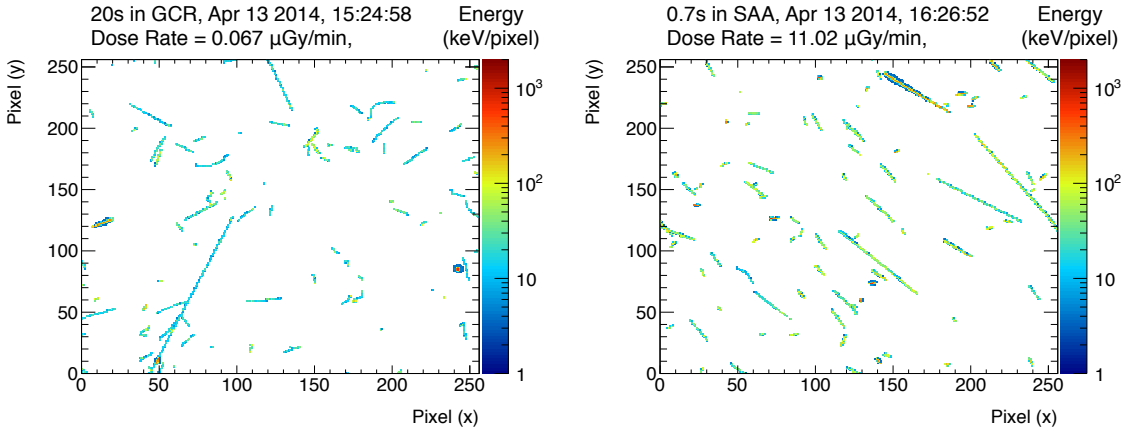

Figure 4.9: Data taken taken over 20 s in the GCR (left) and 0.7 s in the SAA (right) with a Timepix detector.

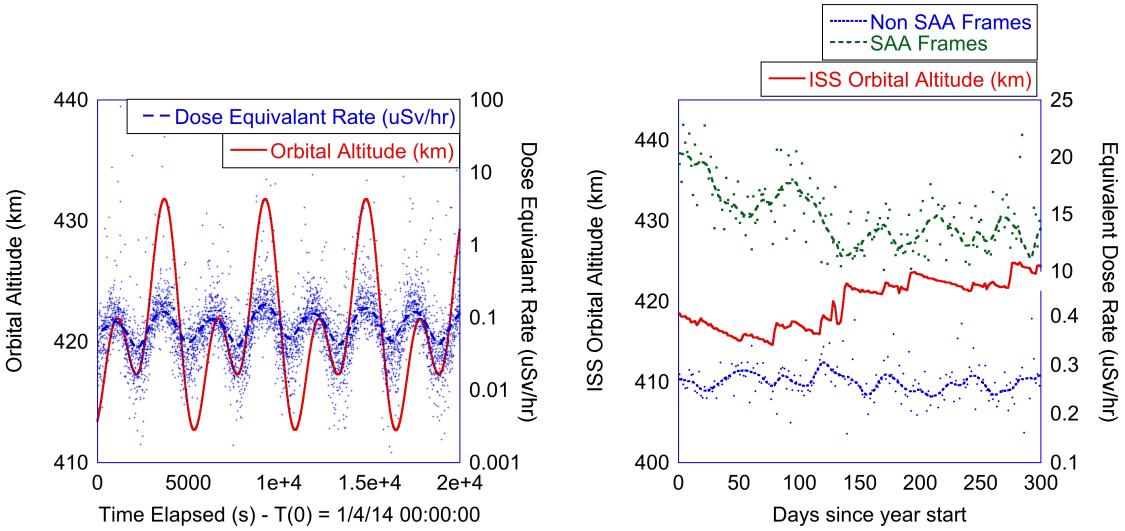

Figure 4.10: Variation of Dose Rate with Altitude on the ISS. Left - over 5 hours, Right - over 2013, split into SAA and GCR components. All line fits were performed with the LOWESS method [84]. Dots are the data, lines are the fit to dose rate.

4.5 LET, Tissue Conversion Factor and Quality Factor Spectra

Measured $\mathrm{LET_{Si}}$ spectra in both the SAA and GCR are shown in Figure 4.11a and the microdosimetric distribution (weighted by total absorbed dose) is shown in figure 4.11b. The SAA spectrum is dominated by a peak between 1-10 $\mathrm{keV\,\mu m^{-1}}$ which is associated with protons. The GCR spectrum has 3 peaks, one at 0.4 keV/um which is mainly energetic electrons (both native to the GCR and produced by interactions with the ISS shielding) and 2 high energy peaks at 100 $\mathrm{keV\,\mu m^{-1}}$ and 250 $\mathrm{keV\,\mu m^{-1}}$ which are suppressed in the SAA data. Both GCR and SAA spectra feature a superfluous peak at 14 $\mathrm{keV\,\mu m^{-1}}$ which is associated with an incorrect track length calculation for stopping protons which needs to be corrected.

Derived silicon to tissue conversion factors are shown in figure 4.12. The majority of the GCR is in the highest energy ($C = 1.23$) bin, while the SAA has a wider distribution due to the increased prevalence of low energy protons.

Derived ICRP Quality Factors for the SAA and GCR are shown in figure 4.13. In both cases the majority of the distribution is in the $Q = 1$ bin and the shape of the distributions is quite similar, especially for $Q > 20$.

Figure 4.14 shows maps of average (per detected track) $\mathrm{LET_{Si}}$ and derived ICRP

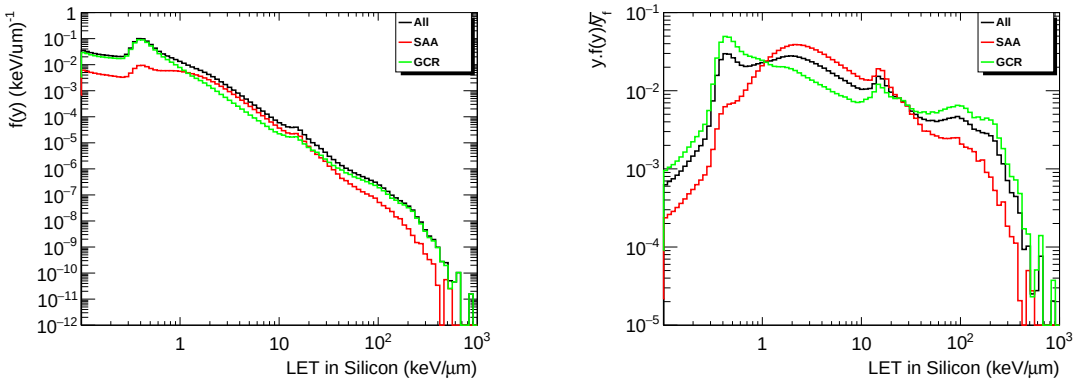

(a) LET Spectrum (b) Microdosimetric Spectrum

Figure 4.11: LET Spectra for the first six months of 2014 split into SAA and GCR components in terms of the absolute probability $f(y)$ left and dose weighted representation $y.f(y)/\bar{y}_f$ right. Please note that in the dose weighted representation all plots are independently normalised. The peak around 14 keV µm^{-1} is due to incorrect track length calculation for protons with less than 10 MeV which stop in the sensor.

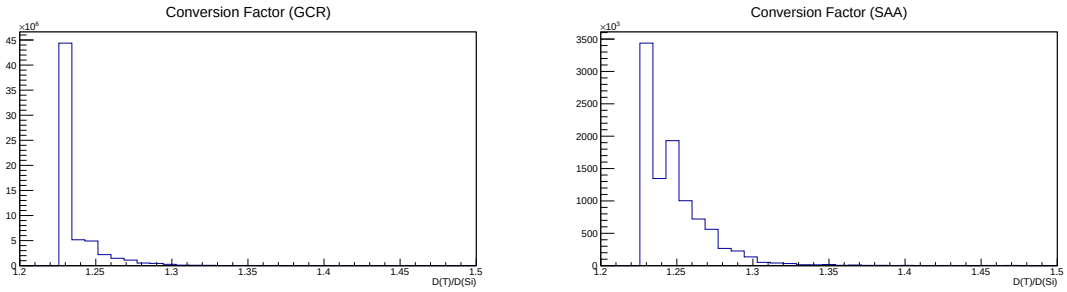

Figure 4.12: Measured silicon - tissue conversion factors on the ISS, left - GCR, right - SAA.

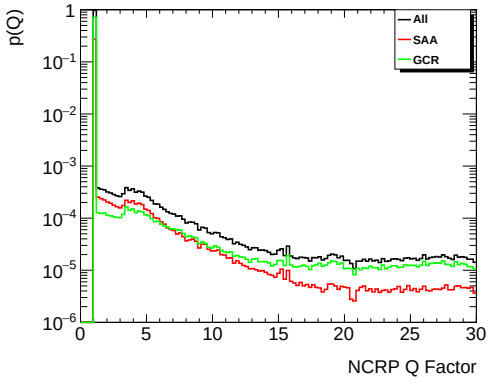

Figure 4.13: Quality Factor spectrum for the first six months of 2014 split into SAA and GCR components.

60 Quality Factors as a function of station position. It shows that the average Quality Factor is higher in the SAA ($\bar{Q}_{\mathrm{SAA}} \approx 1.1$) than the GCR ($\bar{Q}_{\mathrm{GCR}} \approx 1.03$). This is somewhat surprising as the Quality Factor for GCR cosmic rays should be higher than that for SAA protons. The reason for this is the relatively large fraction of electrons in the GCR and the low minimum energy sensitivity of the Timepix detector. If a cut of 1 keV µm^{-1} in LET is applied, removing most of the electron/minimum ionising contribution the result inverts and $\bar{Q}_{\mathrm{SAA}} \approx 1.1$, $\bar{Q}_{\mathrm{GCR}} \approx 1.3$.

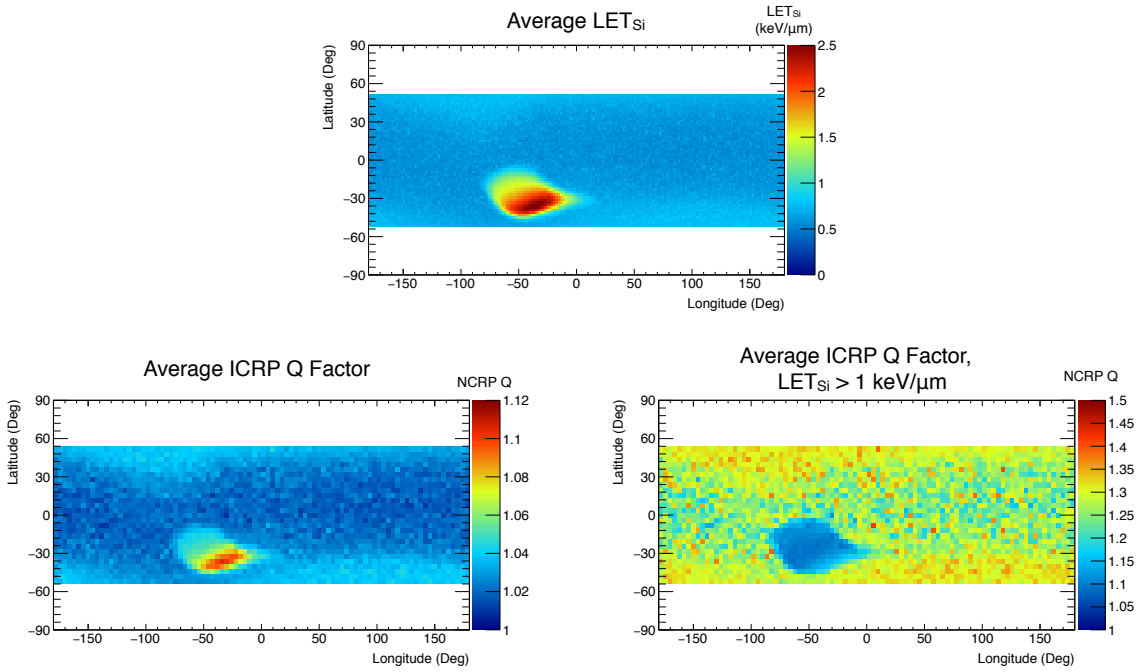

Figure 4.14: Maps of the average $\mathrm{LET_{Si}}$ and Quality Factor with and without a minimum $\mathrm{LET_{Si}}$ cut for the first six months of 2014.

4.6 Angular Distributions in the SAA and GCR

A unique capability of the Timepix detector (and other hybrid pixel detectors) among space dosimetry systems is its capability to determine the incident angle of incoming radiation. In principle the Timepix detector is sensitive to the whole 4π steradians of the sky but its resolving power within that space is more limited. The angular information produced by a fast primary track is nominally limited to 90 degrees of altitude and 180 degrees of azimuth. This is because it is impossible to tell if a particle is going up or down, and left or right.

In the current Timepix detector on the ISS, determination of the absolute angle of the devices is impossible. This is because each device is attached to a workstation computer, which is in turn attached to a mobile arm that is moved by the ISS population on an ad-hoc basis. As the dosimetric information in the sensors is computed on a per particle basis, the angle of the sensor has no impact on the overall calculated astronaut dose.

Sample frames in the GCR and SAA are shown in Figure 4.9. The SAA field has clear directionality compared to the GCR distribution. The source of the directionality could either lie in the inherent nature of the field, or be due to the ISS shielding in the region of the Timepix detector.

Figure 4.15 shows a heat map of angular distributions for 4 Timepix detectors split into SAA and GCR components over April 1st 2014. The SAA data shows clear directionality, while the GCR frames are isotropic. Over this period some or all of the devices may have had their orientations changed which could account for some of the anisotropy.

Figure 4.16 shows minute by minute heat maps of the azimuth and altitude distributions for a single pass of the SAA at 4:13 am UTC on April 20th 2014. It was assumed that the device orientation is not changed over this SAA pass (it should be noted that ISS astronauts keep UTC, and so are unlikely to be using the laptop at the time of the measurement). The field is clearly consistently structured and evolves continuously in time.

Figure 4.17 presents this data in a more quantitive way. Absorbed dose, average altitude and azimuth angles and average track length in the Timepix detector are plotted in 10 minute bins as a function of time from April 20th to April 25th 2014. The peaks in dose rate correspond to SAA passes and correlate to the peaks in the track angles. A direct consequence of these changes is that the average length in the detector is different to the GCR value. The average track length is dependent on the anisotropy of the field and the orientation of the device. The track-by-track method of dosimetry used in the Timepix detector is insensitive to such a variation, however it has important implications for dose rate calculations in other detectors.

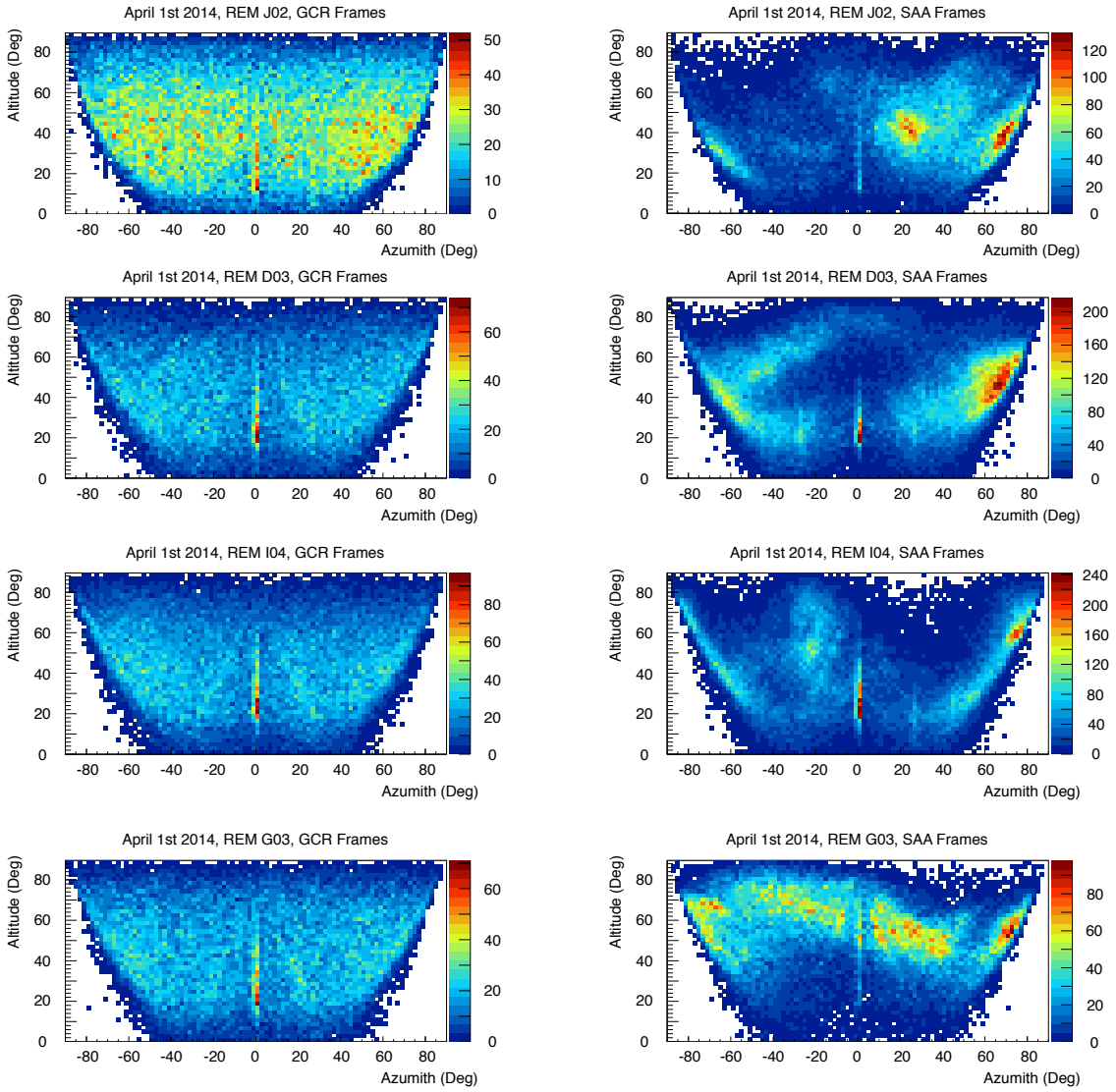

Figure 4.15: Heat maps showing angular distributions of tracks in 4 Timepix (REM is the NASA acronym for the complete system deployed on the ISS) units on April 1st 2014 in the GCR and SAA. The SAA data demonstrates clear anisotropy in comparison to the GCR.

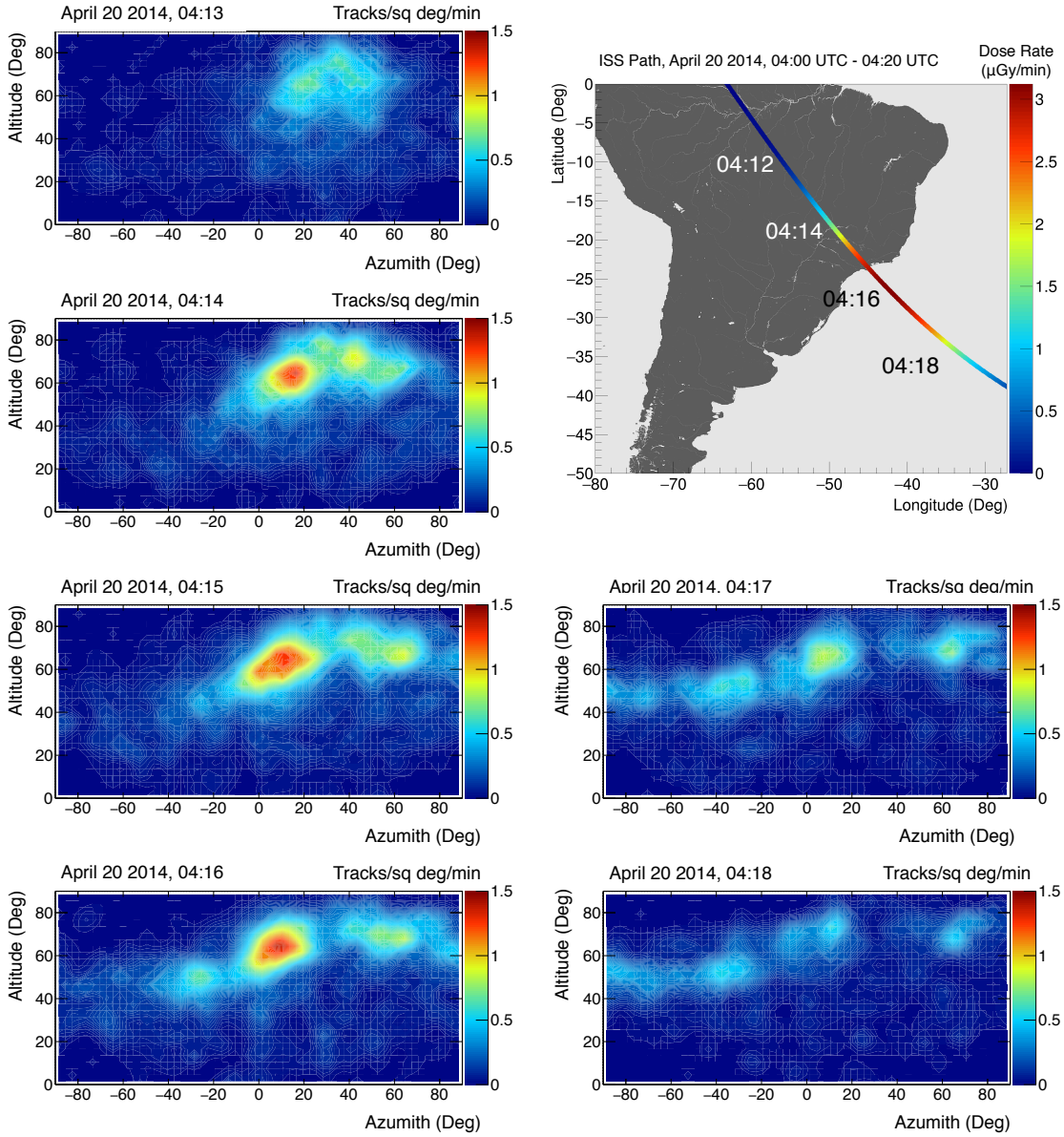

Figure 4.16: Minute by minute heat maps of the angular distribution of tracks during an SAA pass. The path of the ISS and dose rate are shown in the top right.

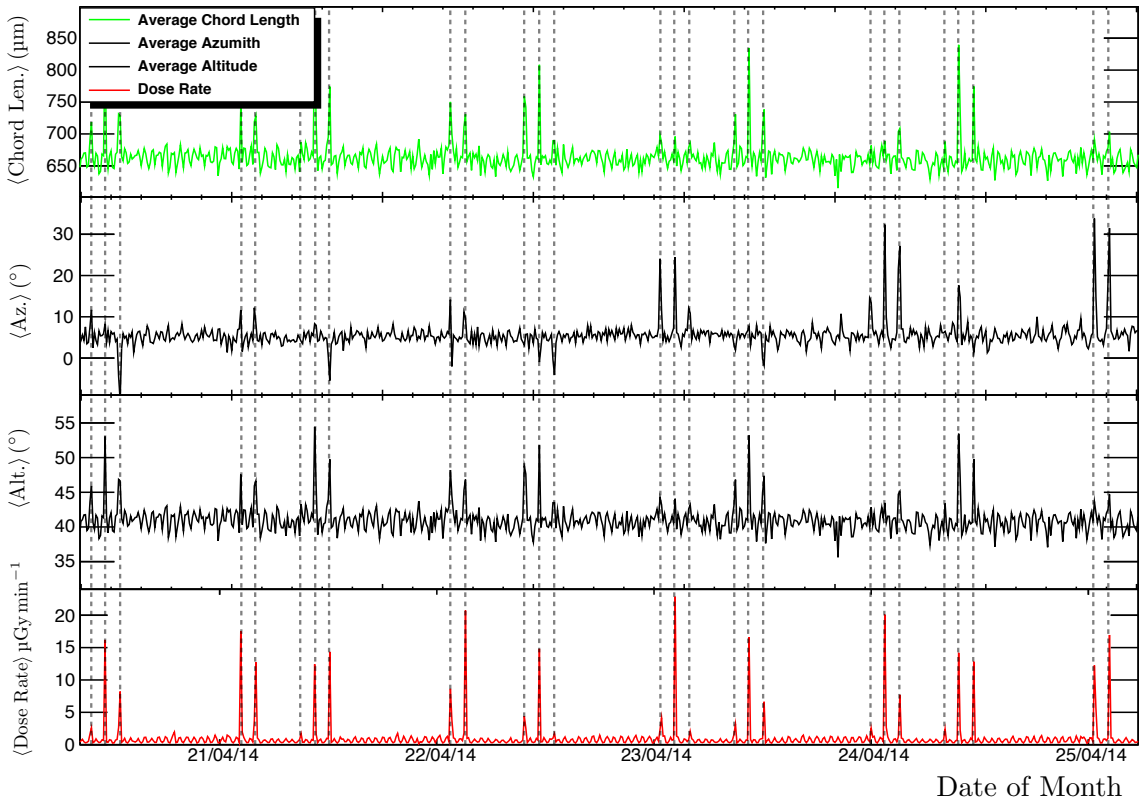

Figure 4.17: Dose rate, average azumith, altitude and mean chord length in 10 minute bins for 5 days in April 2014. SAA passes are shown with dashed lines.

4.7 Discussion and Conclusions

The current prototype Timepix detector deployment on the International Space Station and calculation of dosimetric quantities was discussed. LET and Quality Factor distributions inside and outside of the South Atlantic Anomaly were presented, as well as plots of average Quality Factor, Silicon to Tissue Conversion Factor and LET. The South Atlantic Anomaly field measured inside the ISS shows considerable anisotropy in all deployed Timepix detectors. One consequence of this anisotropy is that the mean chord length of the incident radiation field is different to that of the Galactic Cosmic Ray field.

Other detectors used for dosimetry measurements in space such as Tissue Equivalent Proportional counters [85] assume a mean chord length, typically calculated for an isotropic field. As the chord length of the SAA field inside the ISS is continuously variable this could lead to a systematic error in measurement of LET in directional fields. Other detectors such as the RAD on the Mars Curiosity Rover [86] have a limited field of view so measured LET values should remain accurate. However in a directional field such detectors may under or over estimate incident particle fluxes depending on if the detector aperture is in or out of field.

Outside of low Earth orbit such anisotropic fields are expected to be encountered in future space missions. The Orion program envisages trips to Lunar orbit which would entail humans travelling through the Van-Allen belts for the first time since the Apollo program, and trips further afield such as to nearby Asteroids or Mars will have to deal with space weather including solar particle events which are intrinsically directional particle fields.

Outside of its particle by particle tracking capability the Timepix detector offers several economical advantages as space dosimeter, these are its weight (low earth orbit launch costs are some $10,000 per kilogram), size and power consumption.

Another advantage of the Timepix detector is that the basic quantity gathered does not have to be LET, indeed in an ideal situation it may not be the most desirable quantity in the space radiation environment. Cucinotta et al [87] found significantly different delta electron distributions for ions with different charges but identical LET values over microdosimetric site sizes, and suggest that the relevant biological quantity is not LET, but instead the upward part of the curve is dependent on

$$Q \propto e^{-z^2/\beta^2} \tag{4.6}$$

where z is the particle charge and β the velocity.

One potential strategy is to use the Timepix detector more like a particle spectrometer, separating tracks into charge and velocity bins based on a more sophisticated analysis of track morphology. This data could be used to feed alternative quality factor formalisms, or as the inputs for Monte Carlo simulations. Finally it should be noted that if the inherent inchoate radiation distribution (i.e. the delta electron distribution for a charged particle) is only a function of $\frac{z^2}{\beta^2}$ then in principle one simply needs to know a 'true' microdosimetric spectra for any given $\frac{z^2}{\beta^2}$ point, and to convolve such spectra with the $\frac{z^2}{\beta^2}$ distribution measured in order to produce microdosimetric outputs from a Timepix detector.

Chapter 5

Neutron Dosimetry with a Timepix Detector and a Structured Plastic Converter

This chapter describes the design and characterisation of an energy independent fast neutron dosimeter based on a stacked plastic converter. The converter is initially designed using Geant4 Monte Carlo simulations. A prototype is then 3D printed and characterised at the NTOF neutron time of flight facility at CERN.

5.1 Introduction

Neutron dosimetry is difficult. The primary reason for this is that neutrons interact quite differently in human beings than they do in detectors due to the differing chemical compositions and sizes of detectors and people [88]. Like photons, neutrons are not directly ionizing particles, instead they are only detectable through their secondary interactions. Unlike photons, which almost always produce a secondary electron, neutrons have a wide variety of possible secondary products, and these secondaries are dependent on the chemical makeup of the material they are traversing. Neutrons are also difficult to shield as they do not interact with the electrons of a material as photons do, but instead with the much smaller nucleus, so the cross sections and attenuation coefficients for neutrons tend to be smaller than those for photons.

The primary way that fast neutrons cause damage to people is through elastic

scattering off hydrogen in water. The energy of the resultant proton E_p depends on the scattering angle θ

$$E_p = (1 - \cos\theta)E_n. \tag{5.1}$$

For fast ($\gtrsim$1 MeV) neutrons the protons produced have a short range (< 1 cm) in tissue, and so nearly all stop in a person. The highest LET (and hence biological effectiveness) for stopping protons is found in the Bragg Peak, so a neutron that undergoes repeated small angle scatters, creating several low energy protons is more biologically effective than a neutron that loses most of its energy in one large angle scatter creating a single high energy proton. Very high energy neutrons ($E > 200$ MeV) are hence less biologically effective as they produce a spectrum of energetic secondary protons which may exit a person without stopping.

5.1.1 Neutron Dosimetry and H*(10)

One strategy for performing neutron dosimetry is mirrored by the formalisms used in earlier chapters - determine a spectrum of incident neutrons and then weight the deposited energy by some quality factor. Neutron spectroscopy equipment tends to be both large and cumbersome such as Bonner Spheres [89]. In principle to perform dosimetry one needs to somehow reproduce the complete spectrum of neutron interactions inside a person (which is dependent both on depth, as the spectrum is attenuated and correct chemical composition) to accurately measure the dose delivered by neutrons. In such situations one is in practice restricted to measuring inside tissue equivalent or water phantoms or using Monte Carlo simulations. For practical dosimetry other quantities can be used such as H*(10), the ambient dose equivalent.

H*(10) is a operational dosimetric quantity developed by the ICRP. It is designed for monitoring strongly penetrating radiation in an area (i.e. not personal dosimetry, the instrumentation which is typically carried by an individual at all times). It is defined as the dose at 10 mm inside the ICRU sphere. The ICRU sphere is 30 cm diameter plastic sphere composed of 76.2% oxygen, 11.1% carbon, 10.1% hydrogen and 2.6% nitrogen which roughly approximates a human body in both composition and size. H*(10) is a useful quantity because it is precisely defined and provides a

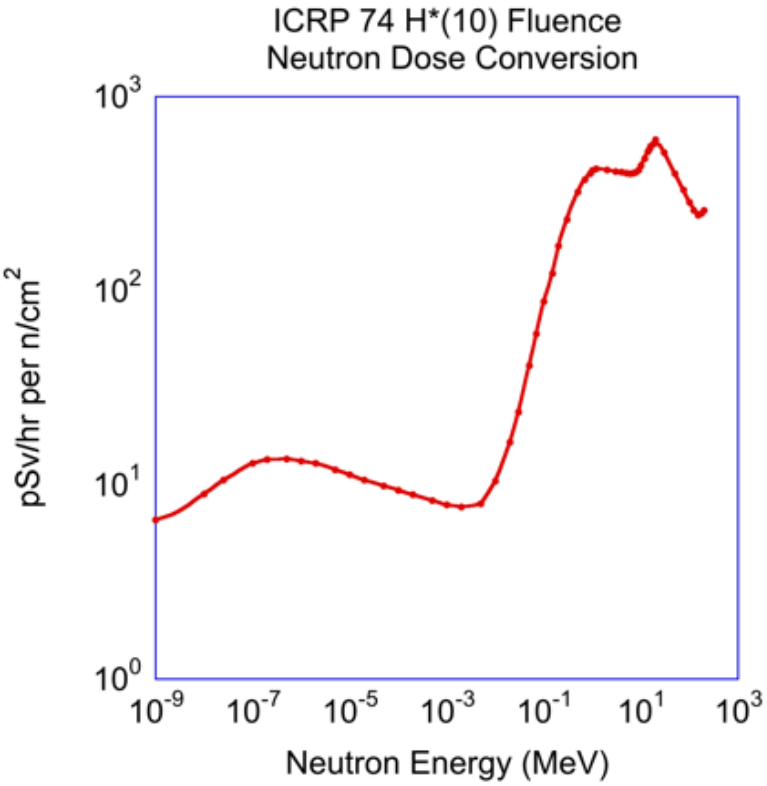

Figure 5.1: Neutron fluence to H*(10) conversion coefficients, from [1].

conservative estimate of effective dose [90]. ICRP report 74 [1] provides conversion coefficients from neutron fluence to H*(10) in sieverts, these coefficients are shown in figure 5.1.

5.1.2 The Multilayer Converter Concept

The objective of this work is to produce a converter layer that sits on top of a Timepix detector with a response which is equivalent to the neutron fluence to H*(10) conversion curve over a given energy range and so energy independent for that energy range, following the Monte Carlo studies of Othman [91]. With respect to that work the simulations used here should more accurately reproduce the detector response.

The converter design is based on a variable thickness polyethylene geometry stacked on top of a Timepix detector. Polyethylene is well known to be sensitive to fast neutrons, specifically to elastic scattering off the hydrogen nuclei that comprise two

thirds of the atoms (14% of the mass) in the polymer.

The essential idea of the dosimeter is that each thickness of polyethylene will have a difference in terms of the simple number of protons it emits (i.e. the response) at some given energy. We then call the response of some thickness t of polyethylene with energy the response function $R(t, E)$. The principle is then to see if some linear combination of these response functions can be used to reconstruct the ambient dose equivalent H*(10) over a range of neutron energies. In order to compute the dose, one simply needs to measure the response in each section and add them together with the appropriate weighting factors for the section to get an output in Sieverts.

5.2 Monte Carlo Simulation Details

Several assumptions about the Timepix detector are made in these simulations based on the operational description given in chapters 2 and 3. These are as follows:

- We can distinguish tracks from protons and other reasonably energetic heavy charged particles with those from photons and electrons. For now we do not consider any attempts to distinguish different species of heavy charged particles.
- The detector has no dead time, the frame time is set to such a value that particle tracks never overlap (a realistic proposition for dosimetry, where count rates are low).
- We can measure the energy deposited by an individual cluster by summing over the energy deposited in the pixels in that cluster, given that we take into account the fact that secondary particles (specifically delta electrons) that are contained within the track structure will be hidden by the charge sharing effect detailed earlier.

All of the simulations detailed in this study were carried out using Geant4.9.6 [92]. Electromagnetic physics was modelled using the Livermore low energy physics package. Hadronic Physics was modelled using the quark gluon string plasma model with a binary ion cascade. These models are known to accurately model fast neutron physics and recommended for energies less than 20 MeV [93]. Radioactive decay of particles was also modelled in the simulation. The tracking cut for secondary particles

Process Type	Model
Electromagnetic	`G4EmLivermorePhysics`
Hadronic	`QGSP_BIC_HP`, `G4EMExtraPhysics`, `G4HadronElasticPhysicsHP`, `G4StoppingPhysics`, `G4IonBinaryCascadePhysics`
Decay	`G4DecayPhysics`, `G4RadioactiveDecay`

Table 5.1: Geant4 Physics Models used in the Simulation

(after which their energy is deposited locally and is considered to 'belong' to the parent) was set at 5 µm, which is 10% of the pixel pitch. Details of the models used are shown in table 5.1.

5.2.1 Geant 4

Geant4 (*GEometry ANd Tracking, v4*) is a Monte Carlo [94] toolkit designed to simulate the passage of particles through matter. Originally designed for high energy physics detector design and simulation at CERN, Geant4 has found widespread application in a variety of areas in physics including medical physics and dosimetry.

The basic geometry of the simulation was a slab of silicon corresponding to the silicon sensor of a Timepix detector. It measured 14.08 mm by 14.08 mm by 300 µm. This volume was voxellised into 256 by 256 voxels of size 55 µm × 55 µm × 300 µm. Each voxel corresponds to size of one real pixel in the Timepix sensor. The simulation outputs the pixel coordinates of any energy deposition, the amount of energy deposition and the particle type.

As with a real, calibrated Timepix detector our simulation outputs the energy deposited by a particle pixelwise. Therefore an algorithm was developed to sum along the track in silicon in order to reconstruct the energy deposited in the same way that one would cluster pixel hits in a Timepix. This is shown diagrammatically in Figure 5.2. There is no attempt to reconstruct the solid state charge sharing effect in silicon in this work because we quantify the response in terms of number of particle hits, and this should not be significantly changed by charge sharing.

The assumptions made are that charge sharing exists so short ranged secondaries are not seen and also that the range of no secondary will exceed the charge sharing.

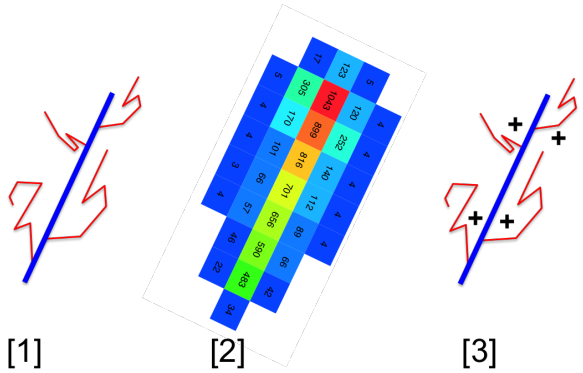

Figure 5.2: Diagram showing the track summing used in the simulation in order to account for the charge sharing effect. Geant4 creates a detailed simulation of the track of the particle down to the delta electrons [1]. However the detector measures a cluster, where the delta electrons are obscured by their short range and the charge sharing effect as shown in the measured proton cluster in [2] (numbers represent energy measured in the pixel in keV). Therefore we sum across the track in order that the simulation outputs the same energy that would be recorded in a measurement [3].

This is a perfectly reasonable assumption. The highest energy neutron considered in this work is 15 MeV. This in turn can produce a 15 MeV proton of mass m in an elastic scattering reaction with a hydrogen nucleus in polyethylene. The maximum energy this proton can then produce in a collision with an electron of mass m_0 is $4Em_0/m$, which results in a 30 keV electron ($E = 15$ MeV) [3]. The range of this electron is about 10 µm, far smaller than a single pixel [47]. The essential idea is that the output of the simulation should roughly represent the output from a Timepix detector after clustering and calculation of cluster properties.

Finally in general the simulation was developed with flexibility and extensibility in mind. The command line library TCLAP (http://tclap.sourceforge.net) was used to give a wide set of functionality directly from the command line allowing easy configuration of optimal geometry components beyond the silicon sensor (such as the ASIC, bump bonds, PCB and FitPIX box) without recompilation. The polyethylene converter was implemented as a stepped geometry of polyethylene slabs read in from a text file. This implementation allows for the easy testing of many geometries and energy ranges without needing to modify and recompile the Geant4 code. A visualisation of the simulation in progress with the full geometry is shown in Figure 5.3

The simulation outputs several ROOT trees [51]. The first contains details about the reconstructed clusters including the energy, position and type of the initial primary

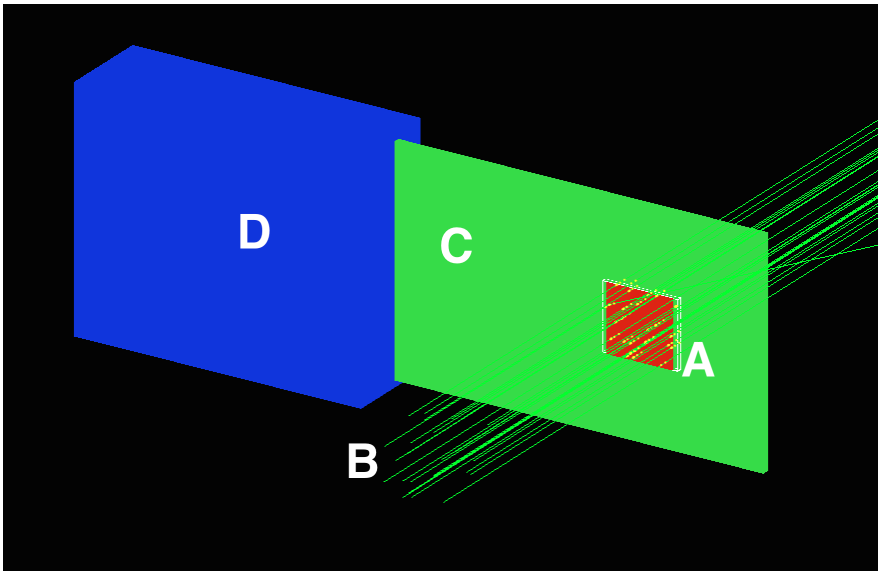

Figure 5.3: Geant 4 visualisation with a modelled Timepix detector (A), PCB (C) and FitPix readout system (D). In this visualisation 10 MeV neutrons (B) are incident on the detector.

particle, the energy deposited by the cluster, the energy of the main depositing particle and the centroid of the cluster. The second tree outputs all energy depositions in the silicon step-wise and event-wise allowing ipso facto inspection of the data. The third tree provides complete details about the polyethylene geometry used.

The resulting trees are then analysed by several different ROOT scripts to produce the plots given in the results section.

5.3 Results of Simulations

For the first set of simulations the response (integral number of reconstructed clusters) was investigated as a function of the cluster thickness for monoenergetic neutrons. We were interested in investigating what the contribution to the count rate would be from interactions of the neutrons with silicon. Figure 5.4 shows the absolute count rates of protons and any other hadronic particle measured in the detector. For simplicity we label these two groups protons and 'hadrons'. With the same energy these particles should be morphologically similar in the detector (blob/track like), but protons represent the signal we want to measure, while other hadrons are the noise. A summary of the absolute number of detected particles for 10^8 incident neutrons is shown in

Figure 5.5, showing that the two dominant detected particles are protons and excited ^{28}Si nuclei. We do not distinguish the particles based on their origin, just what is measured in the simulated detector. Three conclusions are clear here.

- The proton count rate is a strong function of the polyethylene thickness up to a threshold thickness for any given neutron energy. This corresponds to the maximum range of the recoil protons produced in the polyethylene.
- The hadron count rate is independent of the polyethylene thickness. This is because (almost) all of these events originate in the silicon and the neutrons are never significantly attenuated by the polyethylene converter at the thicknesses studied.
- For all three energies studied the hadron (background) count rate exceeds or is similar to the proton (signal) count rate.

Following this we investigated to see if we could use the energy measurement capabilities of the Timepix detector to cut the (n,Si) component based on energy. The energy deposited in an elastic collision depends on the ratio of masses of the colliding particles and the scattering angle θ as shown in equation 5.2.

$$E_R = \frac{4A}{(1+A)^2}\left(1-\cos\theta\right)E_n \tag{5.2}$$

$$E_R|_{\max} = \frac{4A}{(1+A)^2}E_n \tag{5.3}$$

$$E_{\mathrm{Si}}|_{\max} = 0.133E_n \qquad E_{\mathrm{H}}|_{\max} = E_n \tag{5.4}$$

where A is the mass of the scattering nuclei in atomic mass units (for the neutron this is 1), E_n the neutron energy and E_R the energy of the recoil particle. In the maximal case for polyethylene the recoil energy is E_n, in silicon it is $0.133E_n$ when E_n is the neutron energy [3].

Energy spectra for protons and hadrons for 10 MeV neutrons are shown in Figures 5.6 and 5.7. It is clear that the vast majority of the hadronic component is below 200 keV. Therefore we can cut this component simply by imposing a cluster energy cut.

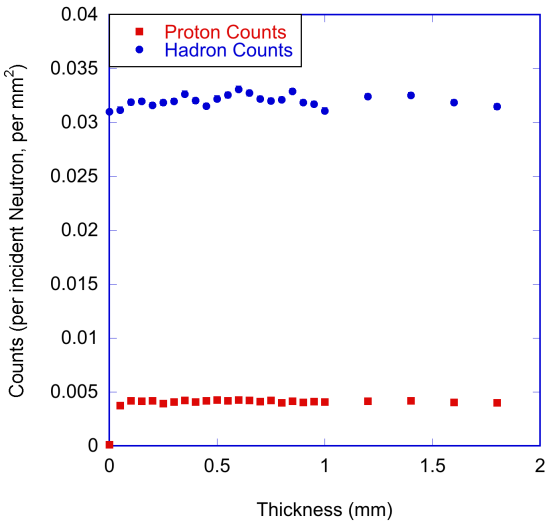

(a) 2 MeV Incident Neutrons

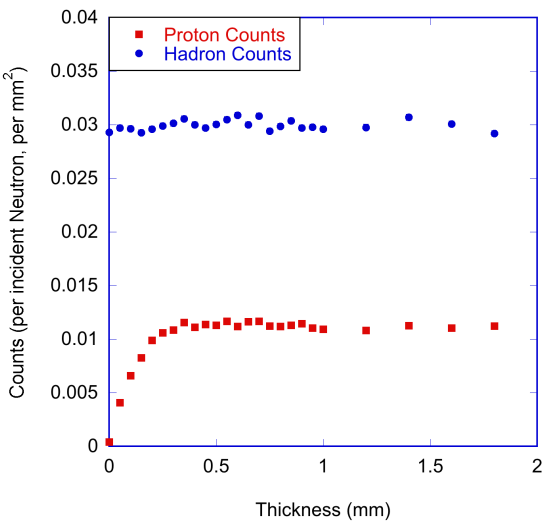

(b) 5 MeV Incident Neutrons

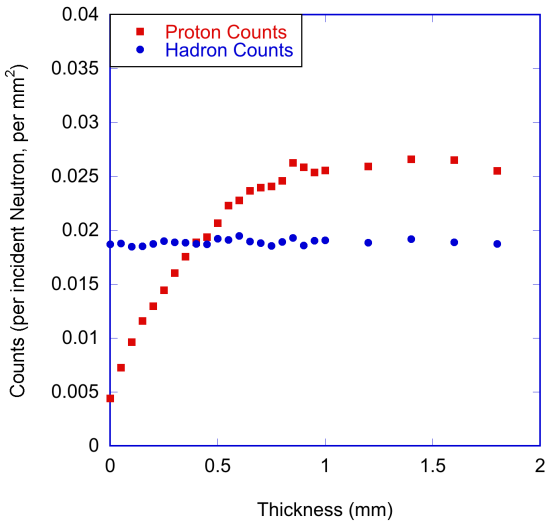

(c) 10 MeV Incident Neutrons

Figure 5.4: Number of protons and 'hadrons' (anything hadronic that was not a proton) detected for 2, 5 and 10 MeV incident neutrons.

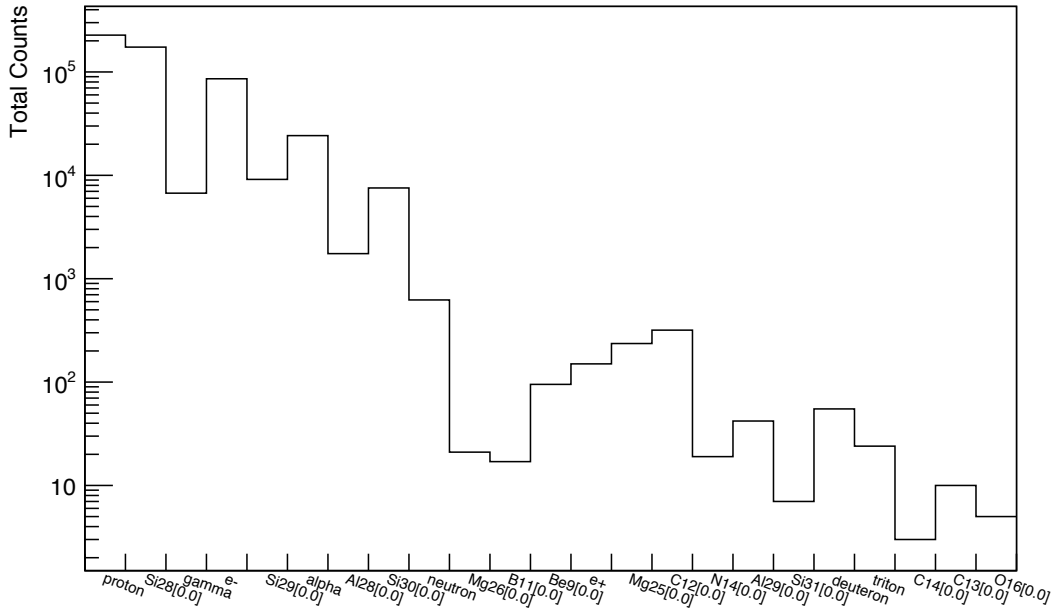

Figure 5.5: Detected/absorbed cluster type in Medipix for 10^8 incident 10 MeV neutrons. The clusters are tagged by the component that deposited the most energy in Geant4. Interactions tagged as photons/neutrons will have deposited a sufficiently small amount of energy to be under the physics cut for secondary production.

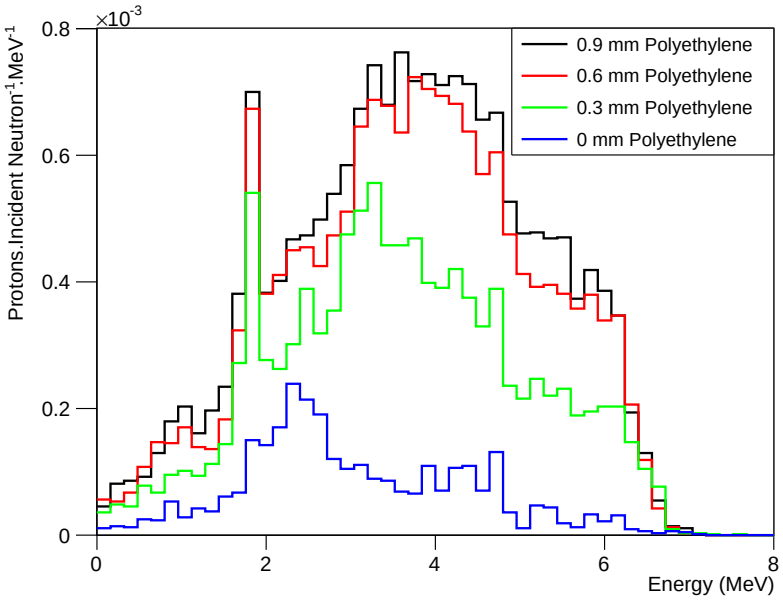

Figure 5.6: Detected/absorbed energy spectrum of protons for 10 MeV incident neutrons, for three different converter thicknesses and for no converter.

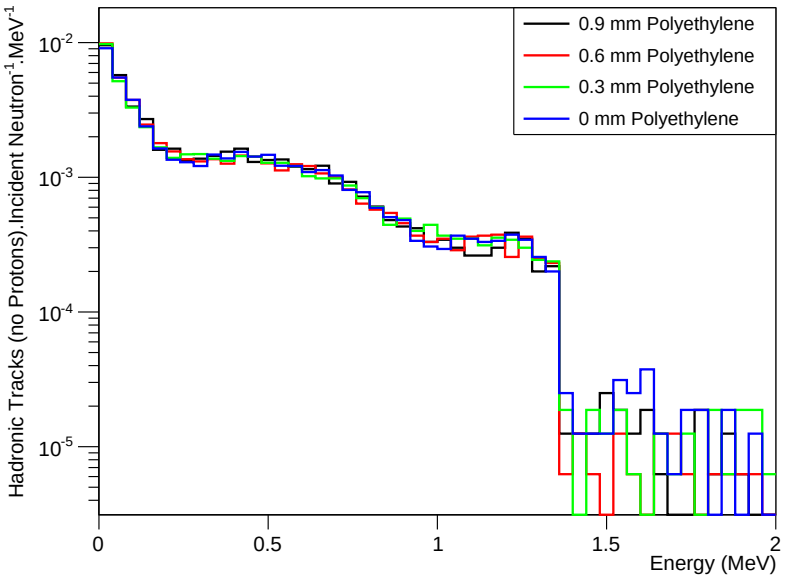

Figure 5.7: Detected/absorbed energy spectrum of 'hadrons' (anything hadronic that was not a proton) for 10 MeV incident neutrons, for three different converter thicknesses and for no converter. The sharp drop at 1.33 MeV corresponds to the maximum energy transferrable to a silicon nucleus

Initially we used a more complicated polyethylene geometry based on the doctoral thesis of M.A.R. Othman [95]. This geometry is shown in Figure 5.8. It consists of six different thicknesses of polyethylene slabs between 10 µm and 1 mm with one uncovered segment in the middle. We simulated this geometry with 50 simulations of 10^8 mono energetic neutrons, varying in energy from 100 keV to 15 MeV.

We then calculated the response of the polyethelene slabs to heavy charged particles with and without a 200 keV cut. The responses are shown in Figure 5.9. It is clear that resonances of the neutrons with silicon dominate the uncut data (as there is no variation with polyethylene thickness), while the response functions are very different for the cut data. Finally we subtract off the counts in the uncovered region from the covered region. This removes the residual response in all regions and would in the case of a charged particle field allow the subtraction of the field as well. These subtracted functions are shown in Figure 5.10.

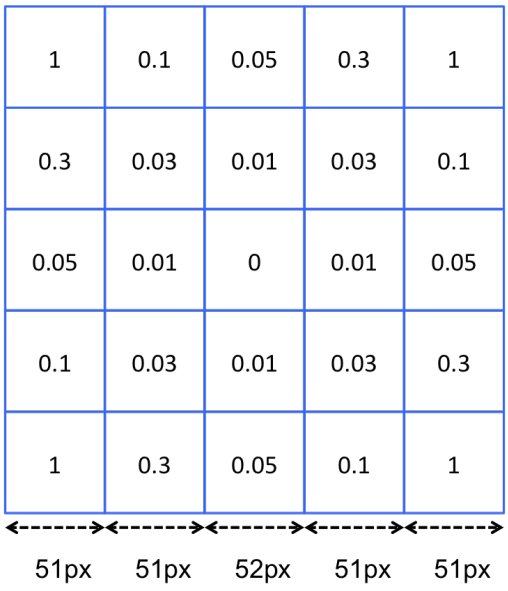

(a) Schematic of Geometry, thicknesses are in mm, 1 Px = 55 µm

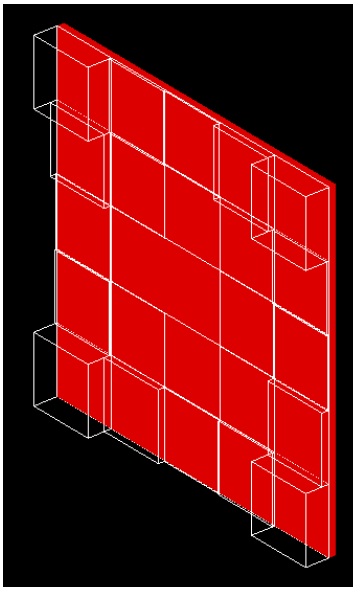

(b) Geant4 Visualisation of Geometry

Figure 5.8: Test geometry used for simulations, based on the Geometry from the thesis of M.A.R Othman. The geometry consists of six thicknesses of polyethylene at 1 mm, 0.3 mm, 0.1 mm, 0.05 mm, 0.03 mm and 0.01 mm and a single uncovered segment in the centre of the detector.

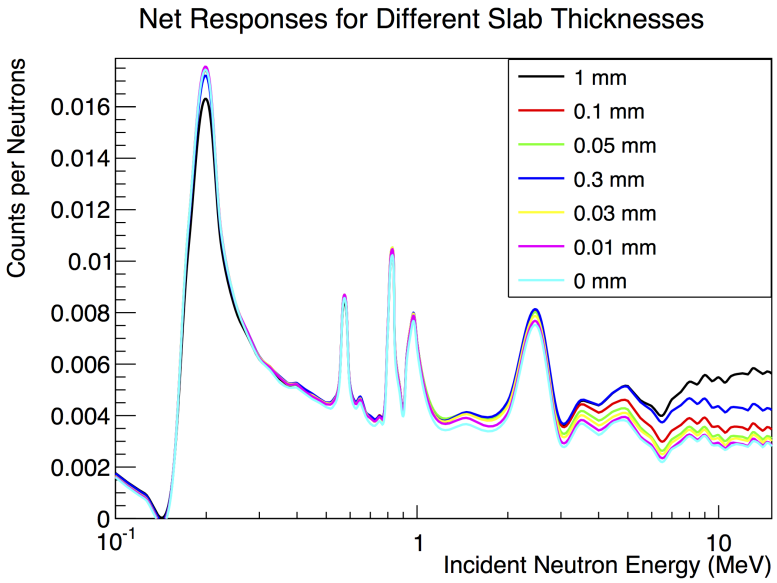

(a) No Cut

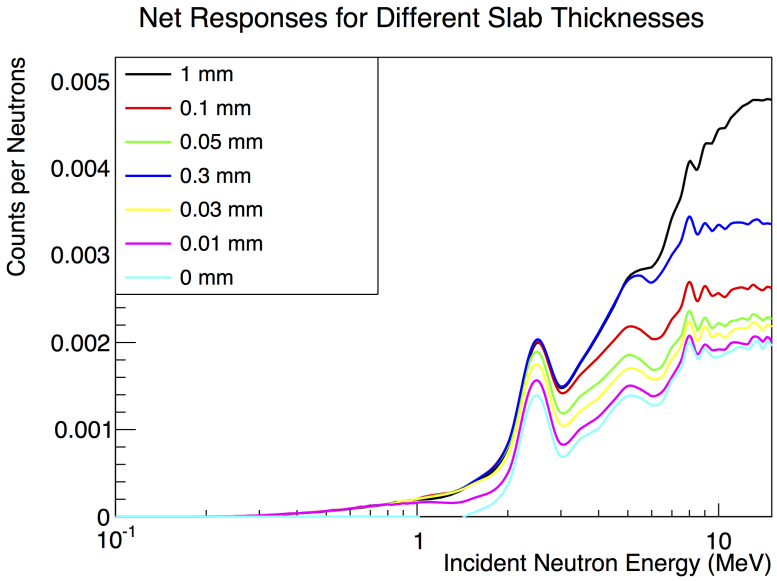

(b) 200 keV Cut

Figure 5.9: Absolute response of the detector to heavy charged particles with and without a 200 keV cut.

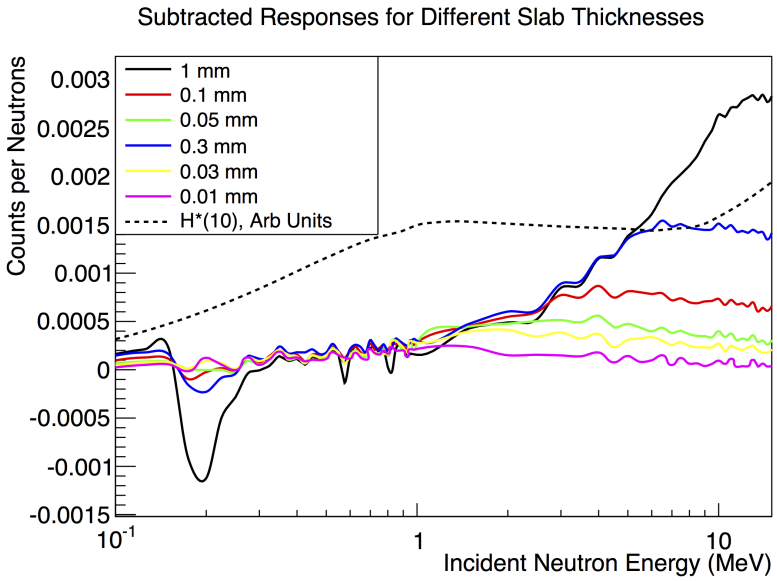

(a) No Cut

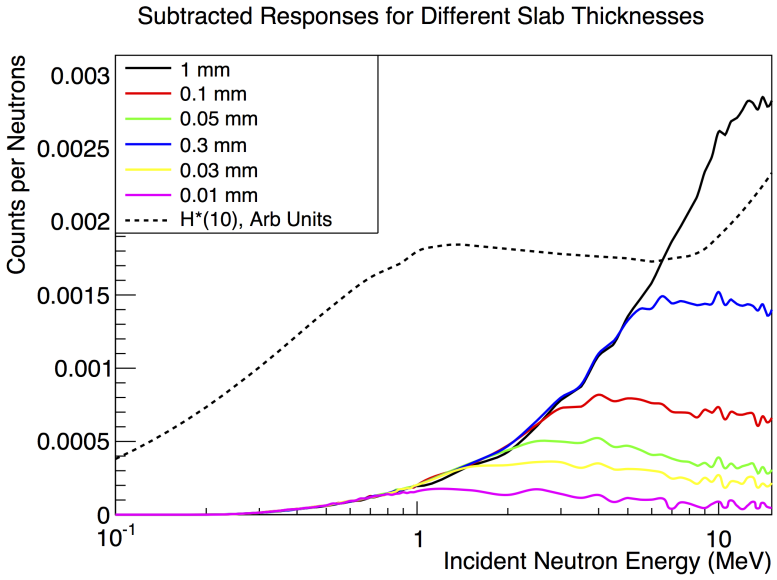

(b) 200 keV Cut

Figure 5.10: Subtracted response of the detector to heavy charged particles with and without a 200 keV cut.

5.4 Optimisation to Produce an Energy Independent Response

The ultimate aim of the optimisation is to find a solution whereby the linear combination of the weighted response functions is the same as that of the H*(10) curve over a range of energies, i.e. that:

$$\sum_i \beta_i R_i(E) \approx \mathrm{H}^*(10)(E) \quad \text{for} \quad E_{\min} \rightarrow E_{\max} \tag{5.5}$$

Where $R_i(E)$ is the response function for a particular slab i of polyethylene and β_i is the weighting coefficient for that slab.

To optimise the geometry we used a simulated annealing algorithm [96]. Simulated annealing is an ideal candidate for complex optimisation problems (which the six dimensional search space of this problem probably does not qualify for), but is easily extensible to arbitrarily complex or curved polyethylene geometries, (which comprise a much higher dimension search space) without suffering a large performance decrease.

The objective with simulated annealing is to minimise some cost function F. The parameters that describe the system are allowed to vary in a semi-random way and if a change reduces the value of F it is accepted. The crux of the algorithm is that some changes that increase the value of F are also allowed, and over time the allowable size of these negative transitions is also reduced. In this way the algorithm touches on all of the search space without needing to exhaustively search through it. This process is similar to that of annealing in the cooling of metals (with the decreasing size of the allowed negative transitions being a surrogate for the temperature), hence the name.

The cost function F for the subtracted response functions R_i is defined as follows:

$$F = \sum_{E_{\min}}^{E_{\max}} \left| \left[\left(\sum_i \beta_i \int_{E_n}^{E_{n+k}} R_i(E) dE \right) - \int_{E_n}^{E_{n+k}} \mathrm{H}^*(10)(E) dE \right] \right| \tag{5.6}$$

This equation looks complicated but the idea behind is straightforward. The data is interpolated using cubic spline interpolation to form a set of continuous curves $R_i(E)$. The integral of these curves over some arbitrary energy range ($E_n \rightarrow E_{n+k}$)

is multiplied by the linear coefficients and summed. This forms the integral of the reconstructed H*(10) function over the region $E_n \rightarrow E_{n+k}$. This is then subtracted from the actual H*(10) function and the absolute value taken. This value will tend to zero for a better match to the H*(10) curve providing the interval k is sufficiently small. Finally these absolute differences are summed over the relevant energy range from $E_{\min} \rightarrow E_{\max}$ to form the cost function F. If the two curves are similar F is small, if they are different F is large.

There are a number of other ways to work with this data, such as optimising residuals around fixed points (as used in least squares) - however the advantage of this method is that it allows comparison of an H*(10) function with Monte Carlo simulations and experimental data which have an arbitrary (and different) number of points. The primary advantage of simulated annealing is that it does not suffer from the curse of dimensionality. An exhaustive search over all the variables in a problem goes as the power of the number of variables. So for an exhaustive search through all configuration for a ten slab geometry will take 10^{10-4} times longer than for a four slab configuration.

We cool this model and perform the optimisation using the classic Metropolis-Hastings algorithm from statistical physics [97].

The results of this optimisation for the subtracted response functions with the 200 keV cut are shown in Figure 5.11. 1000 perturbations were used per slab, per temperature step with 100 temperature steps total in the cooling. The complete optimisation takes about 20 seconds on an Intel Core i7 processor. The six slab solution fits the H*(10) curve well between 1 MeV and 15 MeV. Reducing the number of slabs from six to four as shown in Figure 5.12 provides an almost identical fit to the data, but a reduction to three (Figure 5.13) starts to degrade the range of the energy independent response. The β_i values for 6,5,4 and 3 slab configurations are shown in Table 5.2. Note that some of the β_i values are negative, i.e. the contribution is subtracted from the overall response. While it may seem odd or unphysical to have a negative response, it is important to bear in the mind that this is the result of the fitting procedure, which aims for the composite response function to match the H*(10) dose fluence response function. This means that the response of any one slab is unimportant, instead it is the complete response of the converter that matters.

The response for this optimised configuration in counts per mSv is shown in figure 5.14. The response is 405 ± 30 counts per mSv between 1.5 MeV and 15 MeV, or

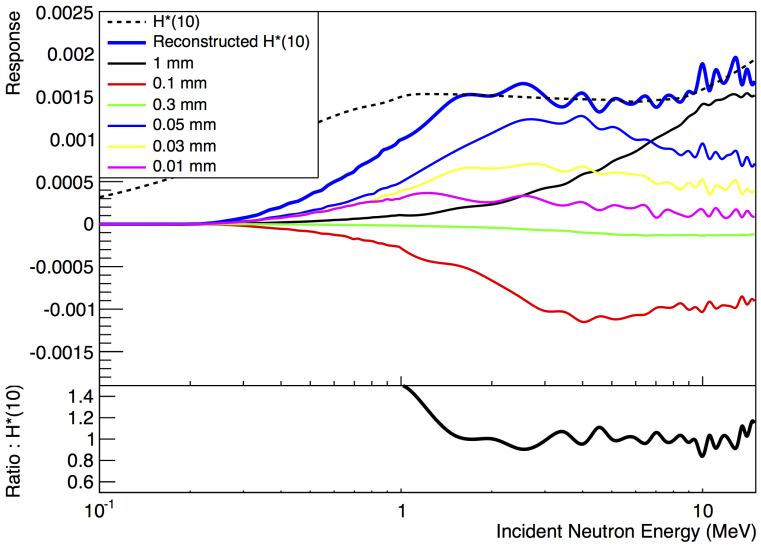

Figure 5.11: Optimised response compared to H*(10). There is a good fit between 1 MeV and 15 MeV to the H*(10) curve.

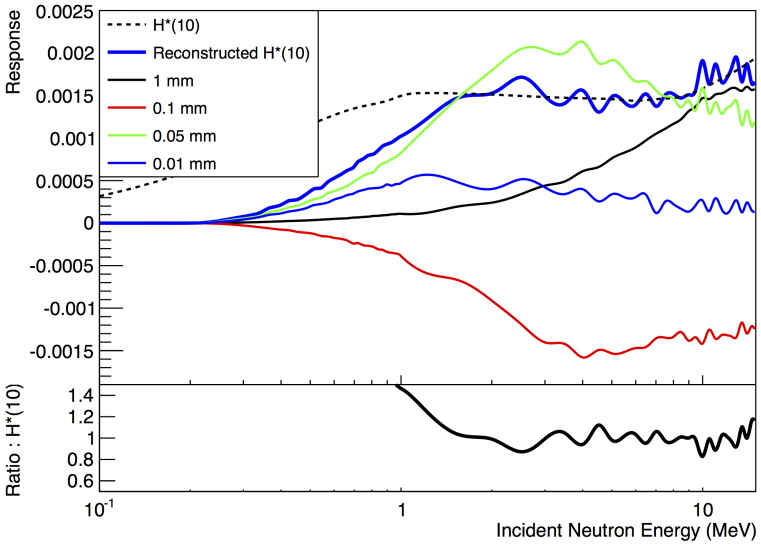

Figure 5.12: Optimised response with 4 slabs compared to H*(10). The fit is as good as with the 6 slab configuration used in Figure 5.11.

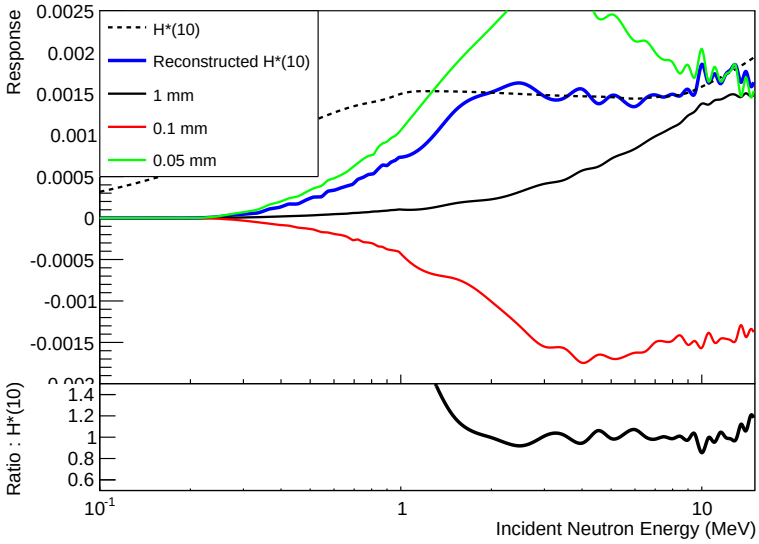

Figure 5.13: Optimised response with 3 slabs compared to H*(10). The performance of the fit starts to degrade in comparison to the 6 and 4 slab configurations used in Figures 5.11 and 5.12.

Thickness	6 Slab	5 Slab	4 Slab	3 Slab
0.01 mm	2.26	2.38	2.95	5.47
0.03 mm	1.50	1.37	-	-
0.05 mm	2.81	3.00	4.10	0.753
0.1 mm	-1.58	-1.74	-1.94	-
0.3 mm	-0.0650	-	-	-
1 mm	0.552	0.545	0.563	0.415

Table 5.2: Normalised scaling coefficients (β_i) for different thicknesses and configurations of converter.

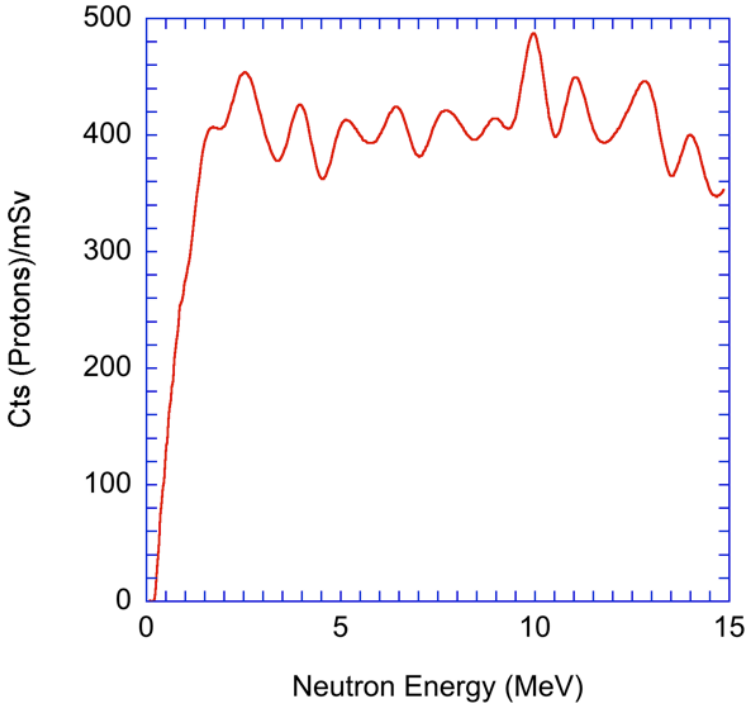

Figure 5.14: Response (counts/mSv) for the optimised converter design. The average counts are 405 ± 30 from 1 MeV to 15 MeV.

2.5 µSv per count.

5.5 Experimental Geometry and 3D Printing of Converters

Following the optimisation in the previous section a new design of converter was conceived for use as an experimental prototype. The essential idea is to scale the active areas in proportion to the β_i values calculated, so that with the new converter geometry the β_i values are close to 1. In addition the minimum converter thickness used was 0.03 mm because 0.01 mm thick polyethylene is very difficult to obtain or work with. Figure 5.15 shows this optimal geometry complete with a 10 pixel wide uncovered region at the edge of the detector.

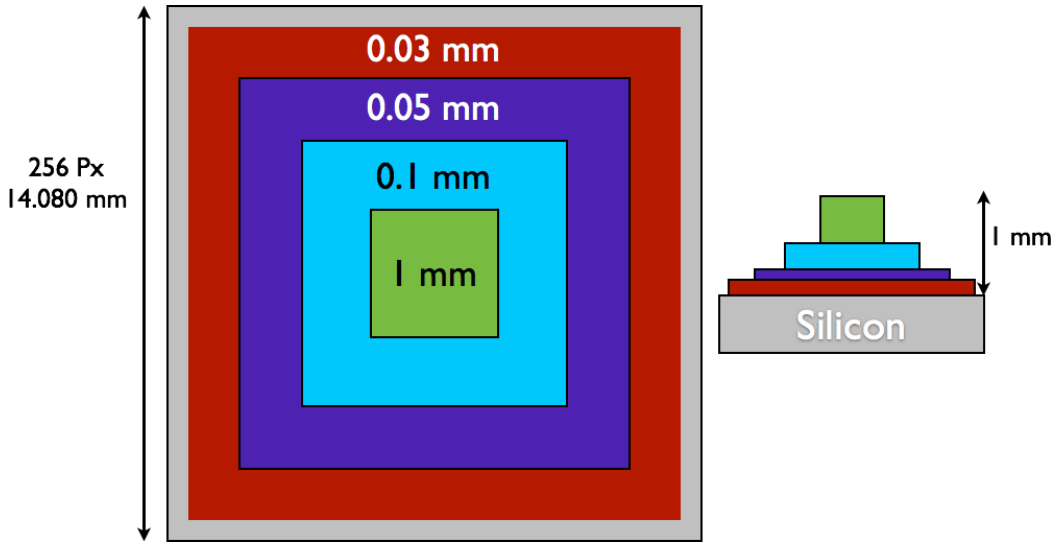

Thickness	β	Scaled Area (%)	Width (Pixels)	Width (mm)	Δ Thickness
0 mm (None)	-	15 %	256	14.08 mm	0 mm
0.03 mm	2.86	31.6 %	236	12.98 mm	0.03 mm
0.05 mm	2.50	28.9 %	187	10.29 mm	0.02 mm
0.1 mm	-1.65	18.7 %	127	6.99 mm	0.05 mm
1 mm	0.508	5.7 %	61	3.36 mm	0.9 mm

Figure 5.15: Configuration for plastic slabs in an optimised geometry. The slabs sit on top of each other as shown in the top figure, the bottom table details the exact geometric characteristics of the slabs. Included is a 10 pixel dead zone for measuring background at the edge of the detector.

Following the design of the optimised geometry a 3D printed prototype was produced. The 3D printed prototype was made from Visijet® Crystal, EX 200 material. 3D printing the converter comes with several compromises. The material composition is proprietary and the minimum thickness that can be used is 0.064 mm, however the ability to quickly produce and iterate over designs is very useful. Initial designs attempted to mimic the optimised designs shown in figure 5.15 with supporting bars in order to mount the converter on the Timepix detector. Such designs suffered from warping however and an optimised design was conceived with the help of Dr. M. Weaver which essentially inverts the original design. A solidworks plan of the new converter design is shown in figure 5.16. Photographs of both the failed and optimised converter designs are shown in figure 5.17. An x-ray image of the converter is shown in figure 5.18 and is used to identify the converter zones for the rest of this section.

The Visijet crystal material used is of somewhat uncertain composition. An estimate based on the MSDS data [98] and by assuming that the remaining material is nylon or nylon like [99] gives a hydrogen fraction of 30% to 50% by number of atoms.

5.6 Experimental Converter Validation with Time of Flight Neutrons

In this section neutrons produced at a Time of Flight facility are used to validate the detector concept. The essential idea is that the energy of a neutron produced by a TOF facility can be determined by measuring its time of flight which can be measured by a Timepix detector operating in TOA mode. From this the response (i.e. number of counts) of each segment under the 3D converter can be measured as a function of energy, directly validating the converter concept. The responses measured at NTOF should be different to the simulated responses as both the material and converter design differ from those simulated.

5.6.1 The NTOF Facility

NTOF [100] is a neutron Time of Flight (TOF) facility at CERN. At NTOF a broad spectrum of neutrons is generated by firing a short pulse of 7×10^{12} protons at $20\,\mathrm{GeV}\,c^{-1}$ from the CERN Proton Synchrotron into a lead target. The neutrons are then sent down a 185 m long tunnel where they separate in time following their

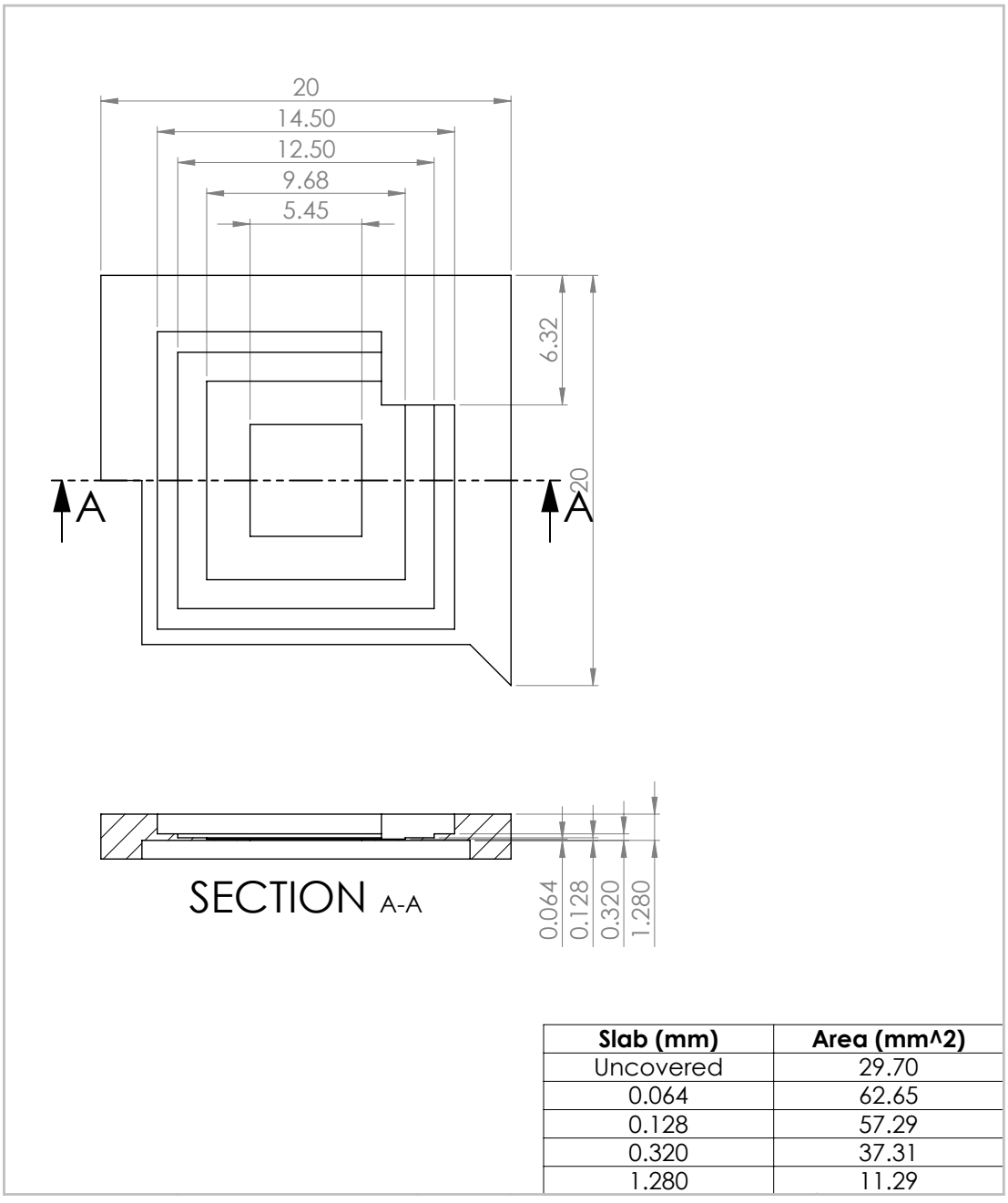

Slab (mm)	Area (mm^2)
Uncovered	29.70
0.064	62.65
0.128	57.29
0.320	37.31
1.280	11.29

Figure 5.16: Solidworks plan of converter for 3D printing. Figure courtesy M. Weaver.

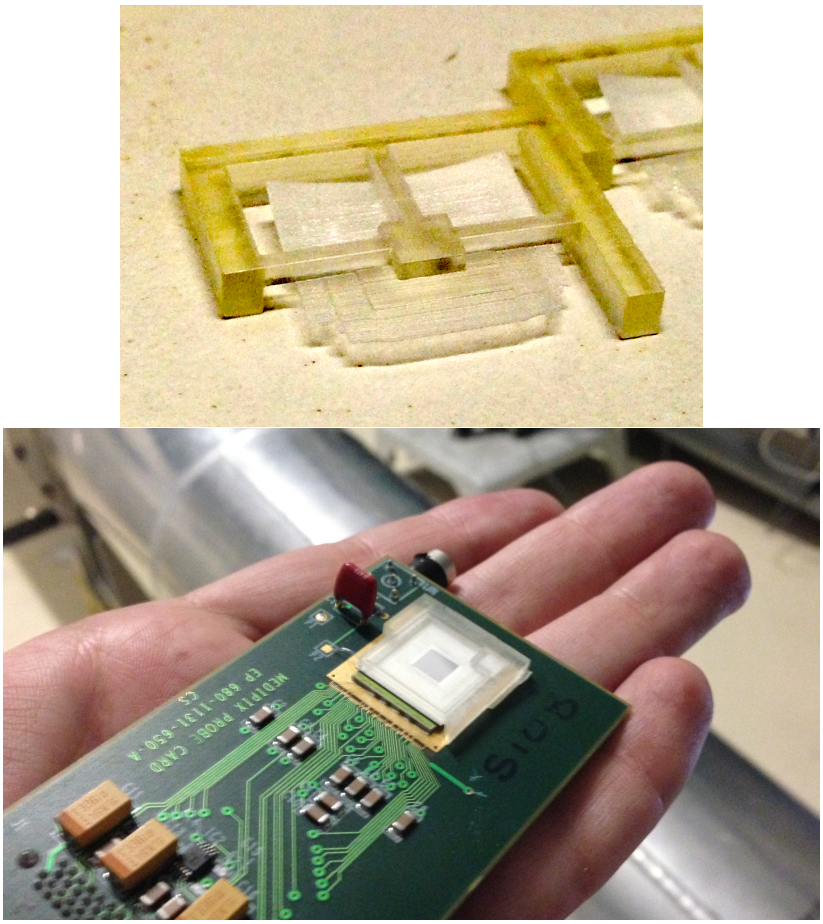

Figure 5.17: Photographs of 3D printed converters. Top - the original design based on figure 5.15 shows warping around the thinnest sections of the converter. Bottom - modified design mounted on Timepix detector.

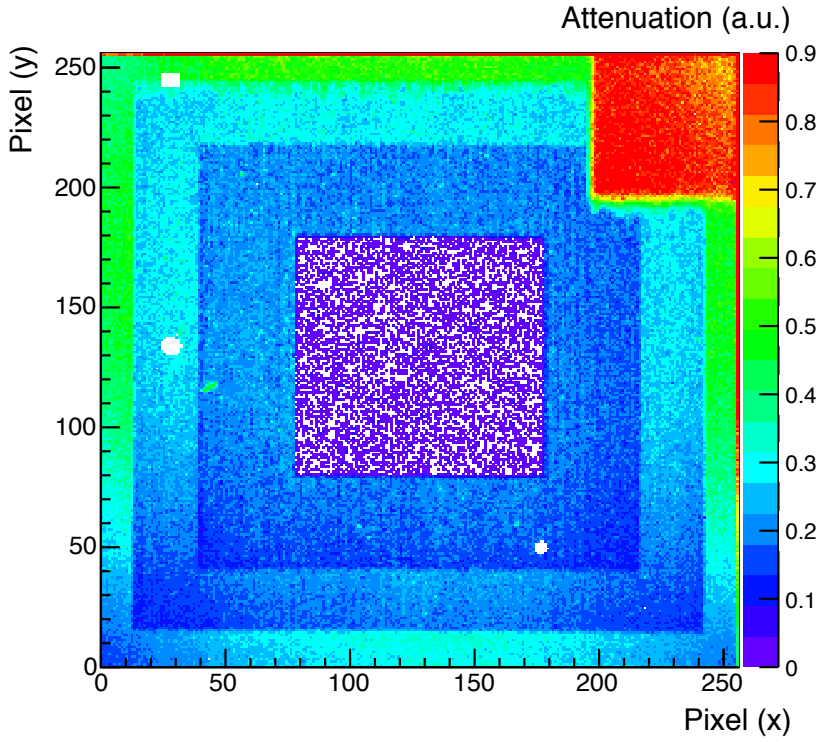

Figure 5.18: Flat field corrected X-ray radiograph with ^{55}Fe photons.

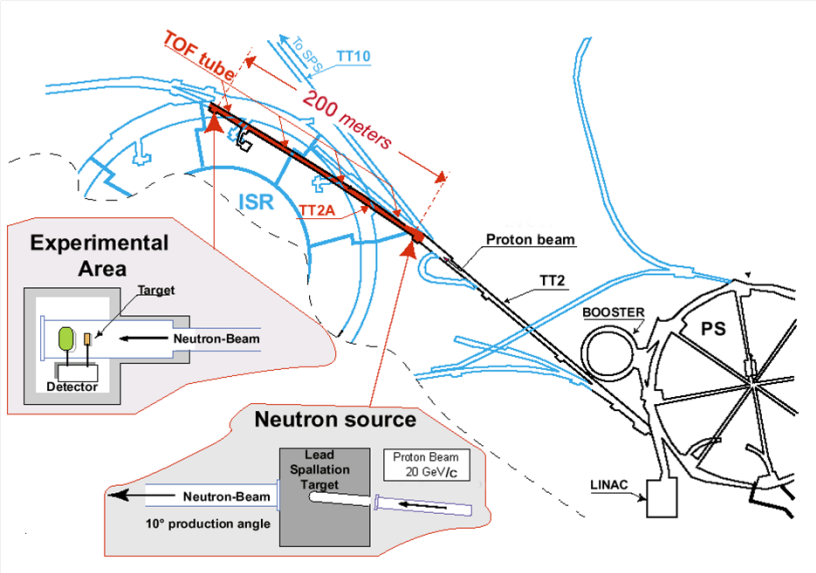

Figure 5.19: Plan of the NTOF Facility at CERN.

kinetic energies. Figure 5.19 shows a schematic of the NTOF facility and figure 5.20 shows the neutron spectrum generated at NTOF.

The energy of a neutron E_n and its time of flight T across a distance D are related by the following expressions:

$$E_n = m_n \left(\sqrt{\frac{1}{1-\beta^2}} - 1 \right) \qquad \beta = \frac{v}{c} = \frac{D}{Tc} \tag{5.7}$$

Where m_n is the neutron mass ($939.565\,\mathrm{MeV}/c^2$). Figure 5.21 shows the time of flight of neutrons as a function of their kinetic energy for the 185 m throw distance at NTOF.

This means that in principle by measuring the time of arrival of an interaction the energy of the neutron that created it can be discerned, if one has some way of measuring the time of neutron production.

5.6.2 Data Analysis and Clustering

A clustering algorithm similar to the one used in section 3.4.2 is used to separate the clusters following the method of Bergmann [57]. The primary difference between this clustering algorithm and the one described in section 3.4.2 is that because the

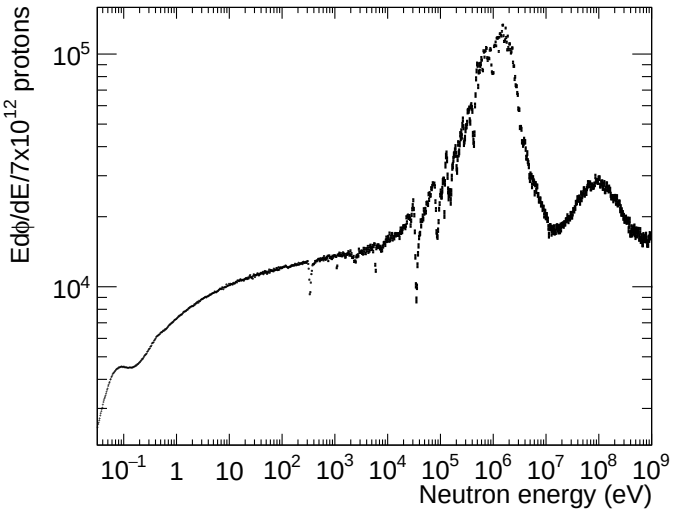

Figure 5.20: Neutron Spectrum generated at NTOF [2].

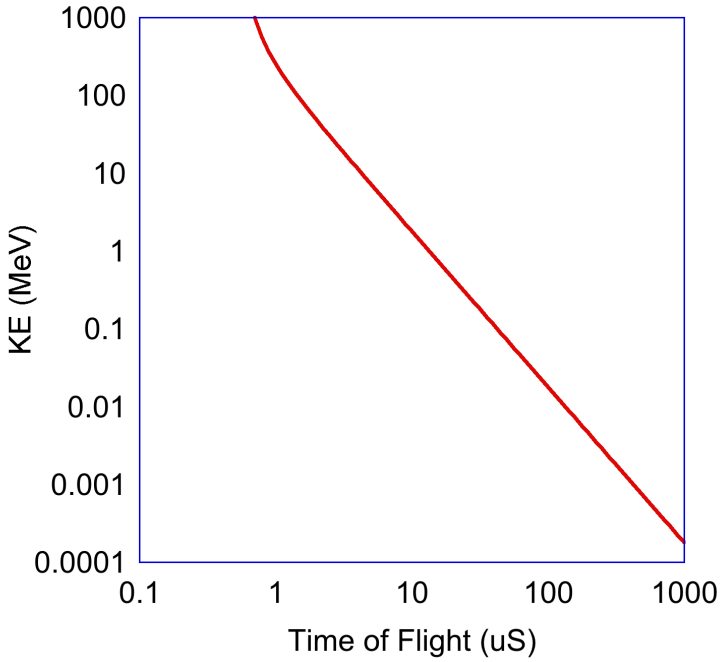

Figure 5.21: Time of flight of neutrons as a function of neutron kinetic energy at NTOF (185 m throw length).

detector is operated in TOA mode the time of arrival (i.e in the counts in the pixel) can be used to discriminate overlapping clusters. In this case an 8-fold flood fill search is performed with the additional constraint that any new pixels added to the cluster must be within 60 ns (i.e. 3 TOA counts at 48 MHz clock frequency) of the existing pixels in the cluster.

There are four used clustering categories in comparison to the six used earlier:

- Dots - As in section 3.4.2. Low energy point like interactions.
- Tracks - Heavy Tracks. High energy, long range interactions. Faster recoil protons and similar.
- Blobs - Heavy and Medium Blobs. High energy, short range interactions.
- Curly - Straight and Light tracks

The reason for the simplification of the clustering algorithm is to approximately replicate the conditions used in the simulation - i.e. the separation of 'noisy' electron tracks and tracks with $E < 200\,\text{keV}$ (dots), see figure 3.13 and 'signal' - i.e. proton recoil tracks. As the clustering algorithm used does not exactly match that used in the simulation the results should not exactly match the simulation response. A sample frame gathered at NTOF is shown in figure 5.22.

The TOA value of each cluster can then be used to measure the energy of the incident neutron that produced it providing that the start time of the neutron pulse is known. At NTOF an external trigger is provided at the start of each pulse, but this trigger is associated with a 2 µs jitter which introduces a considerable energy error, especially for fast neutrons with $E > 1\,\text{MeV}$. This measurement of arrival time can be further refined by looking for the 'photon flash' which is associated with production of photons in the lead target which travel with velocity c to the Timepix detector. This is done by searching through the clusters in each frame and looking for the earliest TOA bin with a threshold number of photons (normally 10). The trigger jitter of 2 µs can be measured by plotting this value and is shown in figure 5.23.

5.6.3 TOA and Energy Spectra

The resultant TOA spectrum is shown in figure 5.24. The absolute response spectrum can be obtained by normalising to the energy bin width and the NTOF spectrum. Ab-

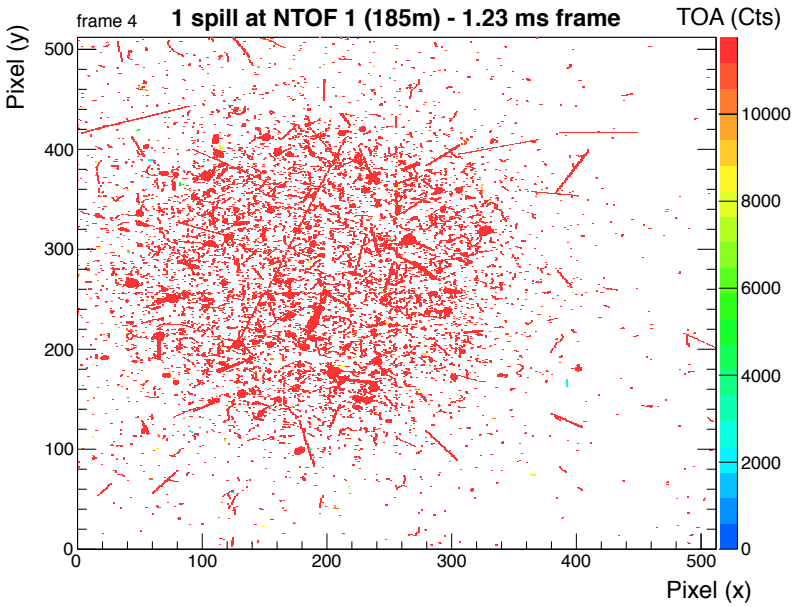

Figure 5.22: Sample frame measured at NTOF (measured with a quad Timepix detector in order to show the whole beam spot).

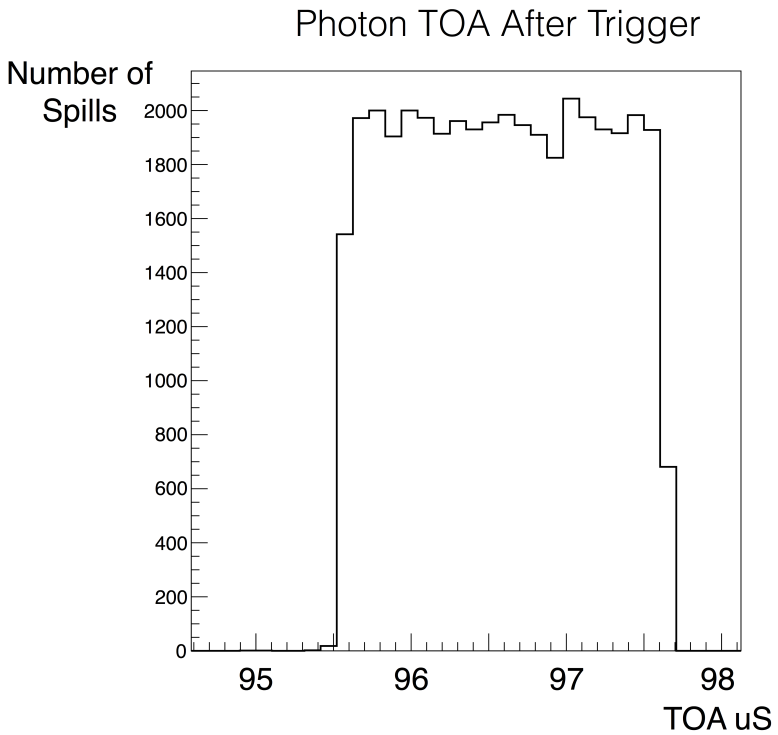

Figure 5.23: Trigger jitter measured at NTOF

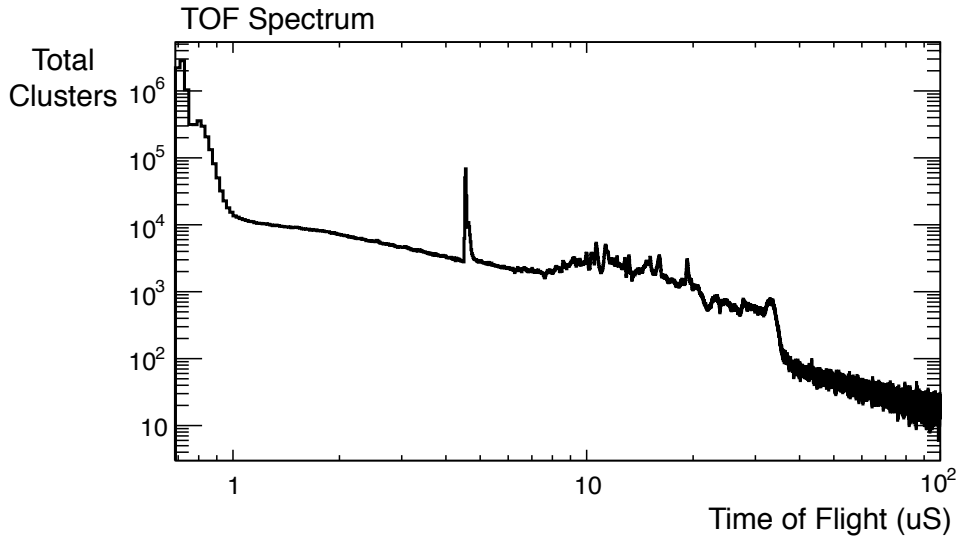

Figure 5.24: TOA Spectrum measured by a Timepix detector at NTOF.

solute response spectra are shown both with and without the converter in figure 5.25. The spectrum shown in figure 5.25 is split into different cluster components. The dot spectrum in the fast neutron energy region displays characteristic structure which corresponds to neutron elastic scattering in silicon [57].

5.6.4 Calculation of response curves

The primary complication in the calculation of response curves is that the NTOF beam is inhomogeneous, and that this inhomogeneity varies with energy. Measured beam profiles at NTOF for 4 different energy regions using a quad Timepix detector are shown in figure 5.26. These beam profiles were used for validation and alignment of the NTOF neutron beam, and for the installation of a new laser alignment system at NTOF.

As the dot like clusters are primarily from elastic scattering of neutrons off silicon above 200 keV and the neutron beam is not significantly attenuated by the converter these elastic scatters can be used to derive a flat field like correction for the beam where the number of signal hits at a given position is scaled by the inverse of the number of dots at that position. This correction procedure is shown in figure 5.27.

Subtracted normalised response curves (from Blob and Track like clusters) are shown in figure 5.28. Optimised responses up to 15 MeV are shown in figure 5.29, and up to 100 MeV is shown in figure 5.30. In general the reconstructed responses work

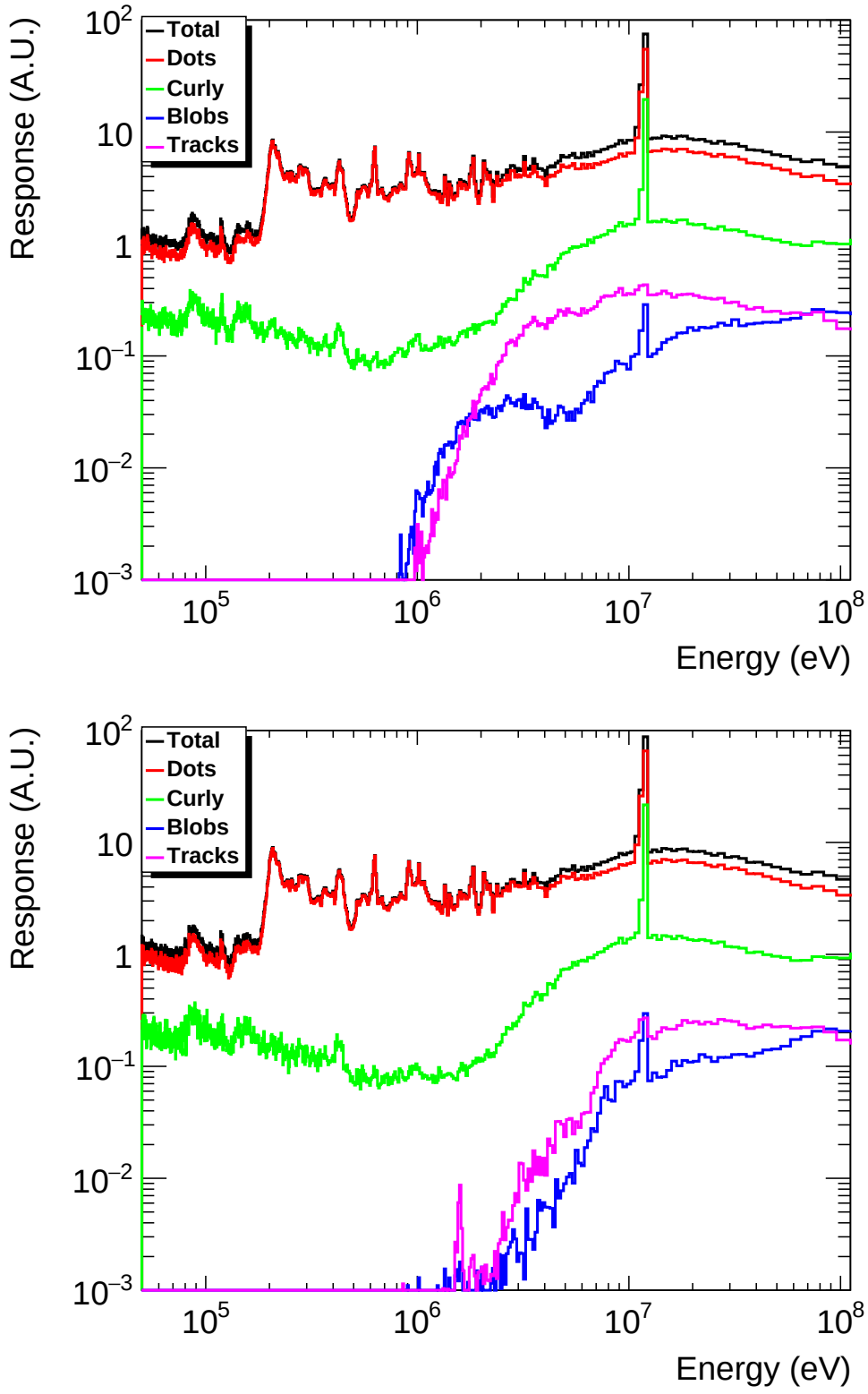

Figure 5.25: Response spectrum of a Timepix detector with (top) and without (bottom) converter by cluster type.

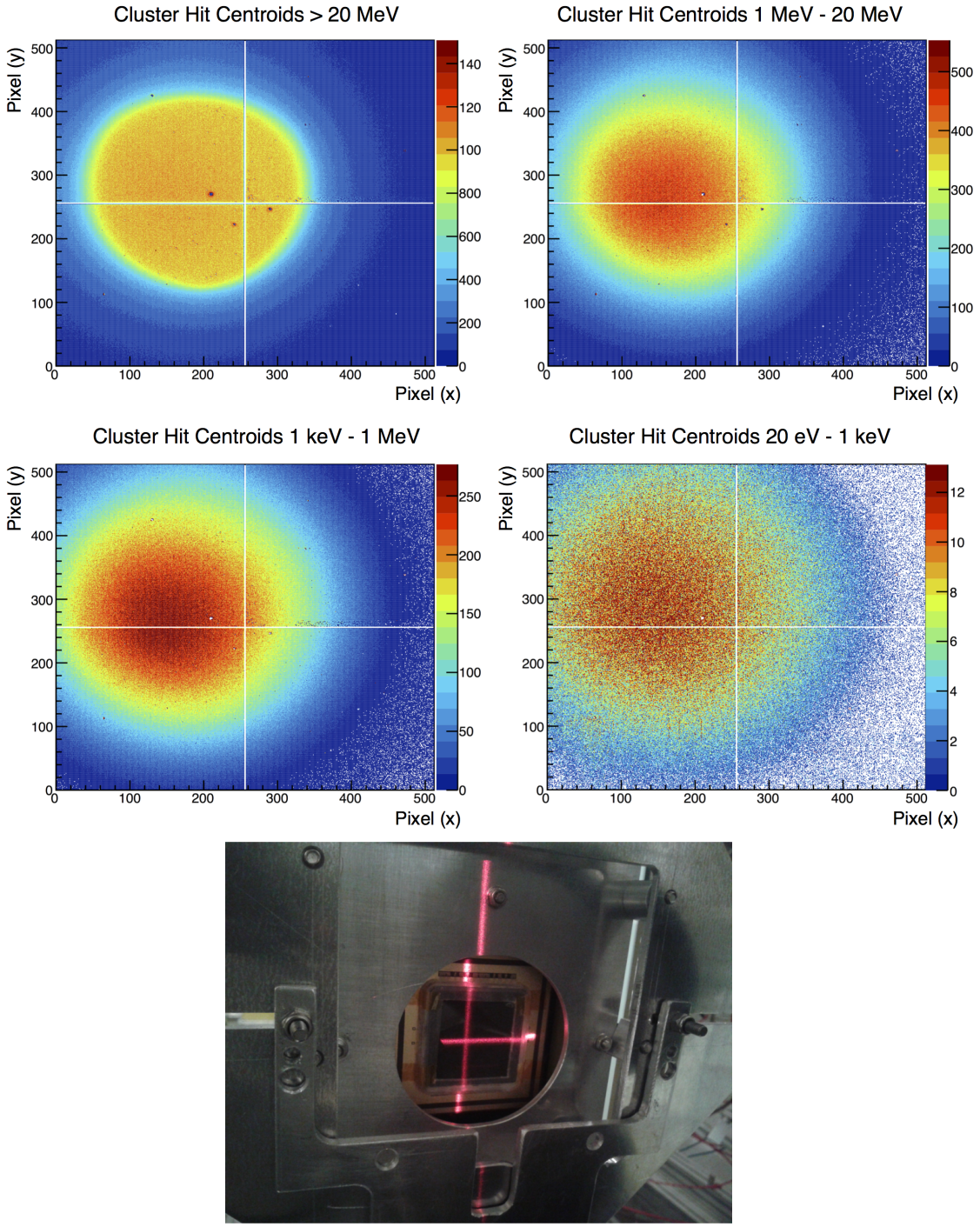

Figure 5.26: Top - Beam profiles as a function of energy measured with a Quad Timepix detector at NTOF. The varying profile of the beam is due to different collimators used to shape the beam in different energy ranges. Bottom - Resultant laser alignment system installed at NTOF.

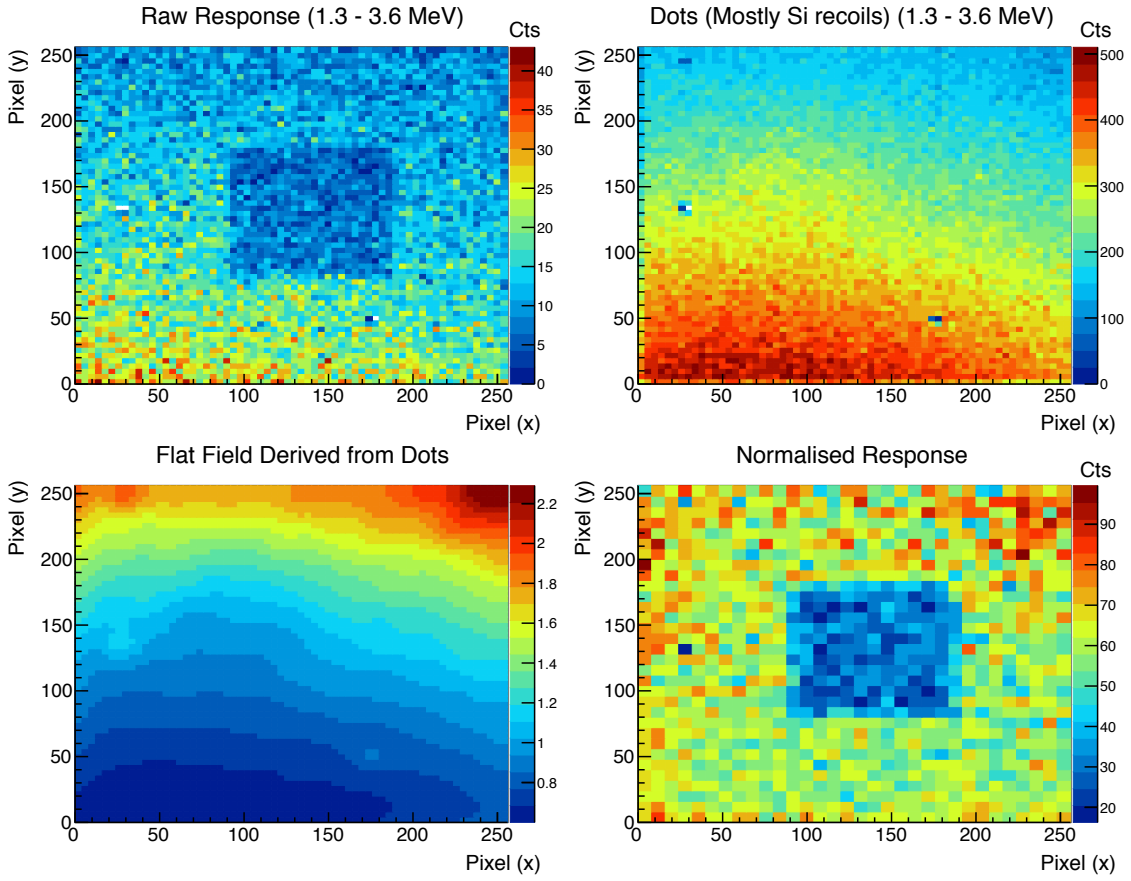

Figure 5.27: Flat field correction at NTOF, (top left) - the measured response, (top right) measured dot response, (bottom left) resultant flat field, formed by smoothing the dot response, calculating its inverse and normalising so the average per pixel value is 1, (bottom right) corrected response.

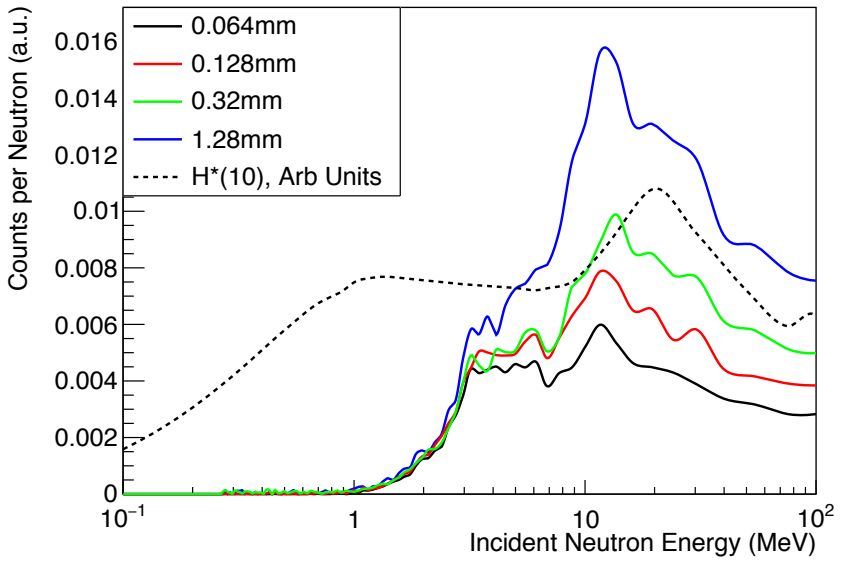

Figure 5.28: Subtracted response functions for different 3D printer material thicknesses as a function of neutron energy.

well for high energy parts of the curve but less well for low energy parts. This could be because the clustering algorithm does not classify tracks and blobs as low energy protons and that the thinnest segment of the converter is thicker than the optimised design. Future characterisation of this converter should focus on validating the concept at standard neutron sources.

5.7 Conclusions and Future Work

Geant4 simulations of a neutron dosimeter based on several different thicknesses of polyethylene were carried out. A realistic simulation was carried out of the detector and geometry which was guided by experimental experience with the Timepix detector. Optimisation of the response functions found that six thicknesses of polyethylene is unnecessary and that four can provide an energy independent response from 1 to 15 MeV. An experimental prototype was designed and manufactured using 3D printing. Characterisation of the experimental converter was performed by operating the Timepix detector in TOA mode at the N_TOF neutron time of flight facility at CERN. The experimental prototype demonstrated energy independence from 3 MeV to 100 MeV. Further work could focus on providing an absolute calibration of this converter to dose rate using a calibrated neutron source and investigating the background rejection of

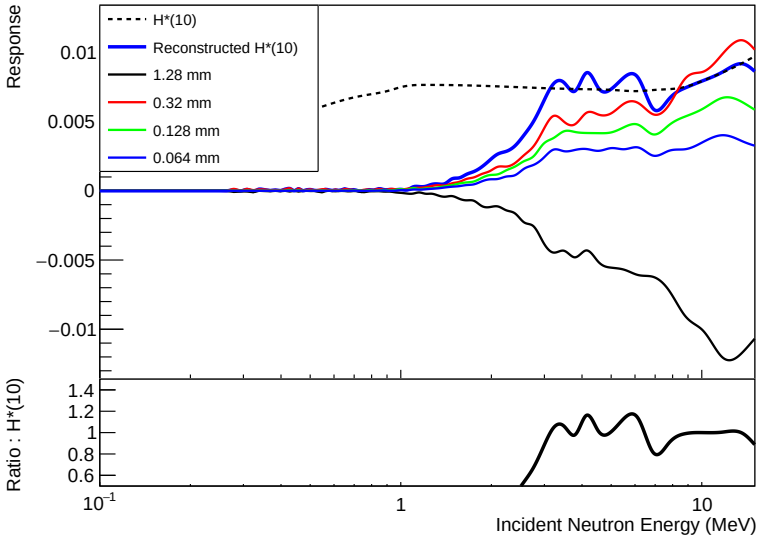

Figure 5.29: Optimised response functions for different 3D printer material thicknesses as a function of neutron energy up to 15 MeV.

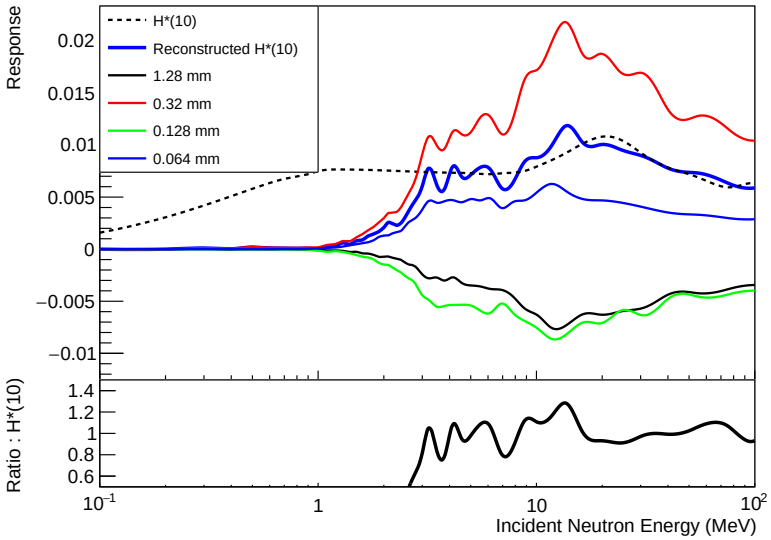

Figure 5.30: Optimised response functions for different 3D printer material thicknesses as a function of neutron energy up to 100 MeV.

photons and charged particles offered by the uncovered region.

Chapter 6

The GEMPix

Most of the material in this chapter was published as S.P.George, F. Murtas et al, *Particle tracking with a Timepix based triple GEM detector*. *JINST* **10** (2015), P11003, http://dx.doi.org/10.1088/1748-0221/10/11/P11003

This chapter focuses on using a Timepix ASIC (i.e. without attached sensor) to read out a sensitive gas volume, specifically a triple Gas Electron Multiplier (GEM) foil assembly. We have called this detector the 'GEMPix'.

6.1 Introduction

The Timepix ASIC [101] was originally developed as a read out system for gas detectors in the framework of the EUDET EU project. The advantages of using a highly pixellated ASIC to read out gas detectors are obvious, mainly in regards to spatial resolution and number of read out channels. Most other gas detector systems use much larger pads to collect charge. There is no formalised difference between a 'pad' and a 'pixel', but pixels tend to be sub-millimetre sized, regularly spaced on a grid and numerous, while pads are generally larger, can have a much more exotic layouts depending on the application and in general a detector will feature at most a few hundred. In a pad configuration the read out and signal processing electronics are typically external to the detector at a considerable increase in cost and size, especially for detectors with a 'large' number of pads (> 100). It is clear that using a Timepix can offer a several orders of magnitude improvement in the pad size (smaller) and number of read out channels (larger) with a much smaller overall detector volume once read

out electronics have been taken into account. The main tradeoff with such a device is the number of electrons that need to be generated to create a signal which is over the Timepix threshold (some $>1000\,/(55\mu\mathrm{m})^2$), which requires some form of external amplification. The concept for gas pixel detectors has been around for several years [102] and was first developed by Bellazzini et al [103] as an X-Ray polarimeter using a custom ASIC [104] for x-ray astronomy [105, 106]. Other examples include the GRIDPIX detector designed for high energy physics applications[107], however sparks and discharges have proven to be persistent problems for these devices. Thanks to a specially designed High Voltage power supply (HVGEM, [108]) and a carefully designed GEM electrode layout, the GEMPix demonstrates good reliability and discharge resistance.

6.2 Physics of Detection in Gases

The basic physics of detection in gases is qualitatively similar to the physics of detection in semiconductors. An ionizing particle travels through a gaseous medium creating ionizations along its path. This ionization typically produces a free electron and a charged ion. The average value required to produce an ion-hole pair W is typically around 25 eV to 35 eV. This value is higher than the first ionization potential for many gases (≈ 15 eV) and this is because an incident particle can lose energy by other mechanisms such as atomic excitation. A remarkable feature of W is that is largely independent of the stopping power of the radiation and varies only slightly (at most a factor of 2) among different gas mixtures.

The resultant ions and electrons are swept out by an electric field, in the case of a position sensitive detector this field is typically called a drift field. Electrons will accelerate due to the drift field until they scatter off a gas molecule. The combination of these two effects causes the electron drift velocity to be a nonlinear function of the applied drift field (see figure 6.1). This scattering also causes diffusion which follows the classical diffusion relation,

$$\sigma = \sqrt{2Dt} \tag{6.1}$$

where σ is the standard deviation of the width of the charge cloud, D the diffusion coefficient and t the drift time. As with the drift velocity D is also a function of the

applied drift field. D is typically split into lateral and transverse components relative to the drift field (following the symmetry of the electron acceleration).

6.2.1 Avalanche Multiplication

An electron avalanche can occur if an electron is accelerated sufficiently that it has enough energy to ionize a gas molecule in a collision. The created secondary electron in turn is accelerated and can create more electron-ion pairs in a continuing cascade. This process is called a *Townsend Avalanche*. The number of electrons created along an infinitesimal path length $\frac{dn}{dx}$ is then the number of electrons multiplied by the number of additional electrons created per unit path length α,

$$\frac{dn}{dx} = \alpha n \tag{6.2}$$

α is called the Townsend coefficient. Assuming that α is not a function of position (i.e the electric field strength is constant) then equation 6.2 can be solved to give

$$n(x) = n(0)e^{\alpha x} \tag{6.3}$$

i.e. the multiplication is the exponential of the drift length. Because there is a threshold energy that an electron must obtain in order to create a second electron, α is zero valued for small electric fields. Beyond a threshold value α is a strongly increasing function of the electric field (see figure 6.1). In order for the read out to be proportional to the input charge the normal strategy used is to somehow keep the distance over which the avalanche propagates fixed. In proportional counters this is done using a cylindrical geometry with a wire running through the middle. Here the electric field falls off from the centre as r^{-1} and avalanche multiplication is only possible in a small central region. The remaining volume of the detector acts as a region in which charge is drifted into the avalanche region, but not multiplied. The charge pulse is then read out from the wire. In wire chambers (or Multi-Wire Proportional Chambers) instead of a single wire, a grid of many are used for a similar effect creating a 2 dimensional position sensitive avalanche detector which can be extended to 3 dimensions by precisely measuring the pulse timing. The wire chamber

was an innovation for which Georges Charpak was awarded the Nobel Prize in 1992.

It is clear that the spatial resolution of a wire chamber is limited by the spacing of the wires. Micropattern gas detectors evolved out of a need to manufacture avalanche detectors with a higher spatial resolution (highly granular wire chambers are difficult to manufacture) taking advantage of manufacturing techniques from the microelectronics industry. The salient feature of GEM foils [109] and other micropattern detectors such as Micromegas is that the spacing between the anode and cathode that generates the electric field is very small. In this way very large electric fields with large Townsend Coefficients can be generated with relatively modest input voltages, and such fields are confined to a well defined, small spatial volume in comparison to the drift region.

The exact choice of drift gas mixture used in an avalanche detector depends on the needs of the experiment - normally the amount of amplification one wishes to obtain for a given applied electric field (i.e. the Townsend coefficient) and the amount of diffusion that is tolerable. At a minimum a drift gas will consist of a gas which provides a process for gas amplification and has electron lifetimes long enough to sustain the propagation of a travelling electron cloud. Often an organic gas will be added that can add a quenching effect to prevent sparks and discharges. Typically in the following text the drift gas used is Ar:CO_2:CF_4 in a ratio of 45:15:40 which was developed for the LHCb collaboration [110]. Figure 6.1 shows values for the drift velocity, diffusion coefficients and the Townsend coefficent as a function of the applied electric field for Ar:CO_2 :CF_4 in a 45:15:40 ratio. These values were computed with Magboltz [111] by Fillippo Resnati at CERN.

Finally it should be noted that the physics of position sensitive gas detectors is an extensive topic, the slimmest overview of which has been presented here. The interested reader is directed to [3, 112] as a starting point.

6.3 GEM Technology, a Brief Overview

It is clear that the number of electrons N produced by the intrinsic ionisation in the gas is rather low, $N \approx 240$ for a 6 keV photons. As the electrons travel through the drift volume they also diffuse serving to further spread the signal. As approximately 1000 electrons are needed to trigger a single Timepix pixel some form of external amplification is needed. In the GEMPix this is provided by an assembly of three GEM foils.

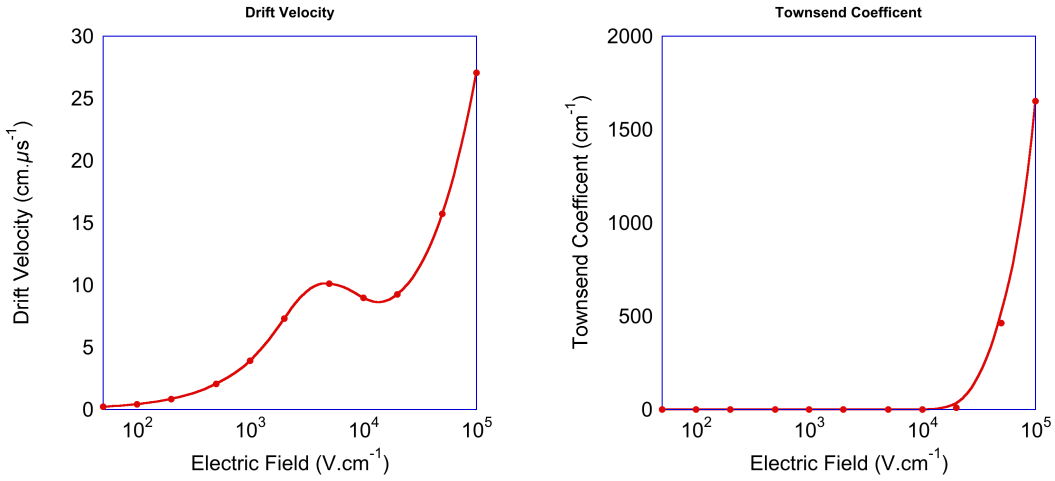

(a) (b)

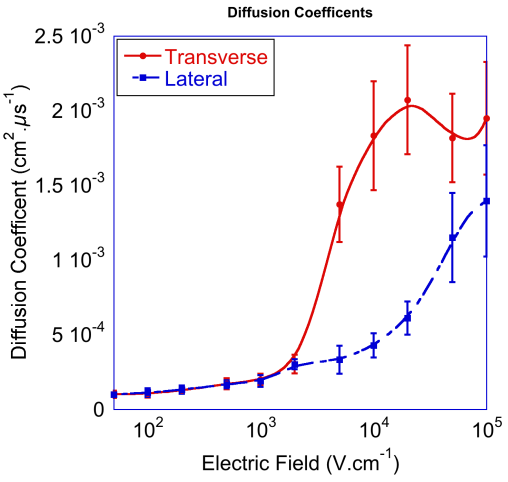

(c)

Figure 6.1: Values of the electron drift velocity (a), Townsend Coefficient (b) and Diffusion coefficients (c) calculated for Ar:CO_2:CF_4 in a 45:15:40 ratio using Magboltz [111].

GEM foils are a relatively recent innovation in detector technology first invented at CERN by F.Sauli in 1996 [109]. A GEM foil consists of a thin insulating layer (typically made of Kapton) which is electroplated with a conductive metal on both sides. Small holes are then etched in this foil and a voltage applied across it as shown in figure 6.2. This produces electrical fields as high as $100\,\mathrm{kV\,cm^{-1}}$ inside the holes. When an electron traverses the hole this allows for the formation of a localized electronic avalanche typically producing of the order of 20 electrons for each input electron. A key advantage of GEM technology is that because the gas multiplication is restricted to a very localised region very low input signals can be easily amplified and read out, or high particle count rates can be measured without a risk of discharges and sparks (normally onto sensitive read out electronics). The exact gain depends on the gas used and the voltage applied. In general the gain G (defined as the ratio of output to input electrons) produced by a GEM follows the exponent of the applied voltage,

$$G \propto e^{\alpha V} \tag{6.4}$$

where the Townsend Coefficent α depends on the gas or gas mixture used.

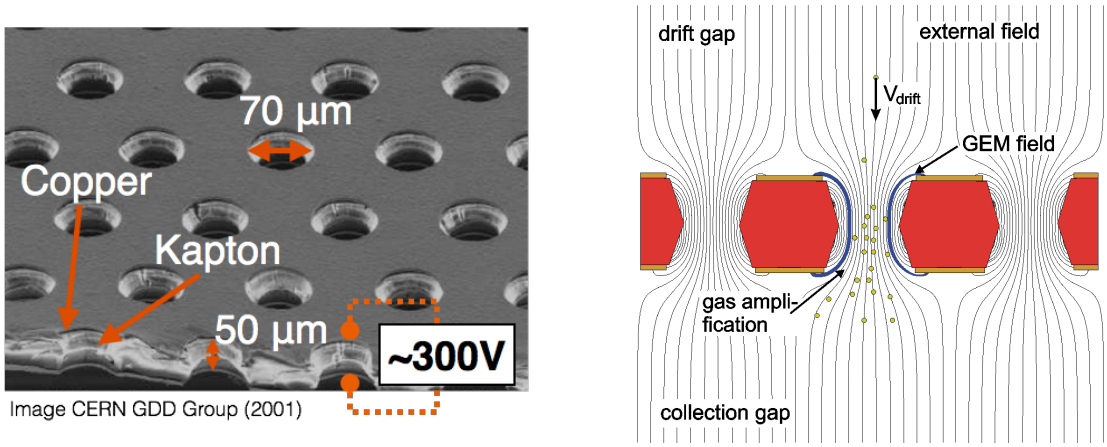

Figure 6.2: Left - Electron microscopy of a GEM foil (image courtesy CERN Gas Detectors group, annotations added by author), Right - Sketch showing the electric fields and gas multiplication process in a GEM foil, from [113].

A typical use case is a multiple GEM configuration. In this way each following

foil serves to multiply the output of the previous one and very high gas gains can be achieved. The GEMPix uses a triple GEM foil configuration with gains on the order of 10^2 - 10^4. In this case the gain is,

$$G \propto e^{\alpha V_1}.e^{\alpha V_2}.e^{\alpha V_3} \tag{6.5}$$

$$G \propto e^{\alpha(V_1+V_2+V_3)}. \tag{6.6}$$

As the gain is (nominally) only dependent on the summed applied voltage it is common in the GEM literature to refer to the summed applied voltage as the gain, i.e. 'a gain of 1.35 kV was applied'.

6.4 The GEMPix Detector

The GEMPix detector is made from a coupling of a small triple GEM assembly ($3 \times 3 \times 1.2$ cm^3) to a quad Timepix ASIC with 262,144 pixels of 55 µm × 55 µm area for read out. The detector essentially consists of three distinct regions. The first is a gas drift region where a signal of ions and electrons is generated by ionizing radiation. An external electrical field is applied to drift the electrons and ions towards the cathode and first GEM foil respectively. The second region is the amplification region consisting of a triple GEM structure which serves to amplify the drifted electrons. Finally at the bottom of the chamber is the Timepix read out. Detectors with drift regions above a position sensitive read out that can measure the drift time of charge are called Time Projection Chambers (TPC), and are widely used in high energy physics [114]. The whole geometry is shown in figure 6.3, a photograph of the detector is shown in figure 6.4.

6.4.1 Construction and Technical Details

In the GEMPix the GEM foils are held rigid by gluing them to a frame, and the electrodes supplying the high voltage are arranged in such a way as to avoid discharges onto the wire bonds of the Timepix read out. On top of the GEM/Timepix region is a 12 mm thick drift volume, topped with a mylar cathode metallized with a thin aluminium layer. A continuous flow of an external gas mixture is supplied externally

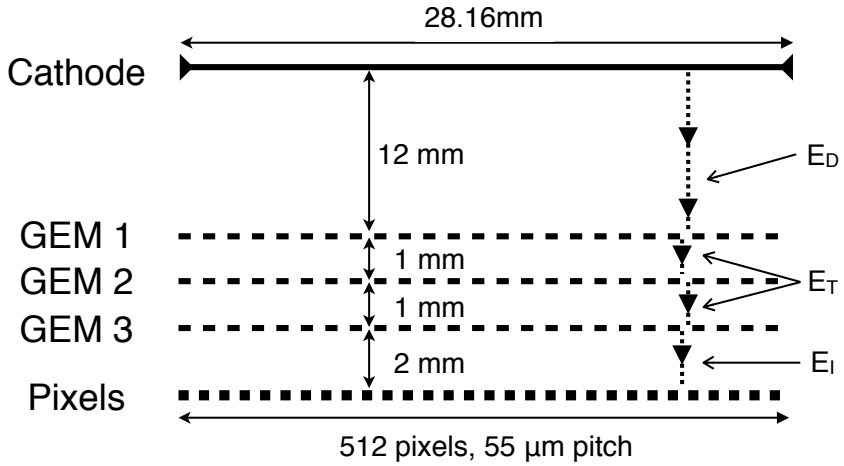

Figure 6.3: Diagram showing the principle dimensions and electric fields of the GEMPix detector (E_D = drift field, E_T = transfer fields, E_I = induction field, GEM 1,2,3 = GEM multiplication fields).

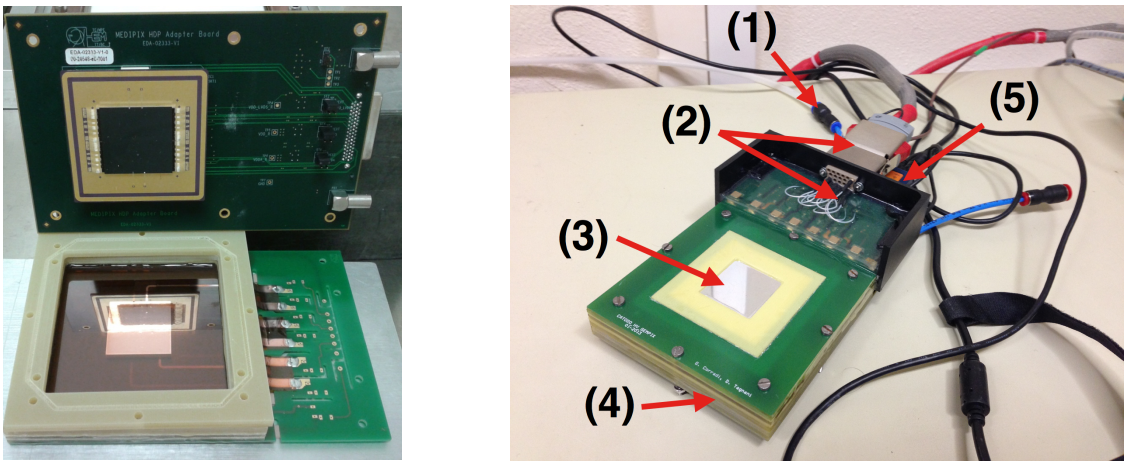

Figure 6.4: Photograph of the GEMPix detector, (left) open showing the quad Timepix ASIC for read out and (right) close showing the principle components (1 - external gas supply, 2 - external HV and fan out, 3 - Mylar window, 4 - frame to hold GEM foils, 5 - FITPix read out).

at a rate of 2-3 l h^{-1}. The whole system is made relatively gas tight with a thin layer of epoxy resin. Seven electrical fields (one per GEM foil, two charge transfer fields, an induction field and a drift field), shown schematically in figure 6.3 are controlled externally by an HVGEM unit.

The HVGEM is a system developed by INFN Frascati which provides 7 independent voltage channels, each with a maximum current limiter and trip control. The HVGEM is controlled via an OpenCAN interface which connects to a PC via a Kvaser USBCanII adaptor. Two different software packages are available for the HVGEM, the first is a Labview based GUI and the second (developed by the author) is a Python scripting interface. A screenshot showing the use of the two interfaces is shown in figure 6.5.

6.4.2 Read out with the Timepix ASIC

As noted in section 2.3.1 each pixel in the Timepix ASIC can operate in one of three modes: Counting (Medipix), Time Of Arrival (TOA) and Time Over Threshold (TOT). In TOA mode the chip measures the particle arrival time. In TOT the pixels act as a Wilkinson type ADC in order to measure the charge.

The Timepix operates with a frame based read out. This means that the chip possesses a digital shutter, and the pixels only count when the shutter is open. After the shutter closes the Timepix is then read out before acquiring a new frame. The FITPix system and accompanying Pixelman software are used to read out the Timepix. This allows us to read out the 2×2 array at approximately 10 Frames Per Second (FPS). This is a limitation of the serial IO method used by the FITPix, not the Timepix ASIC itself which features a much faster parallel bus which can be used up to 1 kHz. One significant limitation of the Timepix TOA mode is that to operate the pixels in TOA mode we are inherently limited in our frame length by the time of one clock cycle multiplied by the counter size in order to prevent the clock overflowing. At 9.8 MHz this limits the frame length to 1.2 ms, at 48 MHz to 246 µs. At 10 FPS this leads to a significant dead time of 98.8 % at 9.8 MHz and 99.75 % at 48 MHz.

As each pixel is individually programmable, it is possible to operate different pixels in different modes during the same acquisition. We exploit this feature to operate the detector in a so called 'mixed mode' where 1 in every 16 pixels measures TOA while the rest measure TOT. The advantages of this mode of operation are obvious, if clusters cover multiple pixels (as they do in the case of the GEMPix), it is possible to measure

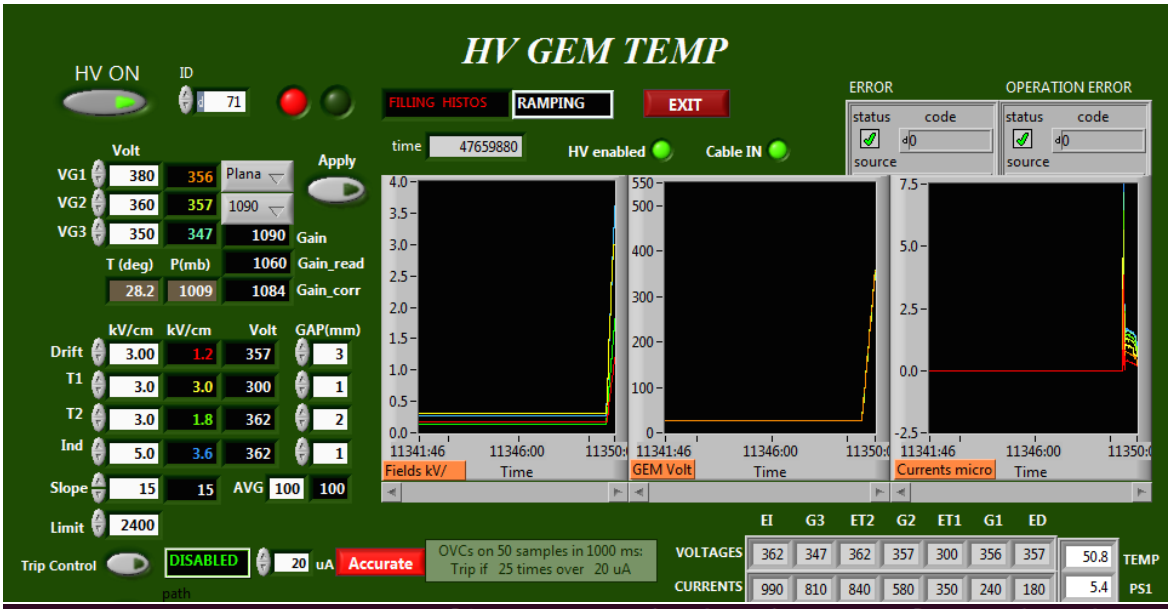


```
stuart@stuart-HP-Compaq-8200-Elite-CMT-PC:~/Desktop/HVGemDevelopment$ python
Python 2.7.5+ (default, Sep 19 2013, 13:48:49)
[GCC 4.8.1] on linux2
Type "help", "copyright", "credits" or "license" for more information.
>>> from GEMHV import *
>>> a = HVDevice(72)
>>> a.HVOn()
>>> a.HV = [150, 150, 150, 150, 150, 150, 150]
>>> a.LOC = 2400
>>> a.Ramp()
>>> a.HV
[29, 30, 29, 28, 30, 30, 62]
>>> a.HV
[105, 107, 105, 105, 106, 106, 106]
>>> a.HV
[149, 150, 149, 149, 150, 150, 149]
>>> a.Currents
[29, 28, 25, 22, 16, 6, 2777]
>>> a.HV = [0,0,0,0,0,0,0]
>>> a.Ramp()
>>> a.HV
[29, 30, 29, 28, 30, 30, 62]
>>> a.HVOff()
```

Figure 6.5: Interface for controlling the seven GEM high voltage fields using Labview (top) and Python scripting (bottom).

both the charge deposited by a track and the relative time of arrival, allowing for the construction of a 3D track of the particle based on the drift velocity of the ions in the gas.

6.4.3 Data Analysis

In a similar way to a Timepix detector with a silicon sensor the measured signal is a convolution of the physical particle track and the drift and amplification processes in the triple-GEM assembly. The key difference with the GEMPix is the prevalence of 'disconnected tracks' for particles with low stopping power such as muons, electrons and energetic hadrons. In this case a procedure is needed for reconstructing the track from its disparate components. Various methods are available including analytical track identification methods such as the Hough Transform [115] or shortening the acquisition time of one frame in order that it is likely that the frame will be empty or contain only one cluster. However the easiest in many measurements is to run the detector in TOA or mixed mode and use the time measurement as an additional degree of freedom in the clustering process in a similar way to the measurements at neutron time of flight beams described in chapter 5.

6.4.4 Setup of Quad ASIC

The threshold (THL) DAC value of different Timepix ASIC's can be quite different for the same real threshold (i.e. in volts). The reason for this is manufacturing differences between ASIC's. Thankfully as the THL step size is relatively constant across Timepix ASIC's setting up multiple chips with the same real threshold is simply a matter of setting all chips to some easily determined reference value (the simplest one is the centre of the noise once equalised which is provided by Pixelman during the equalisation process). The THL values are then all moved away from this reference point by the desired number of DAC steps (typically until the chip is noise free). If a silicon sensor is attached to the chip one can further homogenise the pixel responses with the calibration procedure used in chapter 1. In the GEMPix a separate process is used to partially homogenise the ASIC which is described in section 6.5.1.

6.5 Initial Characterisation with Photons and Alpha Particles

Figure 6.6 shows a sample frame measured at high gain ($G = 1350\,\mathrm{V}$) with an ^{55}Fe source (5.9 keV photons). The frame exhibits three distinct 'types' of clusters. The first is the primary ^{55}Fe photoelectron interactions. The second is a mixture of fluorescence photons from Argon in the gas mixture, and their associated photoelectrons (see section 3.2.4) and the third appears to be small clusters which are modulated by the presence of visible light. These clusters are speculated to be low energy photoelectrons produced by the aluminium cathode.

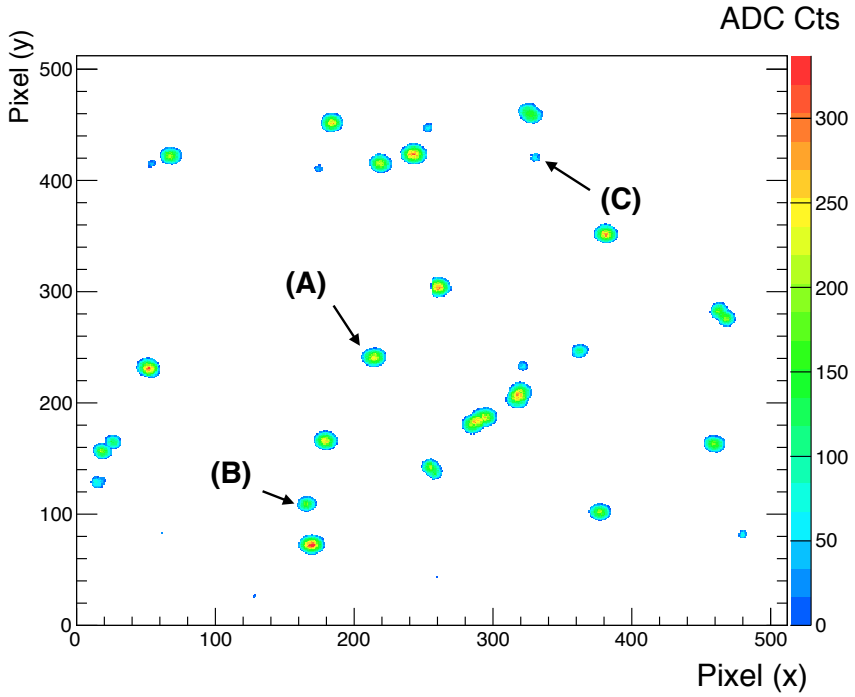

Figure 6.6: ^{55}Fe photons (5.9 keV measured with GEMPix detector. Clearly visible are primary ^{55}Fe interactions **(A)**, Argon escape (3.0 keV)/fluorescence (2.9 keV peak **(B)** and interactions due to visible light **(C)**.

An important parameter to characterize in a GEM based detector is the chamber gain [116]. This determines the number of electrons created by each primary ionization. A signal is only measured if the number of electrons reaching a pixel exceeds the threshold, so changing the gain in turn changes the minimum energy sensitivity of the detector. Figure 6.7 shows the number of clusters as a function of chamber gain for

^{55}Fe x-ray photons and ^{241}Am alpha particles. Both curves display a characteristic S shape, where the plateau value corresponds to 100% detection efficiency. Figure 6.8 shows the TOT values of the individual particle clusters as a function of gain, showing the expected exponential relationship. As the W value for x-ray's and alpha particles is very similar in the Ar:CO_2:CF_4 mixture used it is possible to construct a 'universal calibration curve' to read out energy for a given number of TOT counts as a function of gain by plotting the TOT per unit energy as a function of gain for both x-ray photons and alpha particles. This curve is shown in figure 6.9. The slowing down of ^{241}Am alpha particles in the mylar window was modelled with SRIM [117] and their energy deposition inside the drift volume was estimated to be 3.9 MeV.

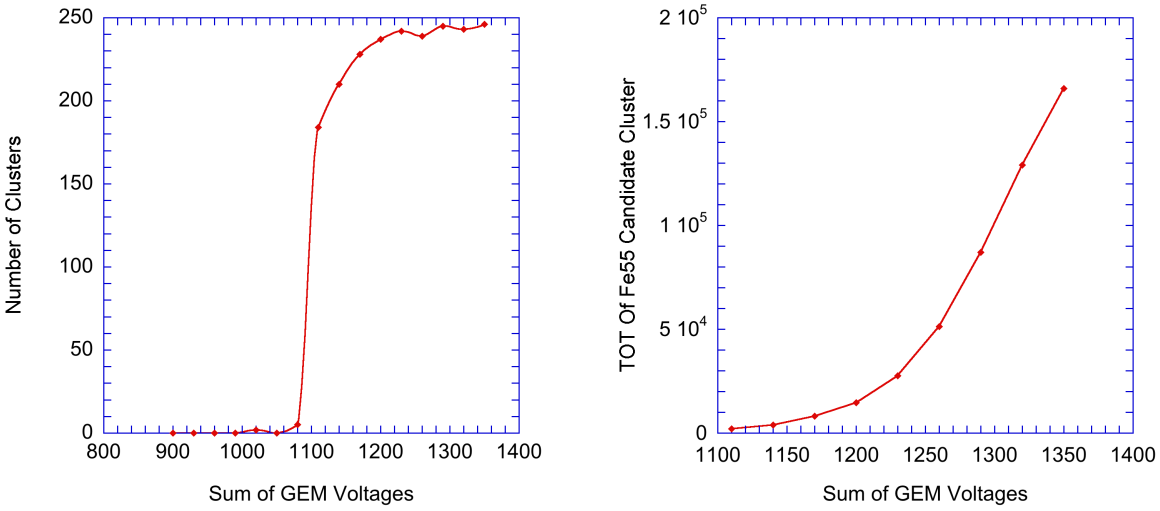

Figure 6.7: Average number of clusters (left) and cluster TOT (right) as a function of gain voltage for ^{55}Fe in Ar:CO_2:CF_4.

6.5.1 Energy Resolution Optimisation

The raw TOT spectrum of ^{55}Fe has an energy resolution of about 23%, as shown in figure 6.10c. Closer inspection of the TOT spectra in different regions can be performed by splitting the detector into 64×64 superpixels of 8×8 pixels each. The spectrum for 10 of these superpixels is shown in figure 6.10a. It is clear that there is a slightly different response in different regions of the GEMPix and so the peaks are not aligned. This is probably due to inhomogeneities in the gain of the GEM foils. The

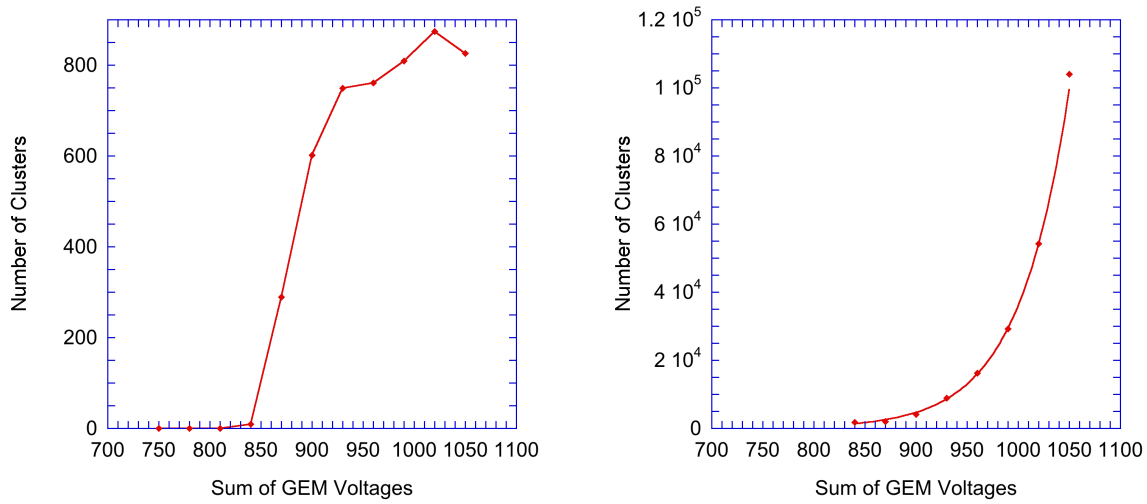

Figure 6.8: Average number of clusters (left) and cluster TOT (right) as a function of gain voltage for ^{241}Am in Ar:CO_2:CF_4.

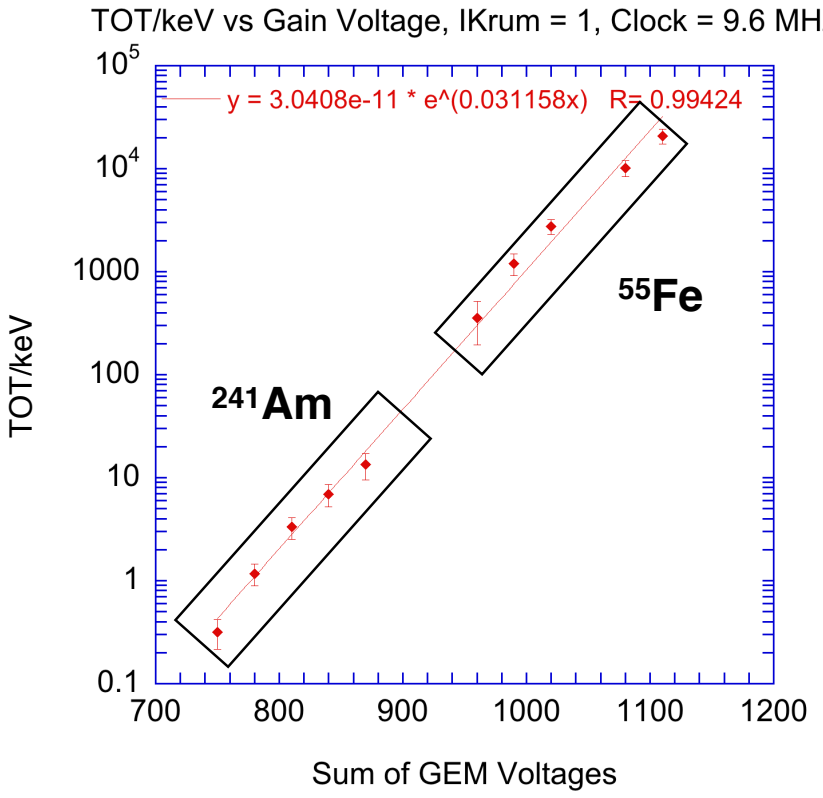

Figure 6.9: Energy calibration curve for GEMPix constructed using alpha particles and ^{55}Fe photons - TOT counts per input particle keV as a function of chamber gain.

superpixel procedure was followed largely because the amount of data required to do a per pixel style analysis would have been very large and time intensive to analyse[1], but also can be justified because the charge in one cluster is physically spread out over many pixels, so a per pixel analysis would not usefully compensate stochastic per pixel variations unlike the calibration procedures followed in chapter 2. Instead this procedure is intended to compensate systematic variations in the gain of the GEM foils and in the Timepix ASIC.

Figure 6.10b shows a map of the fitted gaussian peak position from figure 6.10a as a function of superpixel position. If the TOT value in each superpixel is then corrected so the peak value of the distributions lines up then the energy resolution of the GEMPix improves from 23% to 18.3% as shown in figure 6.10c. Several different superpixel sizes were chosen with fairly similar results (from 4×4 to 64×64), but only 8×8 is shown here as it gave the best results. A modicum of physical motivation for the selection of 8×8 as the superpixel size can be provided in that it is the closest of the superpixel sizes chosen to the overall size of a single cluster.

6.5.2 Particle Tracking Measurements

The GEMPix was used to measure a beam of $\frac{2}{3}$ protons and $\frac{1}{3}$ positive pions with momenta of 120 GeV/c at the CERF facility at CERN [62]. The CERF facility is fully described in chapter 3, however in this case was operated without a target (i.e, the only particles impinging on the detector should be minimum ionizing pions/protons and some scattered radiation).

The detector was placed approximately 10 m away from the beam aperture, allowing the beam to spread out somewhat, reducing its intensity. At this distance the impinging particle beam was nearly plane parallel, and is assumed to be for the calculation of the angular resolution of the detector. In order to test operation as a Time Projection Chamber (TPC) the detector was operated in TOA mode. A sample frame 250 µs long is shown in figure 6.11, where the colour scale denotes the counts of the detector running in TOA mode with a 48 MHz clock (1 count = 20.8 ns).

Except where otherwise noted the chamber is operated at a gain of (G = 2.10^4) corresponding to a total applied voltage to the GEM foils of 1.35 kV (450 V per foil)

[1] at 8 bytes per pixel, $\approx$ 100 pixels per cluster, $\approx$ 1000 clusters per pixel for useful statistics and 262,144 pixels this adds up to 209 gigabytes of raw data

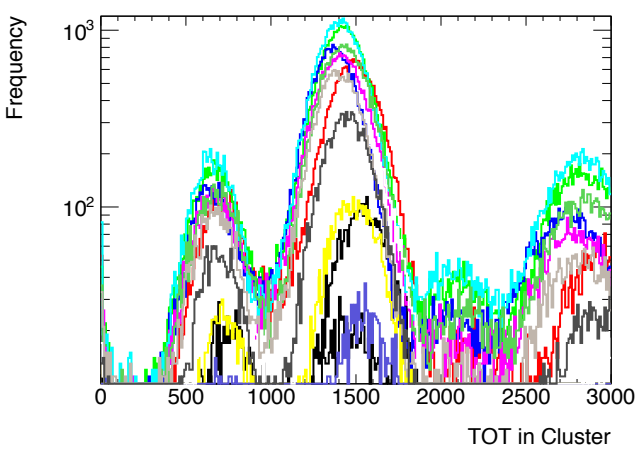

(a) Superpixel response

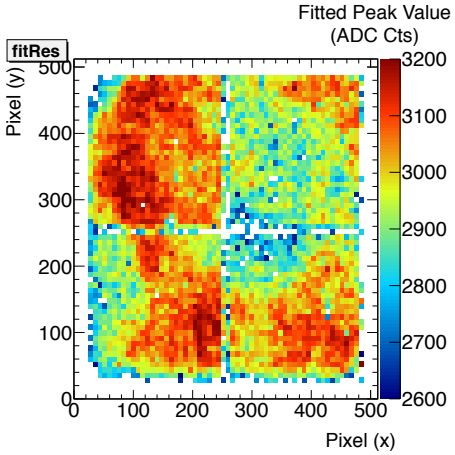

(b) Map of fitted centroids from (a)

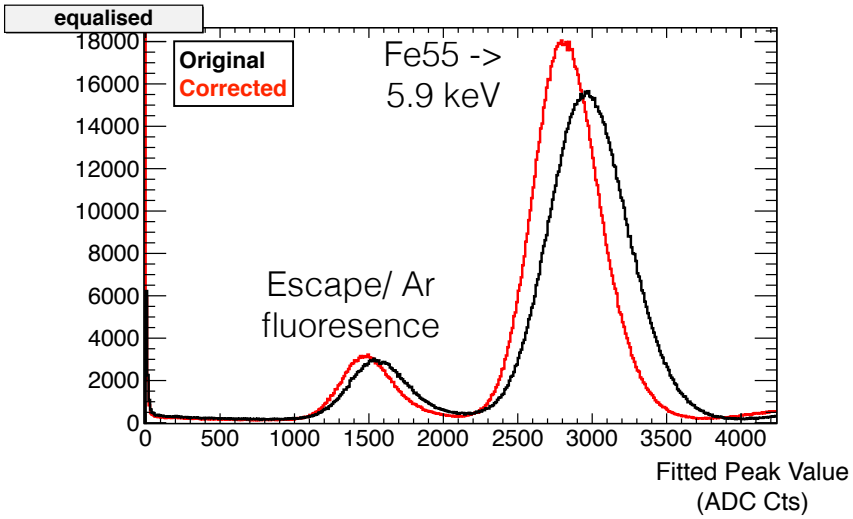

(c) Optimised response by aligning peaks in (b)

Figure 6.10: GEMPix Response Equalisation Process - the detector is split into regions of 8×8 pixels, the response of 10 of these is shown in (a), the per region response is fitted with gaussians, a map of the centroids is shown in (b) and finally the centroids are aligned with a linear weighting factor, which when applied to the whole spectrum improves the energy resolution to 18.3%.

[110] and a drift field of 0.66 kV cm^{-1}.

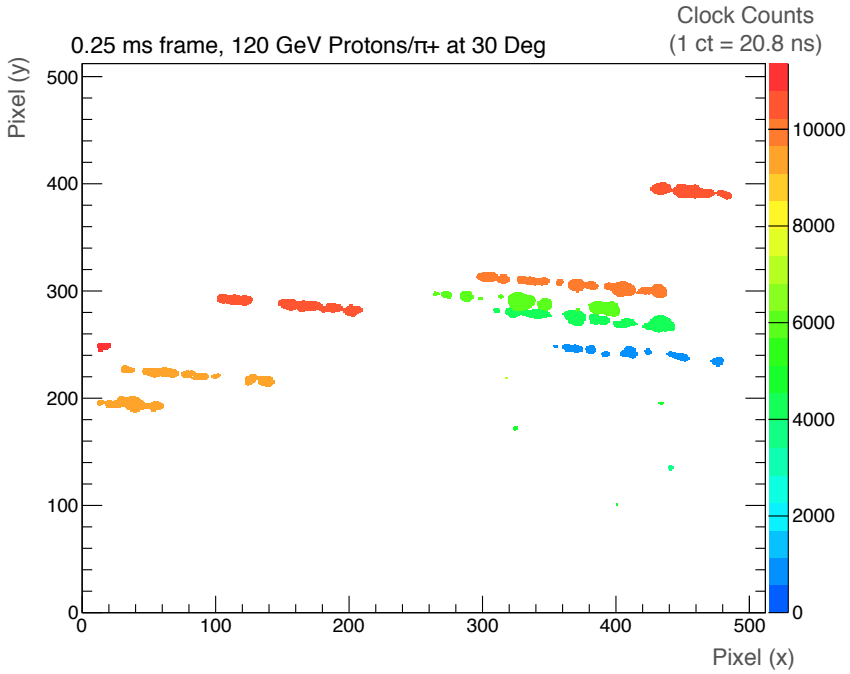

Figure 6.11: Sample frame taken with 120 GeV proton/pion tracks. The beam was incident at 30 degrees and the chip operated in TOA mode. The color of a track denotes its time of arrival (as per the counting scheme in the Timepix ASIC higher counts arrive earlier). Individual particle tracks are clearly visible.

6.5.3 Track Object Reconstruction

There are clearly well separated track-like objects in figure 6.11, consisting of several contiguous clusters of pixel hits [55]. In order to construct tracks the pixels are first grouped into clusters by performing a flood-fill search on a hit pixel for neighboring pixels with a TOA value within 2 counts (±41 ns). Single pixel hits are probably read out noise and hence ignored. Once all the clusters in the frame have been constructed they are then grouped into tracks. To do this a search in TOA is performed with some wider bin (in this case 10 counts, or 200 ns) and a minimum proximity requirement for the centroid of the cluster (within 50 pixels). Finally the completed track can be analyzed for useful information. Figure 6.12 shows examples of reconstructed tracks at 0, 20 and 40 degrees. The color scale denotes the TOA value. We use a custom code to find clusters and construct tracks, and use the ROOT [51] based MAfalda

framework to interface with the Timepix data [52].

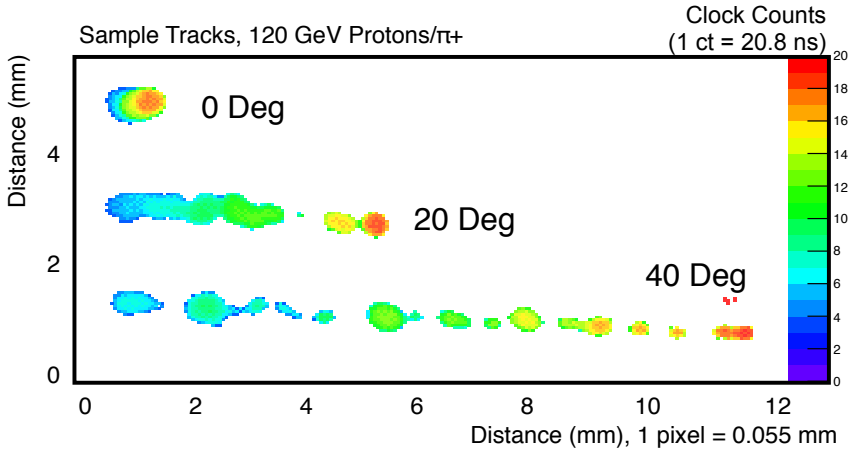

Figure 6.12: Sample 120 GeV/c proton/pion tracks at different angles of incidence. The color of a track denotes its time of arrival (higher counts arrive earlier).

6.5.4 Results of Gain and Drift Scans for Tracks

Figure 6.13 shows the result of a scan in GEM foil voltage measured with the impinging particles at a 30 degree angle of incidence. Figure 6.13(a) shows the number of objects as a function of total GEM voltage (summed voltage over all GEM foils) for all clusters and tracks while figure 6.13(b) shows only candidate tracks with a length of over 100 pixels, or 13.2 mm if the particle is assumed to fully penetrate the drift volume. A track incident at 30 degrees should have a length of 125 pixels. This length is determined by computing the distance between the two intersection points of a least squares best fit line through the hit pixels of track with its minimum bounding box which is found using a rotating calipers procedure [118].

Both figures 6.13(a) and 6.13(b) show a characteristic S shape with a knee at 1300V and both curves reach a plateau value which implies that the track detection efficiency is 100%. Interestingly at an applied voltage of 1380 there is a sudden increase in the number of clusters (and hence tracks) which is associated with a large number of small, randomly placed clusters. This effect has been observed to be modulated with the amount of ambient light and we speculate that it is associated with single photoelectron emission off the aluminium on the 12 µm mylar cathode of the detector. As these clusters are small and randomly distributed, they have no effect on the measured number of tracks shown in figure 6.13(b).

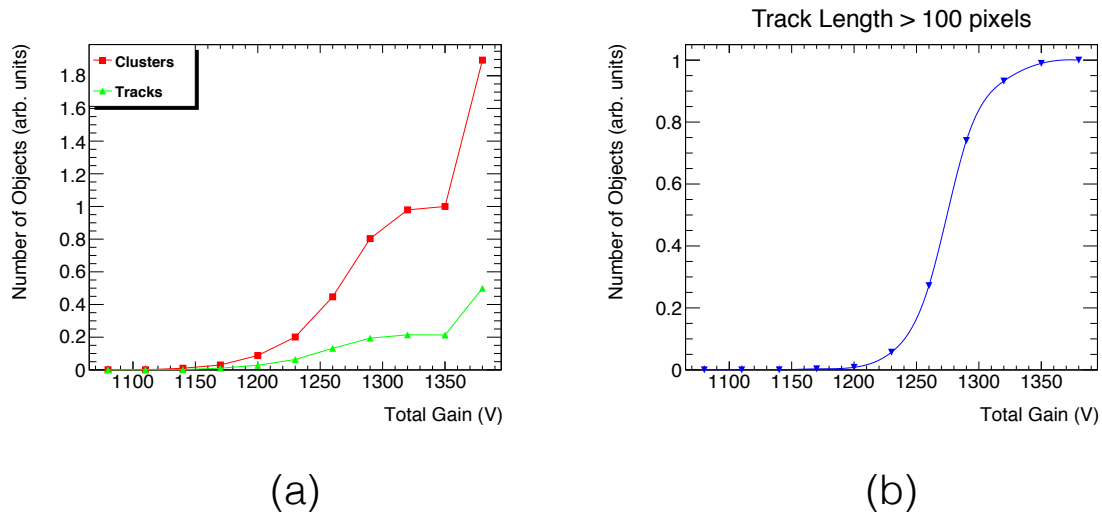

Figure 6.13: Gain voltage scan for the GEMPix at a 30 degree angle of incidence (a) shows the total number of clusters and tracks, (b) Shows only constructed tracks with a length $>$ 100 pixels, most of which should be primary beam particles (fit with a cubic spline).

Figure 6.14(a) shows the results of varying the chamber drift field on the time of arrival difference between the bottom and the top of candidate tracks incident at 30 degrees (the same track selection as figure 6.13(b)). As these tracks should pass through both the bottom and top of the drift volume this time is equal to the drift time of the electrons over the 12 mm drift gap. From a Gaussian fit to these distributions the drift velocity of Ar:CO_2:CF_4 can be measured which is shown in figure 6.14(b). If the track is assumed to enter at the top of the drift volume and exit through its bottom then this calibration can be used to provide an absolute track position in 3D space. Shown for comparison is a Magboltz [111] simulation of the drift velocity in the used gas mixture. In general the simulation matches the results well, with a small systematic shift.

6.5.5 3D Track Reconstruction and Measurement of Angular Resolution

The drift velocity at 0.66 kV cm^{-1} was measured to be 2.97 cm µs^{-1}. With this result the 3D positions of the pixel hits and hence the path of the track can be reconstructed as shown in figure 6.15. The track is fit with 3D least squares to all of the pixel hits

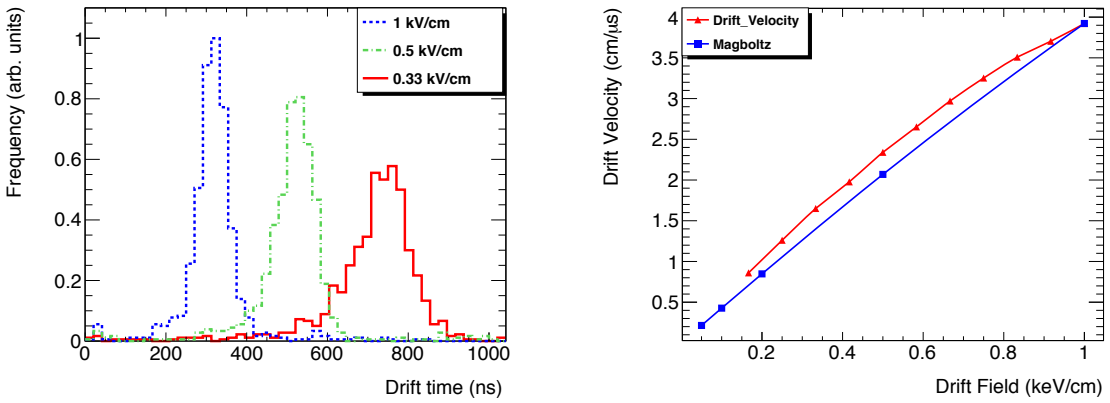

(a) (b)

Figure 6.14: (a) track time difference distributions for different incident drift fields, (b) drift velocity measurement formed by plotting the centroid of a Gaussian fit of the distributions in (a) against the drift field, compared to a Magboltz simulation of the gas mixture used for reference.

in 3D space. Two quantities are computed from this fit, the azimuthal angle θ and the altitude angle ϕ. Distributions of θ and ϕ can be computed as a function of the incident beam angle. These are shown in figure 6.16(a) and figure 6.16(b). The moving centroid of the θ distributions can be attributed to slight changes in the orientation of the GEMPix as the detector was repositioned for new measurements.

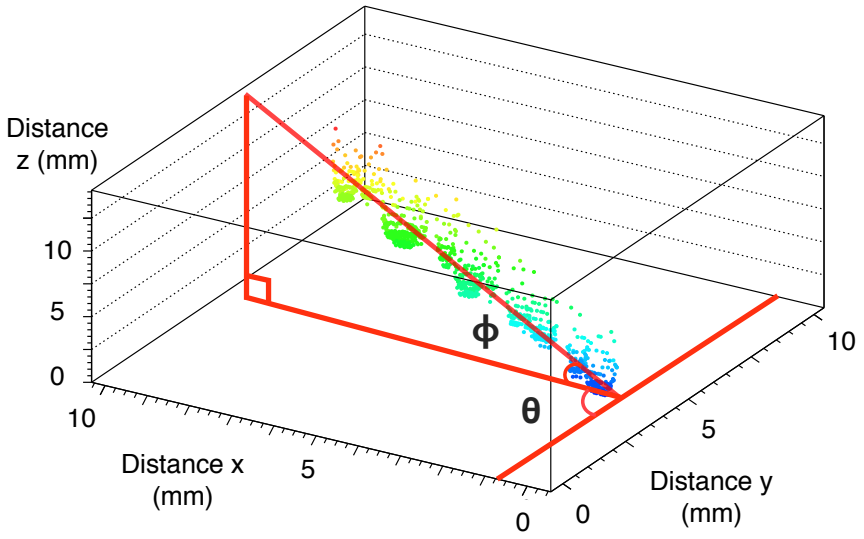

Figure 6.15: 3D least squares fit through of a track constructing the θ and ϕ angles.

Figure 6.16(c) shows the angular resolution of these profiles which we define as the Full Width Half Maximum of the distributions in figure 6.16(a) and figure 6.16(b). The θ resolution improves with increasing beam angle (longer tracks provide more sampling points) to a minimum value of 1.2 degrees at 40 degree ϕ angle, while the ϕ resolution decreases. The θ resolution is in general better than the ϕ resolution. The reason for this is that the intrinsic drift resolution of the GEMPix is inferior to the lateral resolution of the pixel pad (electrons drift approximately 0.5 mm, or 10 pixel lengths in one clock count).

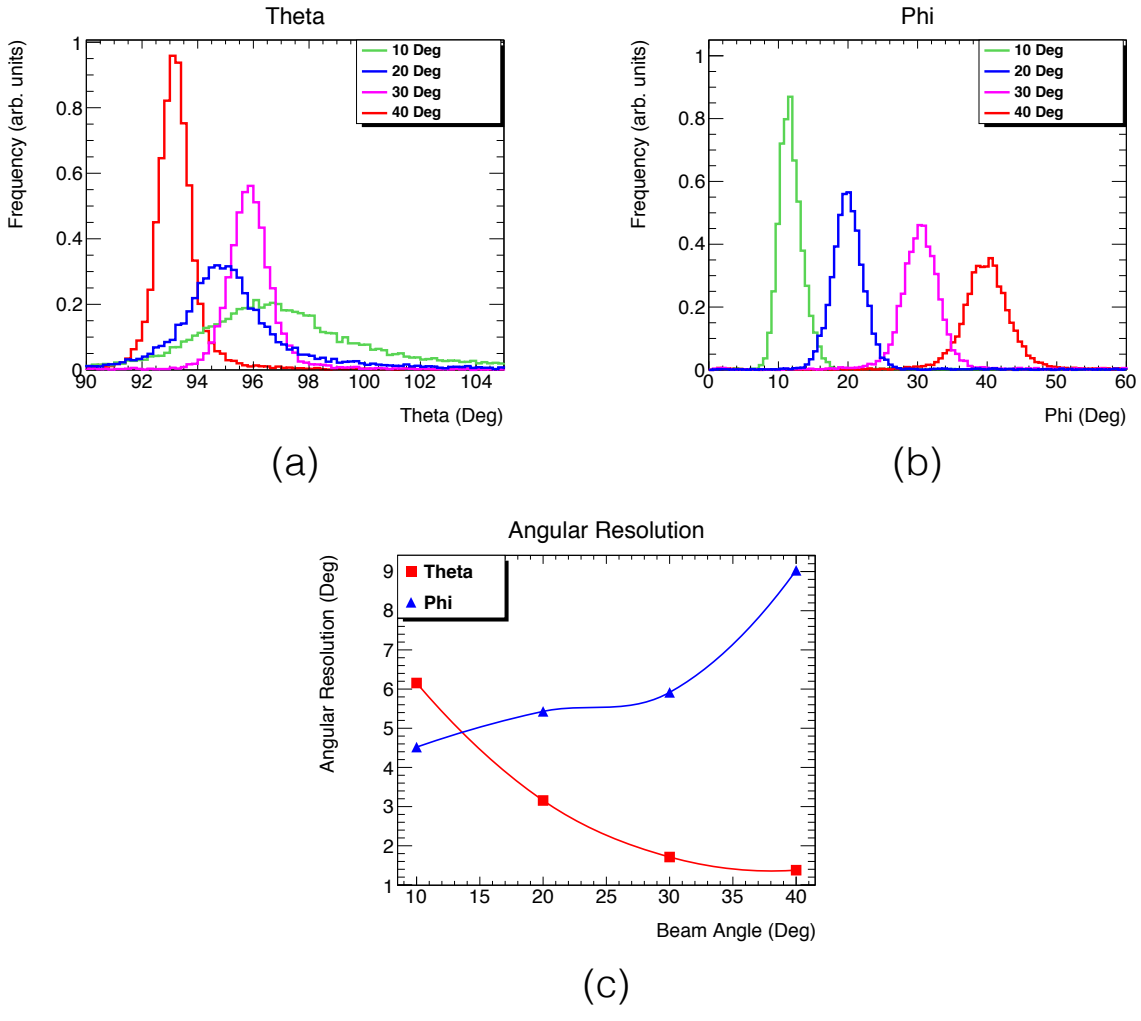

Figure 6.16: (a) Theta distribution as a function of incident beam angle, the centroid of the distribution slightly changes as the detector was repositioned by hand (b) ϕ distribution as a function of incident beam angle, (c) angular resolution of θ and ϕ as a function of beam angle, defined as the FWHM of Gaussian fits to (a) and (b).

6.5.6 Track Fitting Parameters and Spatial Resolution

The spatial resolution of tracks was investigated for 40 degree tracks. Unlike the fits computed in the preceding section, this was investigated by separating the track into individual ionization clusters and fitting the identified 3 dimensional centroids of these clusters. Identification of the individual ionization clusters is clearly a more physically motivated approach than a fit to all of the pixel hits as used in the previous section. However for angles lower than 40 degrees it is clear from figure 6.12 that a substantial number of individual ionization clusters would overlap.

Individual cluster hit positions were defined as the pixel hit centroid in x and y directions, and their average TOA count value in the z direction. Future work with the detector may motivate selecting a different TOA value (for example, the maximum TOA value, or fitting a distribution to the extended charge cloud), but for simplicity we choose the average.

Figure 6.17 shows the relevant fitting parameter distributions. The average number of clusters per track is 8.32 (6.02 per cm) and well fit with a Poissonian distribution. The individual track residuals in the x,y and z directions are also shown. The width of the residual in y ($\sigma = 45.9\,\mu m$) is much smaller than that in x ($\sigma = 331.9\,\mu m$) or z ($\sigma = 292.9\,\mu m$). This is because the particle beam is aligned along the y axis, so the y residuals are angled perpendicular to the fit and so insensitive to changes in the fit parameters in the x and z direction. The correlation between the x and y variables is also shown in figure 6.17. The x and z residuals are highly correlated as they both lie angled (40 and 50 degrees respectively) to the fit and so are subject to the considerably larger error in z axis measurement.

Defining an estimate of the resolution as $\frac{\sigma}{\sqrt{n}}$ the resolution along the pixel pad can be estimated using only the y residuals as 19 µm. The total spatial resolution of the detector is 170 µm which is mostly limited by the time resolution of the detector.

6.6 Mixed Mode Operation for Tracking Measurements

The Timepix ASIC cannot simultaneously measure deposited charge (via the TOT measurement scheme) and time of arrival. However, as our clusters are typically extended over many pixels, we can operate our detector in a so called mixed mode

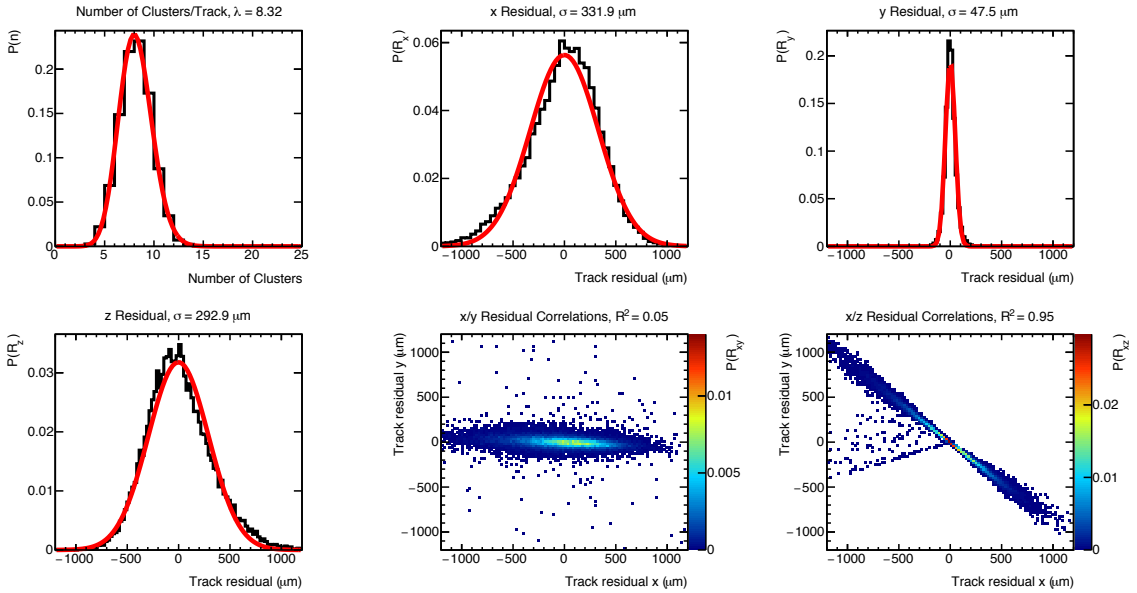

Figure 6.17: Fit parameters using individual clusters for tracks at 40 degrees. The x and z residuals are much larger than the y residual as they are highly correlated due to the path of the particles (roughly perpendicular to the y axis, at 50 and 40 degrees to the x and z axes respectively).

where 1 in every 16 pixels measure TOA while the rest measure TOT. Figure 6.18 shows a sample track at 30 degrees measured using this dual mode scheme.

6.6.1 Charge Measurement

The charge deposition spectrum for 30 degree tracks is shown in figure 6.19. The curve is Landau-like but is not well described by a Landau function. As the GEMPix is a small and thin detector ($3 \times 3 \times 1.2\,\mathrm{cm}^3$) the Landau curve is expected to be truncated. This is because energetic delta electrons will exit the detector having only deposited a fraction of their total energy.

The curve is fit with a convolved Gaussian and Landau distribution, and the TOT counts are normalized to energy using a Geant4 [92] simulation of the energy deposition in 13.9 mm $\left(\frac{12\,\mathrm{mm}}{\cos 30}\right)$ of the Ar:CO_2:CF_4 gas mixture used in the detector using the Photo Absorption Ionization physics model [119] which is designed to simulate energy loss in thin gaseous absorbers. The range cut for the production of secondary particles was set to 100 μm. This distribution reproduces the high energy tail of the curve very well, but fails to reproduce the low energy part of the spectrum. In an at-

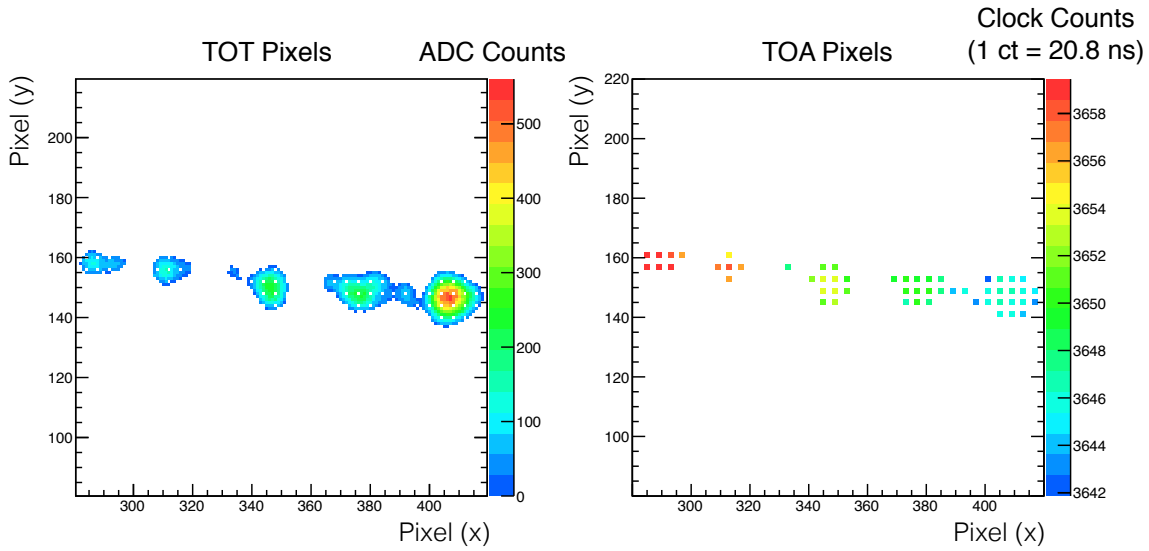

Figure 6.18: Example of a track incident at 30 degrees measured in mixed mode operation. 15 out of 16 pixels measure TOT (left) and 1 out of 16 measure TOA (right). The TOA pixels are drawn at twice lateral size for illustrative effect.

tempt to physically motivate the shape of this curve we convolved this spectrum with a Gaussian where the sigma of the Gaussian varies as a square root of the energy (a Fano like model). This model was used as the number of electrons produced in a GEM avalanche is highly variable for small (1-2) numbers of incident primary electrons [120]. This modified spectrum fits the described curve well.

Figure 6.20 shows the θ and ϕ distributions for the mixed mode operation compared to the pure TOA mode validating the tracking capabilities of the mixed mode operation. For both θ and ϕ the TOA distributions are slightly narrower than those measured in mixed mode.

6.6.2 Diffusion as a Function of Depth

The highly pixelated read out of the GEMPix makes it highly suitable for the investigation of the electron transport properties of gas detectors. Figure 6.21 shows the average cluster width as a function of the depth. The cluster width is defined as $2\sqrt{A/\pi}$ where A is the area of the cluster (the number of counting pixels multiplied by the area of one pixel). The energy calibration used to normalise figure 6.19 was used to bin the clusters by energy. Clusters were selected only from a subset of tracks which

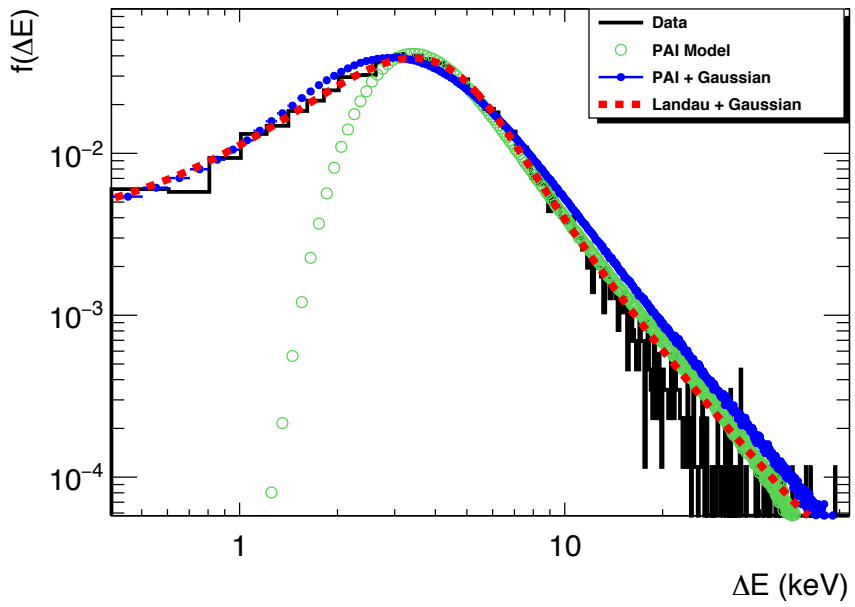

Figure 6.19: Energy deposition curve in the GEMPix fitted with a Landau distribution convolved with a Gaussian. The high energy part of the distribution nicely matches the Geant4 photo-absorption ionization (PAI) model, but additional Fano like Gaussian smearing where the sigma follows the square root of the energy is required to fit the low energy part of the curve.

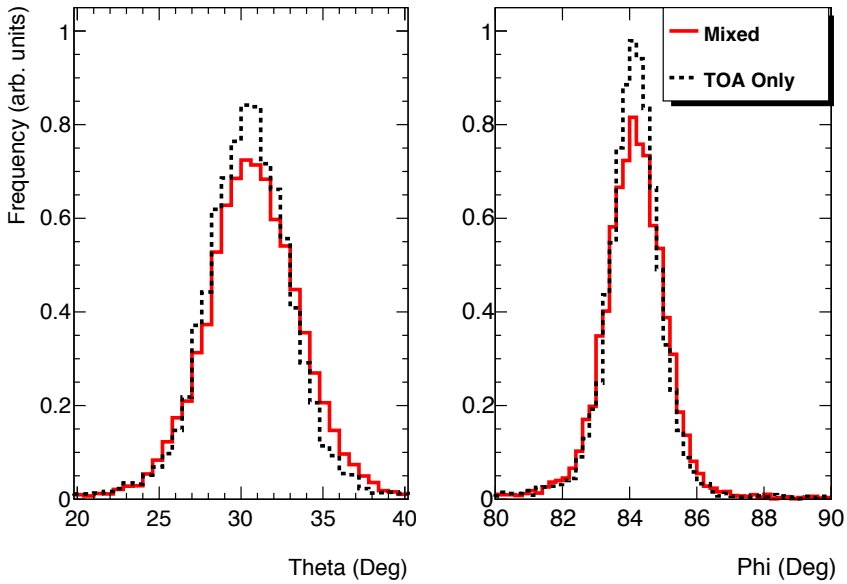

Figure 6.20: Comparison of θ and ϕ reconstruction in mixed and TOA modes at 30 degrees. The mixed mode distributions are slightly wider than the pure TOA mode distributions.

are highly linear (i.e. with no significant delta electron emission), and which appear to fully penetrate the drift volume in order to ensure that the z position is accurate. It is difficult to account for overlapping clusters as ionization events consisting of only a few electrons may be inherently highly asymmetric given the stochastic nature of electron transport. The charge binning used can only be used to approximate the number of primary ionizations as small numbers of electrons produce an extended, long tailed avalanche distribution in GEM based detectors [120].

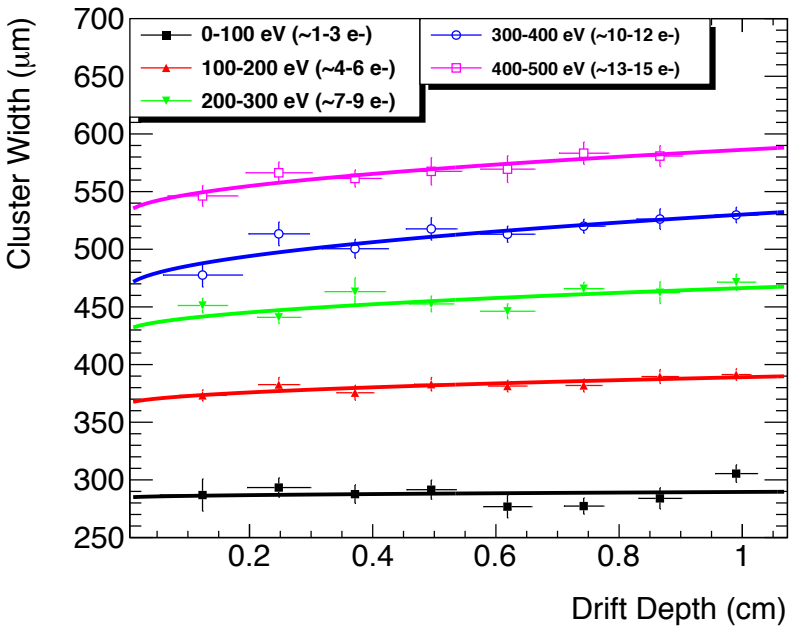

Figure 6.21: Cluster width as a function of drift depth for different charge bins. The curves are fit with functions of the form $y = a + \sqrt{bx}$.

In the the plots in figure 6.21 the cluster widths are fitted with a square root curve ($y = a + \sqrt{bx}$) following the classical diffusion relation $\sigma = \sqrt{2Dt}$ where σ is the diffusion width of a point like cloud in a gas with diffusion coefficient D and drift time t. The b parameter is almost flat for single/double electron clusters, but becomes increasingly larger for multi-electron clusters. At its highest value the b parameter is much less (approximately a factor 5) than the diffusion coefficient for the Ar:CO_2:CF_4 gas mix used. This is probably because of the high (>1000 e-) threshold in each pixel. For small charge clouds a relatively large fraction of the cloud may be below threshold and so undetectable.

The a (intercept) parameter as a function of primary cluster energy is shown in

figure 6.22. We interpret this as the measured cluster width for interactions at the bottom of the drift volume (i.e. the 'intrinsic' cluster width generated by the triple GEM assembly).

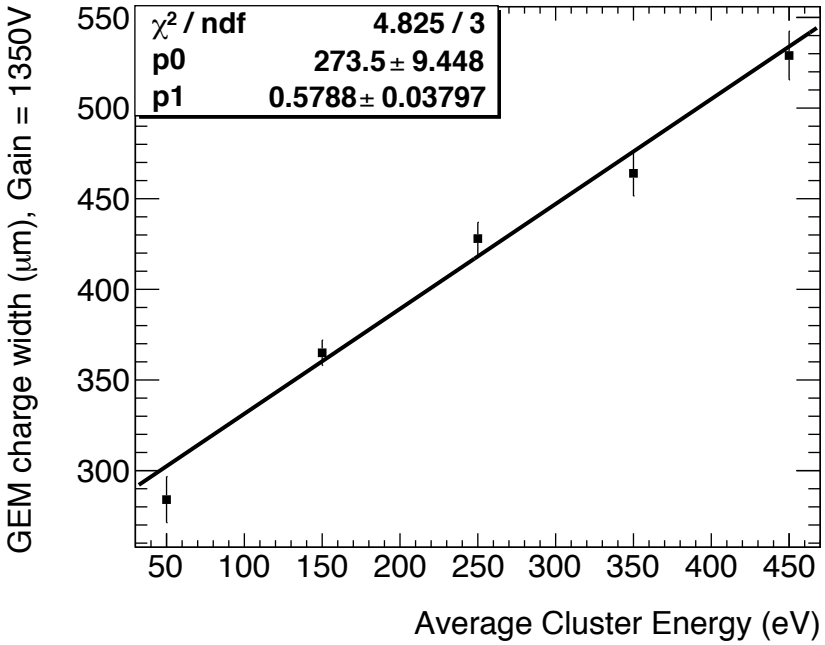

Figure 6.22: Measured cluster width from interactions at the bottom of the drift volume as a function of energy (intercepts from fig. 6.21). Fit linearly with $y = \mathrm{p0} + \mathrm{p1}x$.

6.7 Future Improvements to the GEMPix

In the future it should be possible to improve low charge performance of the detector with detailed characterization of the Timepix ASIC, specifically by introducing a charge calibration and compensating for the timewalk effect for low charges.

The charge response of a Timepix pixel is nonlinear for low charges (below about 4000 electrons). The standard procedure [38] for determining this function relies on single pixel hits from characteristic photon lines which are impossible to produce in the GEMPix. The Timepix ASIC also has a test pulse functionality which injects a fixed amount of charge into the preamplifier but this does not reliably describe the shape of the surrogate function at low charges [39].

The timewalk effect occurs when the rise time of a low charge signal is significantly different than for a high charge one, resulting in a systematic shift of a few counts in the TOA measurement.

Use of the Timepix3 ASIC [121] could considerably improve the performance of the GEMPix. The Timepix3 test pulse functionality has been demonstrated to work well allowing for easy read out calibration. The Timepix3 also measures time and charge simultaneously removing the need for a mixed mode and features a time resolution of 1.5 ns which corresponds to a distance on the order of the pixel pitch (with an equivalent triple GEM assembly). Finally the Timepix 3 offers a data driven read out (which sends out the measured information as soon as pixels go low) with maximum data throughput rate of 85 Mhits/second which should improve the dead time, or remove it entirely in low count rate situations.

One of our target applications is to use the GEMPix as a particle tracker that can measure energy deposition/track structure in tissue equivalent gases over biologically relevant site sizes, i.e. as a microdosimeter. The central principle of such a detector is that the atomic composition and number of atoms in a given path length is the same as that found in a biological site, such as a cell nucleus. This seems eminently achievable with the GEMPix as the length of a HeLa cell nucleus is some 10 µm, the equivalent path length in a propane based tissue equivalent gas at STP is some 90 pixels. Future work in this regard will focus on producing appropriate algorithms to extract microdosimetric spectra and validation of the GEMPix against existing devices (typically Tissue Equivalent Proportional Counters, TEPC).

To motivate this application in figure 6.23, we show some of the more unusual interactions measured using the detector. Figure 6.23(a) shows a shower probably originating in the wall of the detector, (b) a multiple scattering particle, probably an electron, (c) a dense track (most likely a light ion emitting delta electrons and (d) a primary particle (i.e. a 120 GeV/c proton or pion) emitting a delta electron.

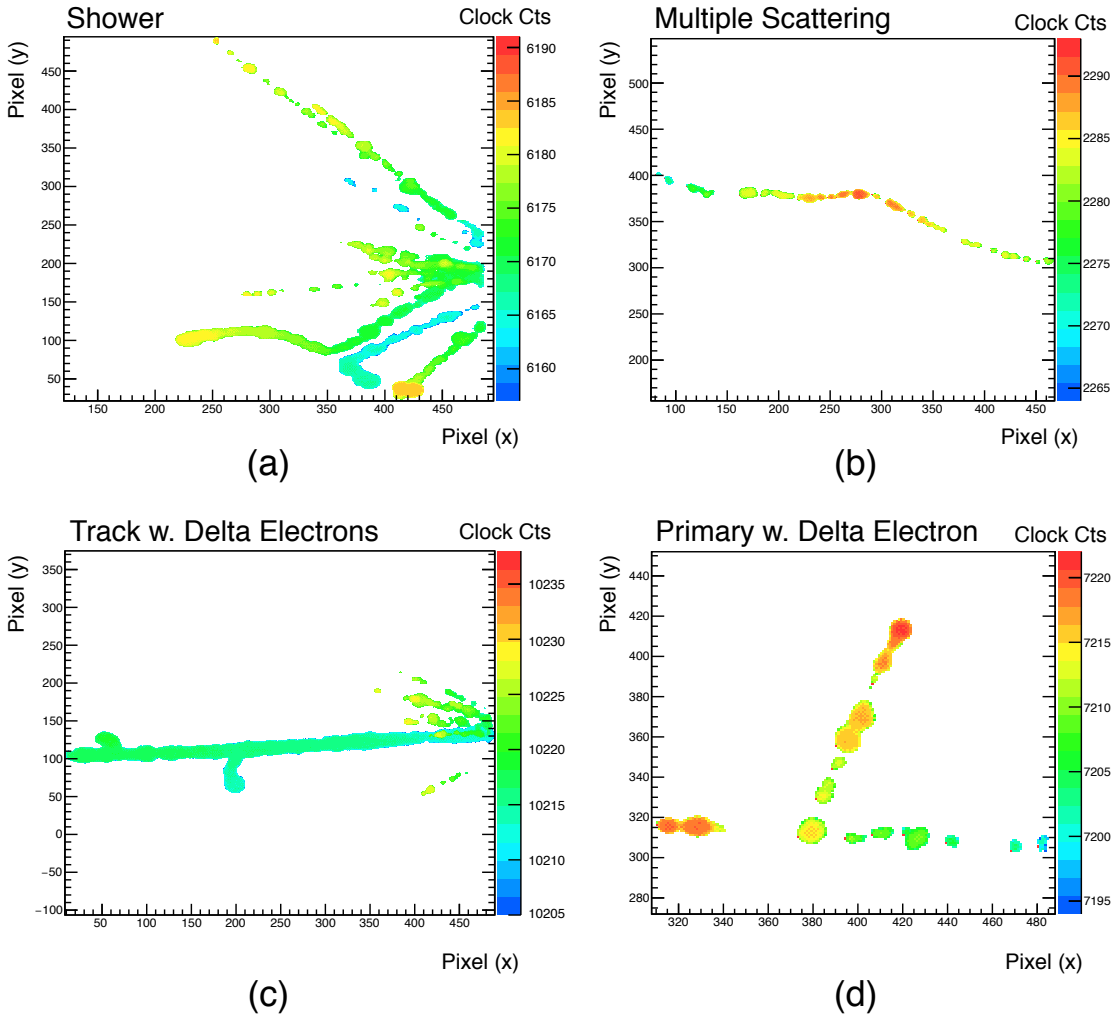

Figure 6.23: Unusual events measured with the GEMPix in TOA mode (a) shows a shower most likely originating in the wall of the detector, (b) shows a particle multiple scattering, (c) appears to be a light ion, with a dense track and delta electron emission (d) appears to be a primary beam particle emitting an energetic delta electron.

Chapter 7

Conclusions

This thesis sought to explain how hybrid pixel detectors could be used in the evaluation of mixed fields.

Chapters 3 and 4 showed how mixed fields of charged particles could be evaluated using Timepix detectors with results that were generally comparable to other instrumentation such as tissue equivalent proportional counters and silicon telescopes. Chapter 3 showed that track morphology can contain useful information not contained with the LET spectrum of a mixed field, and chapter 4 extended that analysis to mixed fields in space and showed that the South Atlantic Anomaly demonstrates a clear angular anisotropy which could be dosimetrically important.

One interesting direction to take the analysis of data from Timepix detectors in the future is to use the Timepix detector to identify dosimetric endpoints other than LET on the basis of track morphology. It would also be interesting to see how much information can be extracted from the visible (long range) delta electrons in heavy ion tracks.

Timepix detectors in space have a promising future. NASA has selected the Timepix detector to be the charged particle radiation monitoring system for the Orion capsule. The whole system (dubbed HERA for Hybrid Electron Radiation Assessor) consists of two Timepix detectors and an integrated computer for onsite data analysis. Timepix detectors have also flown on the recent Orion ETF-1 mission [122]. Outside of human spaceflight there are also Timepix chips mounted on Satellites - the SATRAM payload on the ESA Proba V satellite [123] and the LUCID micro satellite [124].

Chapter 5 showed the development process of a neutron dosimeter based on a multilayer plastic converter on a Timepix detector. The converters were simulated

and based on these simulations a 3D printed converter was designed and tested at the CERN NTOF neutron time of flight facility and the energy independence confirmed. Such a detector can be used in mixed charged particle fields due to its uncovered region which can be used to subtract the charged particle response from the other regions, although this has not been tested outside of a neutron-gamma field at CERN.

The principal limitations of such a detector are its sensitivity to low count/dose rates of fast neutrons. This is largely a function of the fairly low intrinsic cross section of neutrons in thin layers of plastic.

Future development of this detector could be extended in several directions, such as attempting to lower the energy sensitivity using materials other than hydrogenous plastic (such as ^{10}B for thermal neutrons) and in characterising the angular dependence of the device. The ultimate goals of such a project are twofold. Firstly a multilayered converter could be used in a mixed field to add neutron dosimetry capabilities to a Timepix detector. In such a use case one must be careful to understand how the converter and neutron fields affect the charged particle field and have a methodology for subtracting the neutron signal. The second case is the use of a multilayered converter with a much simpler read out as a neutron dosimeter.

Chapter 6 explored a the characterisation of a new kind of microdosimeter called the GEMPix. The operation of the device as a TPC was validated. The energy resolution when exposed to photons was optimised and the spatial and angular resolution of track reconstruction in the device were characterised.

Limitations of this device are the relatively high gas gains required to produce a signal over threshold (1000 electrons per pixel) and that there seem to be relatively large variations in the gas multiplication process for very low input charges.

Future work on the development of this detector as a microdosimeter should focus on comparison of the LET spectra that it can generate with other detectors such as Timepix detectors and tissue equivalent proportional counters. One interesting direction for the extension of this work is the operation of such a detector with low pressure gases and high gains. In this case it may be possible to operate the GEMPix as a nano-dosimeter, allowing fine inspection of radiation interactions on the scale of double strand breaks [125].

7.1 Future Perspectives

Hybrid pixel detectors are rapidly advancing, and due to their versatility and increasingly low cost are sure to find widespread application in many fields in coming years. In this section I briefly outline two new technologies - the Timepix3 and 3D silicon sensors which may have impacts on the field of dosimetry in years to come.

7.1.1 Timepix3

The current state of the art ASIC produced by the Medipix collaboration is Timepix3. Timepix3 offers many useful capabilities and improvements over the Timepix:

- A data driven read out operating at 85 million pixel hits per second. This read out pushes data to the computer as a soon as a pixel goes low. This removes the dead time associated with frame read out (which is very significant for short frames) as well as some of the overwrite/underwrite issues associated with very short frame lengths (see section 2.3.2).
- 1.56 ns time resolution for TOA and TOT.
- A lower threshold (about 500 electrons).
- Improved test pulse functionality.
- Corrected front end response for high charges (although the volcano effect remains a problem in Timepix3).
- Simultaneous TOA and TOT. An example track showing both TOA and TOT modes is shown in figure 7.1. Coupled with the above time resolution, in some situations this allows a Timepix 3 detector to act as a solid state TPC based on the drift time of electrons in silicon. An additional advantage of the TOA information is the ability to connect disconnected parts of a track such as delta electrons in a similar way to the methodology used with the GEMPix tracks in chapter 6.

For evaluation of mixed fields in silicon the simultaneous TOT and TOA is the principle advantage offered by the Timepix 3 detector as it should aid the clustering process. For high intensity mixed fields such as the field at CERF evaluated in

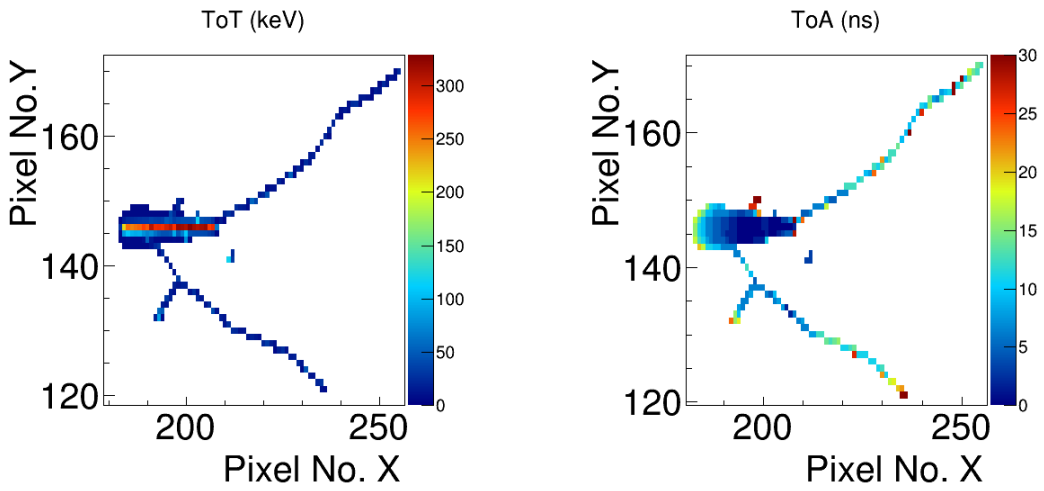

Figure 7.1: Track captured in a Timepix3 detector using simultaneous TOA/TOT mode, reproduced with permission from [126].

chapter 3 or those found in around photon linacs/proton therapy machines the vastly improved duty cycle from the data driven read out should also be very useful.

In the GEMPix detector the improved time resolution offered by Timepix3 should improve the spatial resolution in the z (drift) direction to roughly the same as the pixel ASIC (see section 6.7). The improved test pulse functionality should prove useful for setting up the ASIC.

7.1.2 3D Sensors

3D sensors consist of columnar electrodes of p (or n) type material that fully penetrate the silicon bulk in contrast to the implants at the surface of the sensor currently used [127, 128]. A diagram of a 3D sensor is shown in figure 7.2. There are several advantages of such devices. These are that the devices can be operated with much lower bias voltages than conventional silicon sensors as the width of the depletion region is much smaller. This means the bias voltage does not impose a limitation on the sensor thickness. The collection time of 3D silicon is also much faster (as the drift distances are much lower) than planar silicon and in principle the diffusion should be much lower (although this precludes TPC operation of a 3D silicon sensor). Finally the sensors are much more radiation hard than conventional silicon[1].

[1]This was the advantage that led to the development of 3D silicon for particle physics applications.

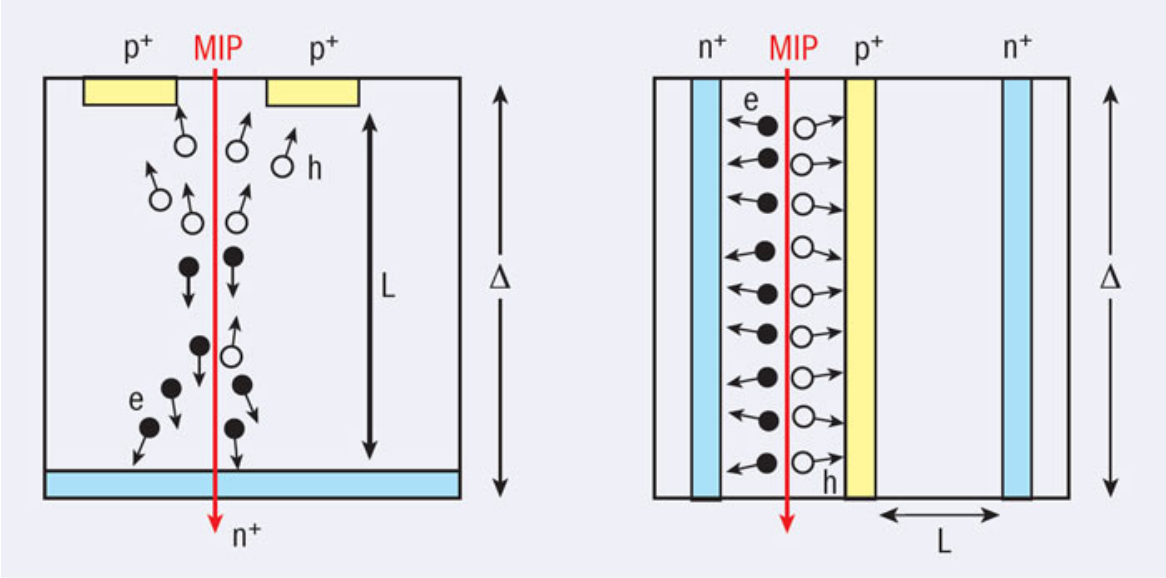

Figure 7.2: Cross section of a planar (left) and 3D (right) sensor. The collection length L and sensor thickness Δ are effectively decoupled in the 3D sensor leading to faster collection times and reduced diffusion. Figure reproduced from [129].

As the depletion region extends out from each electrode it is in principle possible to precisely control the fully depleted volume of each device, this has clear applications in microdosimetry [130]. For this reason it may be very interesting to attach a 3D sensor to a Timepix and evaluate its performance for dosimetric applications.

References

[1] International Commission on Radiological Protection. *ICRP Publication 74: Conversion Coefficients for use in Radiological Protection against External Radiation. Annals of the ICRP*, **26** (1996), 3-4.

[2] Guerrero, C., Tsinganis, A. et al. *Performance of the neutron time-of-flight facility n_tof at cern. The European Physical Journal A*, **49** (2013), 2:1.

[3] Knoll, G. F. *Radiation Detection and Measurement, 4th Edition.* John Wiley & Sons, Inc, Hoboken, New Jersey 07030, USA (2010).

[4] Metcalfe, P., Kron, T. et al. *The Physics of Radiotherapy X-rays and Electrons.* Medical Physics Publishing Corp. (2012).

[5] International Commission on Radiological Protection. *ICRP Publication 103: The 2007 Recommendations of the International Commission on Radiological Protection. Annals of the ICRP*, **37** (2007), 2-4.

[6] Narici, L., Bidoli, V. et al. *ALTEA: Anomalous long term effects in astronauts. A probe on the influence of cosmic radiation and microgravity on the central nervous system during long flights. Advances in Space Research*, **31** (2003), 1:141.

[7] Little, M., Tawn, E. et al. *A systematic review of epidemiological associations between low and moderate doses of ionizing radiation and late cardiovascular effects, and their possible mechanisms. Radiation research*, **169** (2008), 1:99.

[8] Shore, R. E., Neriishi, K. et al. *Epidemiological studies of cataract risk at low to moderate radiation doses:(not) seeing is believing. Radiation research*, **174** (2010), 6b:889.

[9] Chodick, G., Bekiroglu, N. et al. *Risk of cataract after exposure to low doses of ionizing radiation: a 20-year prospective cohort study among US radiologic technologists. American journal of epidemiology*, **168** (2008), 6:620.

[10] United Nations Scientific Committee on the Effects of Atomic Radiation. *Sources and effects of ionizing radiation. UNSCEAR 2000 report to the General Assembly, with scientific annexes. Volume I: Sources.* (2000).

[11] Bordry, F. *LHC Long Shutdown 1 Status LS1@SPC (8th report).* `https://indico.cern.ch/event/338501/session/0/contribution/0/attachments/663271/911736/Slides-LS1SPC_16_September_2014_Fk_Bordry.pdf` (2014). Accessed: 23/09/2015.

[12] Cucinotta, F. A. *Space radiation risks for astronauts on multiple International Space Station missions. PloS one*, **9** (2014), 4.

[13] Cucinotta, F. A., Kim, M. et al. *How safe is safe enough? Radiation risk for a human mission to Mars. PLoS One*, **8** (2013), 10:e74988.

[14] DiCarlo, A. L., Maher, C. et al. *Radiation injury after a nuclear detonation: medical consequences and the need for scarce resources allocation. Disaster medicine and public health preparedness*, **5** (2011), S1:S32.

[15] Tubiana, M., Aurengo, A. et al. *The debate on the use of linear no threshold for assessing the effects of low doses. Journal of Radiological Protection*, **26** (2006), 3:317.

[16] United Nations Scientific Committee on the Effects of Atomic Radiation. *Sources and effects of ionizing radiation. UNSCEAR 2000 report to the General Assembly, with scientific annexes. Volume II: Effects.* (2000).

[17] O'Brien, K., Friedberg, W. et al. *Atmospheric cosmic rays and solar energetic particles at aircraft altitudes. Environment International*, **22** (1996):9.

[18] Stern, D. and Peredo, M. *Cosmic rays and starlight.* `http://www-spof.gsfc.nasa.gov/Education/wcosray.html` (2005). Accessed: 23/09/2015.

[19] Mours, B., Boudreau, J. et al. *The design, construction and performance of the ALEPH silicon vertex detector. Nuclear Instruments and Methods in Physics Research Section A: Accelerators, Spectrometers, Detectors and Associated Equipment*, **379** (1996), 1:101.

[20] Rossi, L., Fischer, P. et al. *Pixel detectors: From fundamentals to applications.* Springer Science & Business Media (2006).

[21] Anghinolfi, F., Aspell, P. et al. *A 1006 element hybrid silicon pixel detector with strobed binary output. Nuclear Science, IEEE Transactions on*, **39** (1992), 4:654.

[22] Catanesi, M., Beker, H. et al. *Results from a hybrid silicon pixel telescope tested in a heavy ion experiment at the cern omega spectrometer. Nuclear Physics B-Proceedings Supplements*, **32** (1993):260.

[23] Spieler, H. *Semiconductor detector systems*, volume 12. Oxford university press (2005).

[24] Mikulec, B., Campbell, M. et al. *X-ray imaging using single photon processing with semiconductor pixel detectors. Nucl. Instrum. Methods Phys. Res., A*, **511** (2003), 1:282.

[25] Diemoz, P., Endrizzi, M. et al. *X-ray phase-contrast imaging with nanoradian angular resolution. Physical review letters*, **110** (2013), 13:138105.

[26] Walsh, M., Opie, A. et al. *First CT using Medipix3 and the MARS-CT-3 spectral scanner. JINST*, **6** (2011), 01:C01095.

[27] Hynds, D., LHCb Collaboration et al. *The Timepix telescope for charged particle tracking. Nucl. Instrum. Methods Phys. Res., A*, **A730** (2013):50.

[28] Pinsky, L., Stoffle, N. et al. *Application of the Medipix2 technology to space radiation dosimetry and hadron therapy beam monitoring. Nucl. Instrum. Methods Phys. Res., A*, **628** (2011):226.

[29] Caresana, M., Garlati, L. et al. *Real-time measurements of radon activity with the Timepix-based RADONLITE and RADONPIX detectors. JINST*, **9** (2014), 11:P11023.

[30] Petasecca, M., Loo, K. et al. *BrachyView: Proof-of-principle of a novel in-body gamma camera for low dose-rate prostate brachytherapy. Medical physics*, **40** (2013), 4:041709.

[31] Heijne, E. H., Sune, R. B. et al. *Measuring radiation environment in LHC or anywhere else, on your computer screen with Medipix. Nucl. Instrum. Methods Phys. Res., A*, **699** (2013):198.

[32] Whyntie, T., Bithray, H. et al. *CERN@school: demonstrating physics with the Timepix detector. Contemporary Physics*, **1** (2015):1.

[33] Jungmann, J. H., MacAleese, L. et al. *Fast, high resolution mass spectrometry imaging using a medipix pixelated detector. Journal of the American Society for Mass Spectrometry*, **21** (2010), 12:2023.

[34] Lau, J. H. *Flip chip technologies.* McGraw-Hill Professional (1996).

[35] Kraus, V., Holik, M. et al. *FITPix: Fast interface for Timepix pixel detectors. JINST*, **6** (2011):C01079.

[36] Turecek, D., Holy, T. et al. *Pixelman: a multi-platform data acquisition and processing software package for Medipix2, Timepix and Medipix3 detectors. JINST*, **6** (2011), 01:C01079.

[37] Jakubek, J., Cejnarova, A. et al. *Pixel detectors for imaging with heavy charged particles. Nucl. Instrum. Methods Phys. Res., A*, **591** (2008), 1:155 . Proceedings of the 9th International Workshop on Radiation Imaging Detectors.

[38] Jakubek, J. *Precise energy calibration of pixel detector working in time-over-threshold mode. Nucl. Instrum. Methods Phys. Res., A*, **633** (2011):S262.

[39] Kroupa, M., Hoang, S. et al. *Energy resolution and power consumption of Timepix detector for different detector settings and saturation of front-end electronics. JINST*, **9** (2014), 05:C05008.

[40] Hoang, S., Vilalta, R. et al. *Data Analysis of Tracks of Heavy Ion Particles in Timepix Detector.* In *Journal of Physics: Conference Series*, volume 523. IOP Publishing (2014) pages 012–026.

[41] Llopart, X., Campbell, M. et al. *Medipix2: a 64-k pixel readout chip with 55-μm square elements working in single photon counting mode. Nuclear Science, IEEE Transactions on*, **49** (2002), 5:2279.

[42] Ballabriga, R., Alozy, J. et al. *The Medipix3RX: a high resolution, zero dead-time pixel detector readout chip allowing spectroscopic imaging. JINST*, **8** (2013), 02:C02016.

[43] Poikela, T., Plosila, J. et al. *Timepix3: a 65K channel hybrid pixel readout chip with simultaneous ToA/ToT and sparse readout. Journal of instrumentation*, **9** (2014), 05:C05013.

[44] Visser, J., van Beuzekom, M. et al. *SPIDR: a read-out system for Medipix3 & Timepix3. Journal of Instrumentation*, **10** (2015), 12:C12028.

[45] Zang, A., Anton, G. et al. *The Dosepix detector - an energy - resolving photon - counting pixel detector for spectrometric measurements. JINST*, **10** (2015), 04:C04015.

[46] Olive, K. et al. *Review of Particle Physics. Chin.Phys.*, **C38** (2014):090001.

[47] Berger, M. J., Coursey, J. S. et al. *Stopping-power and range tables for electrons, protons, and helium ions.* (1998).

[48] Alberts, B., Johnson, A. et al. *Molecular Biology of the Cell.* Molecular Biology of the Cell. Taylor & Francis (2014).

[49] Bouchami, J., Gutierrez, A. et al. *Study of the charge sharing in silicon pixel detector with heavy ionizing particles interacting with a Medipix2 and a Timepix devices.* In *2008 IEEE Nuclear Science Symposium Conference Record* (2008) .

[50] Norlin, B., Reza, S. et al. *Readout cross-talk for alpha-particle measurements in a pixelated sensor system. JINST*, **10** (2015), 05:C05025.

[51] Antcheva, I., Ballintijn, M. et al. *ROOT: A C++ framework for petabyte data storage, statistical analysis and visualization. Comput.Phys.Commun.*, **182** (2011):1384.

[52] Idarraga, J. *MAfalda, An Analysis Framework for Pixel Detectors.* `https://twiki.cern.ch/twiki/bin/view/Main/MAFalda`.

[53] ATLAS Collaboration. *The ATHENA Analysis Framework.* `https://twiki.cern.ch/twiki/bin/viewauth/Atlas/AthenaFramework`.

[54] Toussaint, G. *A simple linear algorithm for intersecting convex polygons. The Visual Computer*, **1** (1985):118–123.

[55] Holy, T., Heijne, E. et al. *Pattern recognition of tracks induced by individual quanta of ionizing radiation in Medipix2 silicon detector. Nucl. Instrum. Methods Phys. Res., A*, **591** (2008):287.

[56] Bouchami, J., Gutierrez, A. et al. *Measurement of pattern recognition efficiency of tracks generated by ionizing radiation in a Medipix2 device. Nucl. Instrum. Methods Phys. Res., A*, **633** (2011):S187.

[57] Bergmann, B., Nelson, R. et al. *Time-of-flight measurement of fast neutrons with Timepix detectors. JINST*, **9** (2014), 05:C05048.

[58] Attix, F. H. *Introduction to radiological physics and radiation dosimetry.* John Wiley & Sons (2008).

[59] Rossi, H. H. and Zaider, M. *Microdosimetry and Its Applications.* Springer Science & Business Media (2012).

[60] George, S. P., Severino, C. T. et al. *Measurement of an accelerator based mixed field with a Timepix detector. JINST*, **10** (2015), 03:P03005.

[61] Hoang, S., Pinsky, L. et al. *LET estimation of heavy ion particles based on a timepix-based Si detector. J.Phys.Conf.Ser.*, **396** (2012):022023.

[62] Mitaroff, A. and Silari, M. *The CERN-EU high-energy reference field (CERF) facility for dosimetry at commercial flight altitudes and in space. Radiation Protection Dosimetry*, **102** (2002), 1:7.

[63] Ferrari, A., La Torre, F. et al. *Monitoring reactions for the calibration of relativistic hadron beams. Nucl. Instrum. Methods Phys. Res., A*, **763** (2014):177.

[64] Dietze, G., Bartlett, D. et al. *ICRP Publication 123: Assessment of Radiation Exposure of Astronauts in Space. Annals of the ICRP*, **42** (2013), 4.

[65] Douple, E. B., Mabuchi, K. et al. *Long-term Radiation-Related Health Effects in a Unique Human Population: Lessons Learned from the Atomic Bomb Survivors of Hiroshima and Nagasaki. Disaster Med Public Health Prep.*, **5** (2011):S122.

[66] Durante, M. and Cucinotta, F. A. *Heavy ion carcinogenesis and human space exploration. Nature Reviews Cancer*, **8** (2008), 6:465.

[67] Townsend, W. L. *Implications of the space radiation environment for human exploration in deep space. Radiation Protection Dosimetry*, **115** (2005):44.

[68] Blakely, E. A. and Chang, P. Y. *A review of ground-based heavy-ion radiobiology relevant to space radiation risk assessment. Part II: Cardiovascular and immunological effects. Advances in Space Research*, **40** (2007), 4:461.

[69] Baker, J. E., Moulder, J. E. et al. *Radiation as a risk factor for cardiovascular disease. Antioxidants & redox signaling*, **15** (2011), 7:1945.

[70] Curtis, S., Vazquez, M. et al. *Cosmic ray hit frequencies in critical sites in the central nervous system. Advances in Space Research*, **22** (1998), 2:197 . Life Sciences: Space Flight and the Central Nervous System: The Potential Independent and Synergistic Effects of Microgravity and Radiation.

[71] Cucinotta, F., Manuel, F. et al. *Space radiation and cataracts in astronauts. Radiation research*, **156** (2001), 5:460.

[72] Guo, J., Zeitlin, C. et al. *Variations of dose rate observed by MSL/RAD in transit to Mars. Astronomy & Astrophysics*, **577** (2015):A58.

[73] Wilson, J. W., Cucinotta, F. et al. *Shielding from solar particle event exposures in deep space. Radiation measurements*, **30** (1999), 3:361.

[74] Hu, S., Kim, M.-H. Y. et al. *Modeling the acute health effects of astronauts from exposure to large solar particle events. Health Physics*, **96** (2009), 4:465.

[75] Stoffle, N., Pinsky, L. et al. *Timepix-based radiation environment monitor measurements aboard the International Space Station. Nucl. Instrum. Methods Phys. Res., A*, **782** (2015):143.

[76] George, J. S., Lave, K. A. et al. *Elemental Composition and Energy Spectra of Galactic Cosmic Rays During Solar Cycle 23. The Astrophysical Journal*, **698** (2009), 2:1666.

[77] Heirtzler, J. R. *The future of the South Atlantic anomaly and implications for radiation damage in space. Journal of Atmospheric and Solar-Terrestrial Physics*, **64** (2002), 16:1701.

[78] Dachev, T., Atwell, W. et al. *Observations of the SAA radiation distribution by Liulin-E094 instrument on ISS. Advances in Space Research*, **37** (2006), 9:1672.

[79] International Commission on Radiological Protection. *ICRP Publication 60: 1990 Recommendations of the International Commission on Radiological Protection. Annals of the ICRP*, **21** (1991), 1-3.

[80] Guatelli, S., Reinhard, M. et al. *Tissue Equivalence Correction in Silicon Microdosimetry for Protons Characteristic of the LEO Space Environment. Nuclear Science, IEEE Transactions on*, **55** (2008), 6:3407.

[81] Badhwar, G. D. *Shuttle Radiation Dose Measurements in the International Space Station Orbits 1. Radiation research*, **157** (2002), 1:69.

[82] Kroupa, M., Bahadori, A. et al. *A semiconductor radiation imaging pixel detector for space radiation dosimetry. Life Sciences in Space Research*, (2015).

[83] Benton, E. R. and Benton, E. *Space radiation dosimetry in low-Earth orbit and beyond. Nucl. Instrum. Methods Phys. Res., B*, **184** (2001), 1-2:255.

[84] Cleveland, W. S. *LOWESS: A program for smoothing scatterplots by robust locally weighted regression. American Statistician*, (1981):54.

[85] Rossi, H. H. and Rosenzweig, W. *A Device for the Measurement of Dose as a Function of Specific Ionization 1. Radiology*, (1955).

[86] Hassler, D. M., Zeitlin, C. et al. *Mars' Surface Radiation Environment Measured with the Mars Science Laboratory's Curiosity Rover. Science*, **343** (2014), 6169:1244797.

[87] Cucinotta, F. A., Kim, M. et al. *Space radiation cancer risk projections and uncertainties. NASA Technical Report*, **217375** (2013):2013.

[88] Podgorsak, E. B. *Radiation physics for medical physicists.* Springer Science & Business Media (2010).

[89] Thomas, D. and Alevra, A. *Bonner sphere spectrometers - a critical review. Nucl. Instrum. Methods Phys. Res., A*, **476** (2002), 1:12.

[90] Menzel, H.-G. and Harrison, J. *Dosimetric quantities in radiological protection and risk assessment. Journal of Radiological Protection*, **32** (2012), 1:N41.

[91] Othman, M. A., Petasecca, M. et al. *Neutron dosimeter development based on Medipix2. Nuclear Science, IEEE Transactions on*, **57** (2010), 6:3456.

[92] Agostinelli, S., Allison, J. et al. *GEANT4: A Simulation toolkit. Nucl. Instrum. Methods Phys. Res., A*, **506** (2002):250.

[93] Ribon, A., Apostolakis, J. et al. *Status of geant4 hadronic physics for the simulation of lhc experiments at the start of lhc physics program. CERN-LCGAPP*, **2** (2010):2010.

[94] Hammersley, J. *Monte Carlo Methods.* Springer Science & Business Media (2013).

[95] Othman, A. *Optimising the packaging of semiconductor detectors to improve their energy response to gamma and neutron radiation for radiation protection: A Geant4 Monte Carlo study.* Ph.D. thesis, University of Wollongong, Wollongong, Australia (2012).

[96] Kirkpatrick, S., Gelatt, C. D. et al. *Optimization by Simulated Annealing. Science*, **220** (1983):671.

[97] Metropolis, N., Rosenbluth, A. W. et al. *Equation of state calculations by fast computing machines. J.Chem.Phys.*, **21** (1953):1087.

[98] *Material Safety Data Sheet : VisiJet Crystal, EX 200 Plastic Material.* `http://www.3dsystems.com/products/datafiles/visijet/msds/visijet-crystal/24184-S02-00-B-MSDS-US-English-EX-200-Crystal.pdf` (2012). Accessed : 30/09/2015.

[99] Lipson, H. and Kurman, M. *Fabricated: The new world of 3D printing.* John Wiley & Sons (2013).

[100] Borcea, C., Buono, S. et al. *First results from the neutron facility (ntof) at cern. Applied Physics A*, **74** (2002), 1:s55.

[101] Llopart, X., Ballabriga, R. et al. *Timepix, a 65k programmable pixel readout chip for arrival time, energy and/or photon counting measurements. Nucl. Instrum. Methods Phys. Res., A*, **581** (2007), 1-2:485.

[102] Costa, E., Soffitta, P. et al. *An efficient photoelectric X-ray polarimeter for the study of black holes and neutron stars. Nature*, **411** (2001), 6838:662.

[103] Bellazzini, R., Angelini, F. et al. *Reading a GEM with a VLSI pixel ASIC used as a direct charge collecting anode. Nucl. Instrum. Methods Phys. Res., A*, **535** (2004), 1:477.

[104] Bellazzini, R., Spandre, G. et al. *Direct reading of charge multipliers with a self-triggering CMOS analog chip with 105k pixels at 50μm pitch. Nucl. Instrum. Methods Phys. Res., A*, **566** (2006), 2:552.

[105] Bellazzini, R., Spandre, G. et al. *A sealed Gas Pixel Detector for X-ray astronomy. Nucl. Instrum. Methods Phys. Res., A*, **579** (2007), 2:853.

[106] Fabiani, S., Costa, E. et al. *The imaging properties of the Gas Pixel Detector as a focal plane polarimeter. The Astrophysical Journal Supplement Series*, **212** (2014), 2:25.

[107] Van der Graaf, H., Aarnink, T. et al. *The GRIDPIX Detector, History and Perspective. Modern Physics Letters A*, **28** (2013), 13:1340021.

[108] Corradi, G., Murtas, F. et al. *A novel High Voltage System for a triple GEM detector. Nucl. Instrum. Methods Phys. Res., A*, **571** (2007):96.

[109] Sauli, F. *GEM: A new concept for electron amplification in gas detectors. Nucl. Instrum. Methods Phys. Res., A*, **386** (1997), 2-3:531.

[110] Alfonsi, M., Bencivenni, G. et al. *High-rate particle triggering with triple-GEM detector. Nucl. Instrum. Methods Phys. Res., A*, **518** (2004):106.

[111] Biagi, S. F. *Monte Carlo simulation of electron drift and diffusion in counting gases under the influence of electric and magnetic fields. Nucl. Instrum. Methods Phys. Res., A*, **421** (1999).

[112] Blum, W., Reigler, W. et al. *Particle Detection with Drift Chambers*. Springer - Verlag, Berlin, Heidelberg, Germany (2008).

[113] Ziegler, M. and Straumann, U. *Development of a triple GEM detector for particle tracking*. In *Nuclear Science Symposium Conference Record, 2005 IEEE*, volume 2. IEEE (2005) pages 935–939.

[114] Nygren, D. *The time-projection chamber: A new 4. pi. detector for charged particles*. Technical report, Stanford Linear Accelerator Center, Menlo Park, CA (USA); Lawrence Berkeley Lab., CA (USA) (1974).

[115] Hough, P. a. *Machine Analysis Of Bubble Chamber Pictures. Conf.Proc.*, **C590914** (1959):554.

[116] Sauli, F. *Recent developments and applications of fast position-sensitive gas detectors. Nucl. Instrum. Methods Phys. Res., A*, **422** (1999):257.

[117] Ziegler, J. F., Ziegler, M. D. et al. *SRIM - The stopping and range of ions in matter (2010). Nuclear Instruments and Methods in Physics Research B*, **268** (2010):1818.

[118] Toussaint, G. T. *A Simple Linear Algorithm for Intersecting Convex Polygons. The Visual Computer*, **1** (1985):118.

[119] Apostolakis, J., Giani, S. et al. *An implementation of ionisation energy loss in very thin absorbers for the GEANT4 simulation package. Nucl. Instrum. Methods Phys. Res., A*, **453** (2000).

[120] Garty, G., Breskin, A. et al. *Single photoelectron detection with a low-pressure gas electron multiplier coupled to a CsI photocathode. Nucl. Instrum. Methods Phys. Res., A*, **433** (1999).

[121] Poikela, T., Plosilab, J. et al. *Timepix3: a 65K channel hybrid pixel readout chip with simultaneous ToA/ToT and sparse readout. JINST*, **9** (2014), 05:C05013.

[122] Gaza, R. *SRAG Measurements Performed During the Orion EFT-1 Mission*. In *Workshop on Radiation Monitoring for the International Space Station* (2015) .

[123] Granja, C., Polansky, S. et al. *Characterization and Directional Visualization of Space Radiation Quanta in Low Earth Orbit with the compact Spacecraft Payload SATRAM*. In *The 23rd International Workshop on Vertex Detectors* (2014) .

[124] Whyntie, T. and Harrison, M. *Full simulation of the LUCID experiment in the Low Earth Orbit radiation environment. JINST*, **10** (2015), 03:C03043.

[125] Grosswendt, B. *Nanodosimetry, from radiation physics to radiation biology. Radiation protection dosimetry*, **115** (2005), 1-4:1.

[126] Bergmann, B. *ARDENT ESR9 Logbook (Experiments at JINR).* `https://ardent.web.cern.ch/ardent/ardent.php?link=esr09-logbook` (2015). Accessed : 25/09/2015.

[127] Dalla Betta, G.-F., Da Via, C. et al. *Recent developments and future perspectives in 3D silicon radiation sensors. Journal of Instrumentation*, **7** (2012), 10:C10006.

[128] Lange, J., Cavallaro, E. et al. *3D silicon pixel detectors for the ATLAS Forward Physics experiment. Journal of Instrumentation*, **10** (2015), 03:C03031.

[129] Da Via, C. *Silicon sensors go 3D. CERN Courier*, (2012).

[130] Rosenfeld, A. *Novel detectors for silicon based microdosimetry, their concepts and applications. Nucl. Instrum. Methods Phys. Res., A*, (2015).